

University of Nebraska - Lincoln

DigitalCommons@University of Nebraska - Lincoln

Mechanical (and Materials) Engineering --
Dissertations, Theses, and Student Research

Mechanical & Materials Engineering,
Department of

3-2021

On Road Coordinates for Autonomous Vehicle Guidance

Ricardo Jacome

University of Nebraska-Lincoln, rjacome@huskers.unl.edu

Follow this and additional works at: <https://digitalcommons.unl.edu/mechengdiss>



Part of the [Materials Science and Engineering Commons](#), and the [Mechanical Engineering Commons](#)

Jacome, Ricardo, "On Road Coordinates for Autonomous Vehicle Guidance" (2021). *Mechanical (and Materials) Engineering -- Dissertations, Theses, and Student Research*. 169.
<https://digitalcommons.unl.edu/mechengdiss/169>

This Article is brought to you for free and open access by the Mechanical & Materials Engineering, Department of at DigitalCommons@University of Nebraska - Lincoln. It has been accepted for inclusion in Mechanical (and Materials) Engineering – Dissertations, Theses, and Student Research by an authorized administrator of DigitalCommons@University of Nebraska - Lincoln.

ON ROAD COORDINATES FOR AUTONOMOUS VEHICLE GUIDANCE

by

Ricardo Osmar Jacome

A DISSERTATION

Presented to the Faculty of

The Graduate College at the University of Nebraska-Lincoln

In Partial Fulfillment of Requirements

For the Degree of Doctor of Philosophy

Major: Mechanical Engineering and Applied Mechanics

Under the Supervision of Professor Cody S. Stolle

Lincoln, Nebraska

March, 2021

ON-ROAD COORDINATES FOR AUTONOMOUS VEHICLE GUIDANCE

Ricardo Osmar Jacome, Ph. D.

University of Nebraska, 2021

Advisor: Cody S. Stolle

Abstract. A new roadmap framework is proposed to improve the guidance and trajectory prediction capabilities of connected and automated vehicles (CAVs). Independent of road shape determination through external sensors, the system serves as a backup for challenging conditions, such as low sensor visibility and adverse environmental effects (e.g., rain, fog, snow). Based on the fusion of vehicle dynamics principles, differential geometry, and road design standards, the roadmap framework provides a consolidated collection of critical reference points of roadway centerlines and information about the shape of the roadway in the vicinity of a vehicle, including curvature, optimal travel velocity, and road alignment angle. Finally, the proposed roadmap for CAV reference offers versatility as additional data can be appended to the map, including elevation and roadside slope data, variable speed limits, and lane controls.

ACKNOWLEDGEMENTS

This has been a long journey, and I would not have made it without all the people who supported me during these years. I would like to thank my advisor Dr. Stolle for his guidance, support, and encouragement during my time at UNL. My committee members Dr. Faller, Dr. Reid, and Dr. Bobaru for their help and being my mentors, and the entire faculty at MwRSF for receiving me as part of an incredible team.

I would like to thank all of my coworkers/classmates for sharing part of their lives with me. Whether it was sharing a meal, a class, or a project, all of you have made this journey better. Michael Sweigard being the one I spent the most time with during work, his conversations were always fascinating, and our work progressed together.

Me gustaría agradecer y dedicarles todo mi esfuerzo a mis padres Ricardo y Maricela por haberme dado la oportunidad de vivir y por todo el esfuerzo que dedicaron para que yo pudiera salir adelante. Jamás habría podido salir adelante sin el apoyo de mi amada novia Elisa Vásquez, quien siempre me apoya con una sonrisa sin importar lo que ocurra. Agradezco la amistad y compañía de mis amigos Miguel y Luis que siempre han sido como una familia para mí. Mi hermano Uriel que siempre he querido ser un ejemplo a seguir para él. Y finalmente le dedico este trabajo a mi amiga Italia López por siempre ser un ejemplo a seguir para salir en cuanto explorar y arriesgarse se trata. Que este documento sea el principio de mucho más por venir. Gracias a todos por ser parte de la persona que soy hoy en día.

TABLE OF CONTENTS

CHAPTER 1. INTRODUCTION	1
1.1 Problem Statement	1
1.2 Review of Current State-of-the-Art Solutions	1
1.3 Proposed Solution	5
1.4 Potential Benefits	6
CHAPTER 2. CURRENT ROAD DESIGN PRACTICES	8
2.1 Alignment.....	8
2.2 Superelevation/Friction	12
2.3 Vehicle Dynamics Considerations	15
CHAPTER 3. DIFFERENTIAL GEOMETRY OVERVIEW	17
3.1 Clothoids	18
3.2 Serret-Frenet Coordinates	23
3.3 Acceleration in Serret-Frenet Coordinates.....	26
3.4 Bertrand (Parallel) Curves.....	29
3.5 References	31
CHAPTER 4. ROAD CURVATURE DECOMPOSITION FOR AUTONOMOUS GUIDANCE 42	
4.1 Introduction	43
4.1.1 Motivation.....	43
4.1.2 Path Prediction in Autonomous Vehicles	44
4.2 Method Formulation.....	46
4.2.1 Vehicle Dynamics and Road Design	46
4.2.2 Spatial Curvature Formulation.....	49
4.2.3 Segment Length Estimation.....	54
4.2.4 Road Curvature Decomposition.....	55
4.3 Implementation.....	57
4.3.1 Roadway Decomposition: AASHTO Base Model	57
4.3.2 Roadway Decomposition: Google Earth Images	59
4.3.3 Roadway Decomposition: GPS Model	63
4.3.4 Smoothing Techniques.....	64
4.3.5 Discussion	66
4.4 Recommendations	67

4.5	Summary/Conclusions	69
4.6	References	69
CHAPTER 5.	A DYNAMICALLY-CONCISE ROADMAP FRAMEWORK FOR GUIDING CONNECTED AND AUTOMATED VEHICLES	74
5.1	Introduction	75
5.2	Review of Transportation Guidance Frameworks	77
5.2.1	Machine-Driven Guidance Systems	77
5.2.2	Attributes for an All-Purpose Navigation System	80
5.3	Introduction to the MVRC Map Framework.....	82
5.3.1	Relationship Between Road Design and Vehicle Dynamics	83
5.3.2	Construction of MVRC Map	89
5.3.3	Example Construction of MVRC Map	92
5.3.4	Augmented Road Data.....	97
5.4	Discussion and Implementation of Map Framework	99
5.5	Conclusions	100
5.6	References	101
CHAPTER 6.	OPTIMIZATION OF ROAD REFERENCE PROFILES FOR CONNECTED AND AUTOMATED VEHICLES	110
6.1	Introduction	111
6.2	Background	112
6.2.1	MVRC Overview	112
6.2.2	Road Design.....	113
6.2.3	Vehicle Dynamics.....	115
6.3	Proposed Optimized References	116
6.4	Mathematical Road Curvature Models	117
6.5	Road Guidance Optimization Problem Formulation.....	119
6.5.1	Least Squares Fitting.....	119
6.5.2	Regional Road Reference-Numerical Optimization Routine	120
6.6	Implementation of Optimization Routine in Different Datasets	121
6.6.1	Analysis for AASHTO Dataset.....	122
6.6.2	Analysis for Empirical Road Dataset.....	124
6.7	Discussion on Alternative Applications	127
6.8	Conclusions	131
6.9	References	132

CHAPTER 7. ROAD ELEVATION REFERENCE FOR CONNECTED AND AUTOMATED VEHICLES FROM SERRET-FRENET FRAMES	136
7.1 Introduction	137
7.2 Proposed Three-Dimensional Augmentation of MVRC.....	138
7.2.1 Empirical State Estimation Considerations	141
7.3 Experimental Setup	143
7.3.1 Test Setup and Equipment	143
7.4 Post-Processing Results and Analysis.....	145
7.5 Conclusions and Recommendations.....	150
7.6 References	150
CHAPTER 8. SUMMARY/CONCLUSIONS	155
8.1 Summary	155
8.2 Key Findings	155
8.3 Recommendations/Future Work	156
8.4 Conclusions	158
Appendix.....	159
A.1 Formulation Chapter 3: Acceleration in Canonical Form.....	159
A.2 Potential Energy Derivation with Respect to Serret-Frenet Triad	168
A.3 Source Code Chapter 4: MDC Geometric Formulation Implementation	172
A.4 Formulation Chapter 6: Geometric Trapezoid	176
A.5 Source Code Chapter 6: Optimization Implementation	181
A.6 Residual Plots for all Vehicle Trials for Chapter 7	191
A.7 Histograms for all Vehicle Trials for Chapter 7	193

LIST OF FIGURES

Figure 1.1. Example of two trajectories (paths in blue) based on waypoints obtained by sensor data [16]	3
Figure 1.2. Road centerlines through: clothoid (top-left) [16], Hermite polynomial (top-right) [18], Spline (bottom-left) [19] and 3rd order polynomials approximating clothoids (bottom-right) [17]	4
Figure 2.1 Radius of Curvature Example for Arbitrary Curve	8
Figure 2.2 Horizontal and Vertical Alignment for a Given Street.....	9
Figure 2.3 Example Horizontal Curves	10
Figure 2.4 Spiral Curve Section Layout [71]	11
Figure 2.5 Half-Spiral Curve with Design Parameters [72]	12
Figure 2.6 Vehicle FBD in Road with Superelevation	13
Figure 2.7 Side Friction against Speed [70]......	14
Figure 2.8 Bicycle Kinematic Model [73]	15
Figure 3.1 Radius of Curvature with respect to a Segment Section	18
Figure 3.2 Cosine Fresnel Integral.....	21
Figure 3.3 Sine Fresnel Integral	21
Figure 3.4 Clothoid Example	22
Figure 3.5 Clothoid Section (left) and Clothoid Curvature (right)	22
Figure 3.6 Labeled Serret-Frenet Triad	24
Figure 4.1 Different Trajectories in Path from Point A to Point B.....	45
Figure 4.2 Normal-Tangential Coordinates Example in Vehicle's Center of Mass.....	47
Figure 4.3 Circumscribed Circle in Scalene Triangle.....	49
Figure 4.4 First Unit Vector Direction on Triangle.....	50
Figure 4.5 First- and Second-Unit Vectors on Triangle.	51
Figure 4.6 Radius of Curvature obtained from Geometric Relationships.	51
Figure 4.7 Scalene Triangle in Small Arc-Segment.	53
Figure 4.8 Road with Discrete Curvature Sections.....	55
Figure 4.9 Road with Discrete Radius of Curvature Sections.	56
Figure 4.10 Road Curvature Decomposition Example.	56
Figure 4.11 Finely-Discretized AASHTO Base Model: Road with Velocity Vectors.	58
Figure 4.12 Finely-Discretized AASHTO Base Model: Road with Curvature Vectors... ..	58
Figure 4.13 Finely-Discretized AASHTO Base Model: Curvature κ vs. Cumulative Curve Length.	59
Figure 4.14 Finely-Discretized AASHTO Base Model: Orthogonal Phase Shift of	59
Figure 4.15 Google Earth: I-80 Road Example.	60
Figure 4.16 Google Earth Model: Road with Curvature Vectors.	61
Figure 4.17 Google Earth Model: Curvature κ vs. Cumulative Curve Length.	61
Figure 4.18 Google Earth Model: Orthogonal Phase Shift Approach.	62
Figure 4.19 Google Earth Model: Road with Tangent Vectors.	62
Figure 4.20 GPS Model: Road with Curvature Vectors.	63
Figure 4.21 GPS Data: Tangent Vector Evaluation using Orthogonal Phase Shift Approach.	64
Figure 4.22 GPS Model: Road Construction with Tangent Vectors.	64

Figure 4.23 GPS Data: Smoothed Tangent Vector Data	65
Figure 4.24 GPS Model: Original Data (Left) and Smoothed Data (Right).	66
Figure 4.25 Implementation Scheme for Road Curvature Decomposition.....	68
Figure 5.1 Sample of Current CAV Guidance Framework	78
Figure 5.2 Proposed MVRC Framework for CAV Guidance.....	83
Figure 5.3 Vehicle Dynamics on a Superelevated Curve	85
Figure 5.4 Example Horizontal Curves	86
Figure 5.5 Serret-Frenet Coordinate System Definition and Vehicle Alignment.....	87
Figure 5.6 Serret-Frenet Frame Imposed on SAE Orientation Convention.....	88
Figure 5.7 MVRC Reference Data on Static Sample Map	92
Figure 5.8 Road Highway from Satellite Images (top) and Road Profile with MDC Curvature Vectors (bottom)	93
Figure 5.9 Road Tangent Angle and Data Smoothing	94
Figure 5.10 High Discretization for Simple Curve with Heading Angle Reference.	94
Figure 5.11 Low Discretization Simple Curve with Heading Angle Reference.....	95
Figure 5.12 ArcGIS Road Data Example	99
Figure 6.1 Example Horizontal Curves.	114
Figure 6.2 Organizational Flowchart of Study	116
Figure 6.3 General Curvature M.1, with Design Values	119
Figure 6.4 Regional Road Reference Numerical Optimization Routine Pseudo Code ..	121
Figure 6.5 AASHTO Road (left) and Fitted Curvature Profile (right).	123
Figure 6.6 AASHTO Compliant Road (left) with Optimized Velocity Profile (right)...	124
Figure 6.7 Empirical Road (left) and Fitted Curvature Profile (right).....	125
Figure 6.8 Empirical Road (left image) with Optimized Velocity Profile (right image)	126
Figure 6.9 Vehicle-Specific Road Reference Numerical Optimization Routine Pseudo-Code	128
Figure 6.10 Vehicle-Specific Reference Velocity: AASHTO standards (top image) and Empirical (bottom image).	129
Figure 7.1 Variant Geometry Curved Road Example.....	139
Figure 7.2 Road for Grade Testing	143
Figure 7.3 Testing Vehicles: Nissan Sentra (left), Nissan Altima (middle), and Hyundai Elantra (right).....	144
Figure 7.4 Sensor Velcro Mounting on Vehicle	145
Figure 7.5 Sample Angular Rate Readings for Nissan Sentra Trial 1	145
Figure 7.6 Numerically Integrated Angular Rates for Sentra-1	146
Figure 7.7 Numerical Drift Subtraction for Pitch in Sentra-1	146
Figure 7.8 Sentra-1 Vehicle Pitch and Vertical Elevation Profile	147
Figure 7.9 Empirical Vehicle Data Results for Sentra-1	147
Figure 7.10 Estimated Road Grade from Geodetic Road Data Results	148
Figure 7.11 Vehicle Empirical Data and Extracted Geodetic Data for all Vehicle Trials	149

CHAPTER 1. INTRODUCTION

1.1 Problem Statement

Recently, autonomous vehicles have become one of the most developed research fields to address vehicle crashes attributed to human error. However, these systems tend to operate reliably only at ideal road conditions. This assumes no weather disruptions, no paint marking deterioration, or any condition where road infrastructure is altered from their original purpose (e.g., extra lane paintings). Ongoing research is attempting to identify reliable solutions for weather and visibility constraints, but optical solutions continue to be challenging to accommodate for all environmental conditions. Thus, the problem statement for this work, lies in how to operate an autonomous vehicle under non-ideal road conditions where sensor performance is low.

1.2 Review of Current State-of-the-Art Solutions

To reduce the frequency of crash events and overall user safety on the road, industry and academia have developed Advanced Driver-Assistance Systems (ADAS) to assist drivers in identifying road geometries while maintaining the vehicle on the road [1][2][3].

The use of ADAS technology has been augmented through wireless communications, which has led to different schemes such as Vehicle-to-Vehicle (V2V) and Vehicle-to-Infrastructure (V2I). Vehicles with wireless capacities are denoted as Connected and Autonomous Vehicles (CAVs). V2I communications provide CAVs with traffic flow data for given areas along with weather alerts. Currently, this technology is in development and being tested by Departments of Transportation (DOTs) and research agencies for full-scale implementation [4][5][6][7].

According to *SAE Recommended Practice J306 2018*, CAVs can be classified into levels of autonomy based on the amount of Dynamic Driving Tasks (DDTs) a vehicle can perform [8]. DDTs are classified into Longitudinal DDTs and Lateral DDTs:

- Longitudinal DDT: Controlling the brake/throttle to achieve the desired forward vehicle travel behavior.
- Lateral DDT: Maintaining a desired vehicle travel direction by modulating braking and steering, ranging from simple guidance to emergency maneuvering.

DDTs can be performed by either a human driver or a vehicle controller. Human drivers perform all DDTs on levels 0 through 2. Levels 3 and 4 provide some automation wherein a controller takes over certain DDTs subject to criteria (e.g., minimum speed, clear visibility). Finally, level 5 consists of a vehicle performing all DDTs. Currently, no level 5 autonomy vehicle exists on the current market [9].

In terms of programming, to perform autonomous navigation, the vehicle performs four main tasks called perception, estimation, planning, and control which will be discussed in detail in Chapter 5. Pendleton et al. provides a complete review of the perception, estimation, planning, and control in autonomous vehicle systems [10].

To enhance the driving capabilities of CAVs, most research and development opts for two options: increase reliability of sensors or increase data quantity/quality for wireless transmission. In the first case, research has focused most of the development in multiple sensor options including ultrasonic, radar, lidar, mono-camera, and thermal camera [11]. This solution has often encounter most of its challenges under adverse conditions for sensor performance, such as the case of rain, snow, or high-reflectivity objects. For example, Zang et al. and Mohammed et al. provide a comprehensive review of the impact that weather

conditions have on sensor performance while driving on highways and urban traffic [12][13]. In the case of academia/DOT efforts, most research focuses in improving wireless communications and enhancing the type/quality of data [7]. Both of the approaches converge on a single objective, which is to increase the quality of data for trajectory generation in vehicles.

Trajectory generation is defined as the geometric path satisfying dynamic constraints that a vehicle needs to follow using controllers. In general, trajectory generation is the output of all techniques involved in the *motion planning* field. Gonzalez et al. and Claussmann et al. provide extensive literature in the types and classes of motion planning techniques available [14][15]. Intrinsically, trajectory generation is formed based on road radius readings from vehicle sensors, in conjunction with high-definition (HD) maps provided by V2I or network communications. As an example, Figure 1.1 shows the trajectory of a vehicle based on radius readings denoted as waypoints, and generates a trajectory based on two methods (a) point-wise tracking and (b) curve fitting.

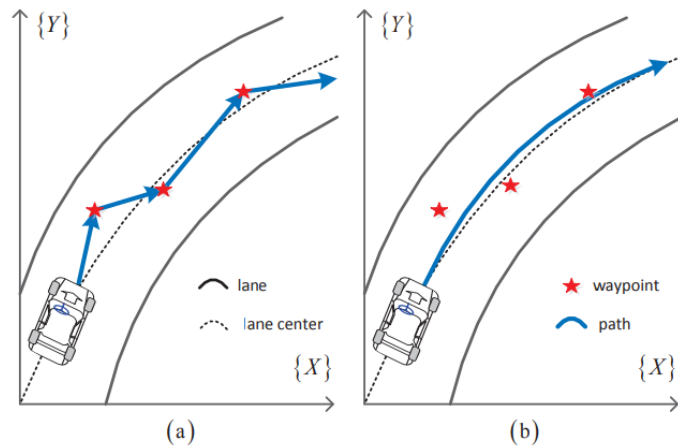


Figure 1.1. Example of two trajectories (paths in blue) based on waypoints obtained by sensor data [16]

Current HD map research focuses on the quality of road data, and different geometric techniques to model road centerlines properly. Betaille, et al. developed the concept of enhanced maps that provide high-accuracy with storage efficient mathematical clothoids [17]. Guo et al. used third-order polynomials on an approximated clothoid spline to represent lanes [18]. Chen et al. used cubic Hermite splines to for road centerlines [19]. Similarly, multiple spline-based options have been presented before to create geometric road representations [20][21][22][23]. Some examples of the described methods are shown in Figure 1.2. A summary table of the multiple research efforts along with their respective methodology for road centerlines is provided below.

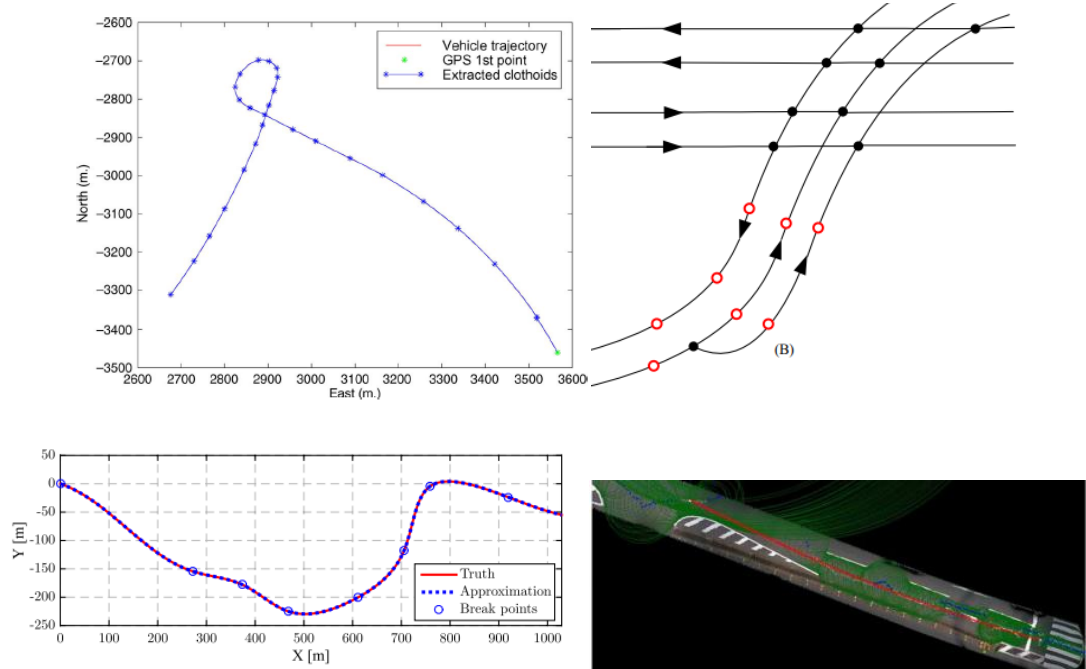


Figure 1.2. Road centerlines through: clothoid (top-left) [16], Hermite polynomial (top-right) [18], Spline (bottom-left) [19] and 3rd order polynomials approximating clothoids (bottom-right) [17]

Table 1.1. Summary of the state-of-the-art applications and methodologies for road centerlines in trajectory generation and digital maps.

Approach	Primary Advantages	Primary Disadvantages	Works Cited
Line and Circle	Low computational costs	Non-continuous paths, local-only	[24][25][26][27][28]
Clothoid	Transitions with linear curvature change	High computational costs, local-only	[17][29][30][31][32][33][34][35][36][37][38][39][40]
Polynomial	Low computational cost, continuous	High computational error as complexity increases, local-only	[18][41][42][43][44][45][46][47][48][49][50][51]
Spline	Low computational cost, continuous	Sacrifices optimality over continuity, local-only	[19][20][21][22][23][52][53][54][55][56][57]
Bezier	Low computational cost, continuous	Complexity increases with number of control points, local-only	[58][59][60][61][62][63][64][65][66][67]

Current enhanced maps share the characteristic of creating a road-centerline in Cartesian coordinates. These approaches are limited for trajectory generation usage because they ignore the dynamic constraints that a vehicle experiences while navigating a road. Furthermore, all the methods previously described rely on the assumption that the vehicle travels locally (i.e., two-dimensional). For CAV applications, when these centerlines are stored on a map it creates inconsistencies for large-scale implementation because of the three-dimensional characteristics of roads.

1.3 Proposed Solution

The present dissertation proposes the construction of a reference profile that is independent of Cartesian coordinates (e.g., not a road centerline representation). Instead, it uses dynamic road-attributes obtained from HD maps, which can be used for autonomous vehicle controller guidance. In other words a reference profile is developed, which the

vehicle references to navigate the road instead of attempting to identify simplified or detailed lane details during ad hoc guidance (e.g., provides appropriate speed level, steering capacity, acceleration limits). This information is then appended to the typical Cartesian coordinates that are used in conjunction with road centerline representation. Thus, constituting the dynamic attributes to navigate a given road centerline. Furthermore, it by only using dynamic attributes, the problem of locality previously shown in other methods is solved. To the extents of the author's knowledge, this approach has not been implemented in the past.

1.4 Potential Benefits

The benefits of a full-scale implementation of the proposed research is an overall reduction on vehicle run-off-road (ROR) crashes. According to the National Highway Traffic Safety Administration (NHTSA) *Fatal Accident Reporting System* (FARS) statistics [68] and the Insurance Institute for Highway Safety (IIHS) and Highway Loss Data Institute (HLDI) annual compilations [69], approximately 10,000 fatal ROR crashes occur each year involving roadside fixed objects.

Non-fatal ROR crashes are also concerning and economically devastating. Research conducted at the University of Nebraska-Lincoln identified approximately 440,000 crashes involving only roadside trees and utility poles in a five-year period spanning twelve geographically dissimilar states [70]. It was determined that the United States experiences an estimated \$13 to 17 billion in direct (emergency medical services, first responders, cleanup, infrastructure repairs) and indirect costs (traffic congestion, loss of workdays and taxable income, incapacitation, lawsuits) related only to non-fatal roadside tree and utility

pole crashes every year. Thus, there is potential savings and overall driver safety from the implementation of the aforementioned solution.

The construction of this dissertation will encompass the following. Chapters 2 and 3 will contain background for the understanding of current road design practices, and differential geometry. These might be omitted if desired. Chapters 4 through 7 are a collection of publications of the work in place for this dissertation. Chapter 4 is journal article published in the *Technical Publication Series for SAE* that details the geometric formulation and extraction of the curvature from multiple data sources. Chapter 5 is a conference proceedings journal accepted for publication in the *ITAVT conference for IFIP/IEEE* that outlines the system of having a roadmap communicating dynamic data, to serve as a reference to vehicles; elaborates on the benefits, and implementation of the system. Chapter 6 is a journal article submitted for publication in the *Transactions for Intelligent Transportation Systems in IEEE* that involves an augmentation of Chapter 5 by optimization routines for velocity references. Finally, Chapter 7 is a journal article submitted for publication that updates the system to provide three-dimensional data from empirical data. Finally, conclusions are given for the overall study.

CHAPTER 2. CURRENT ROAD DESIGN PRACTICES

To formulate a mathematical basis of a road reference module, a review and understanding of road design is first needed. This chapter explains the current methods for highway road design, and its limitations.

In the United States, the prevailing standards for road design come from The American Association of State Highway and Transportation Officials (AASHTO), referred as the Green Book. This book offers an extensive review of road design considerations that comply with vehicle dynamic behavior [71]. In this chapter, road designs will be considered in two main aspects: alignment and superelevation/friction.

2.1 Alignment

In road design, an alignment is defined by a series of points, lines and/or curves. These points are obtained from high accuracy GPS coordinates, each line and curve must connect exactly on a shared point or be coincident. When curves are formed, a radius of curvature is assigned to it. This is defined, as the radius of an imaginary (prescribed) circle that would fit per section of the road, as shown in Figure 2.1.

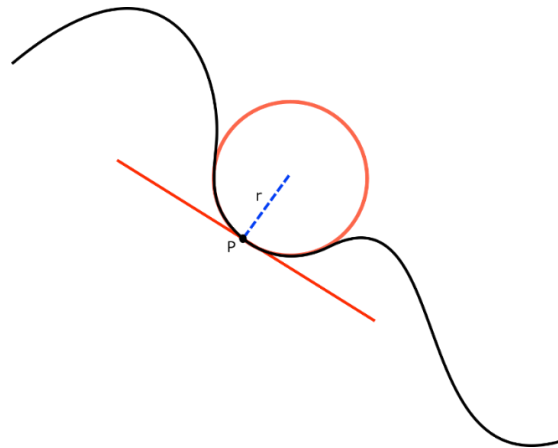


Figure 2.1 Radius of Curvature Example for Arbitrary Curve

Alignment is classified as either horizontal or vertical. Horizontal alignment refers to the lines or curves viewed from a 2-Dimensional top view of the Earth (obtained through satellite images, or ArcGIS). High accuracy GPS points are needed for horizontal alignment design; since, it defines the geometry of the road. Vertical alignment starts from looking at the horizontal alignment curves from a 2-Dimensional lateral view in which uphill or downhill considerations are added. An example of both is shown in Figure 2.2. Horizontal can be thought as the top view of a street and vertical as the lateral view of the same street.

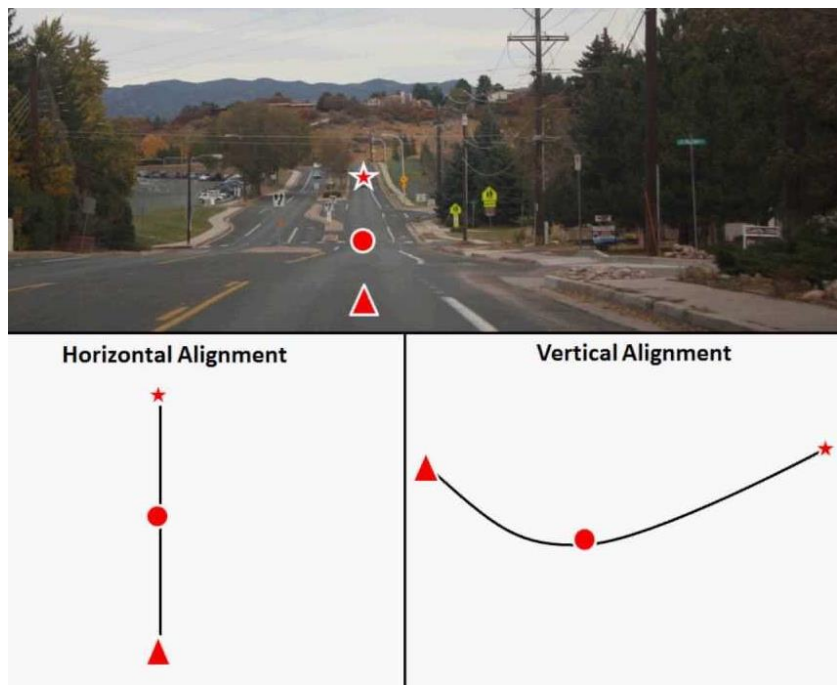


Figure 2.2 Horizontal and Vertical Alignment for a Given Street

Horizontal alignment affects the operational characteristics of roadways, such as vehicle operating speeds, sight distances, and highway capacity. Highway road design is influenced by many factors, including terrain, traffic volume, environmental factors, or right-of-way availability. Thus, road design engineers must design horizontal alignment

curves to provide a safe, functional roadway facility that provides adequate sight distances within economic constraints.

There exist multiple types of horizontal alignment designs, as shown in Figure 2.3 with their respective names. In general, most designs are made with simple or spiral curves. The radius of curvature plays a crucial role in horizontal alignment design; since, it is the primary source of transition for vehicles between curves.

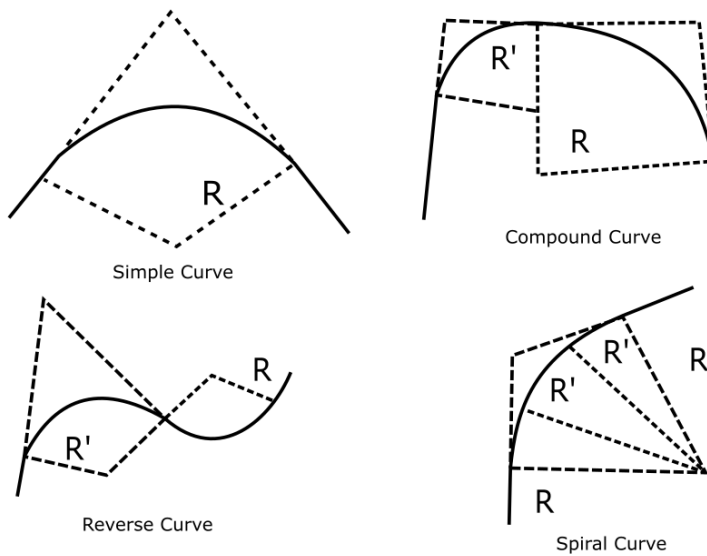


Figure 2.3 Example Horizontal Curves

The most general, and often most complicated, type of horizontal alignment is called a spiral curve. Spiral curves are made of five main components, known as initial tangent, spiral curve transition, circular curve, spiral curve transition, and final tangent. An example of a spiral curve is shown in Figure 2.4 below [72].

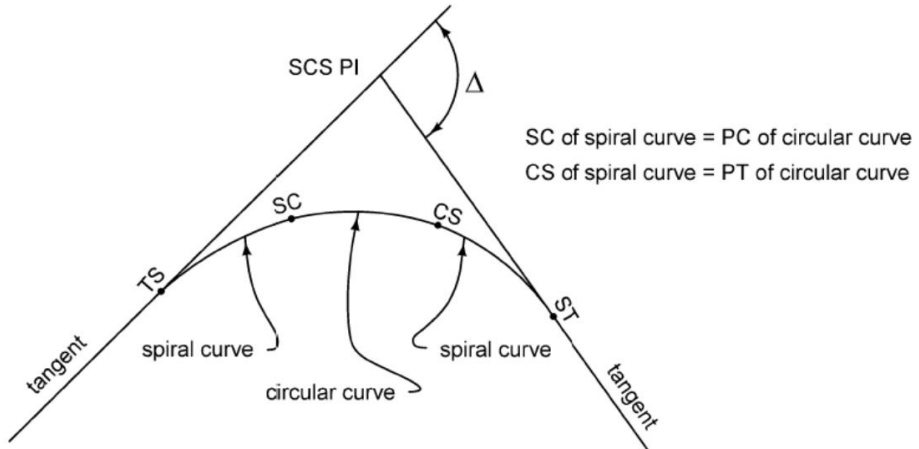


Figure 2.4 Spiral Curve Section Layout [72]

In road design, spiral curves are designed using formulas provided by AASHTO and DOTs to design discrete length segments and their attributes. A sample half-spiral curve is shown in Figure 2.5 [73]. Mathematically, the formulas provided are not an analytical representation of the curve, but independent formulas to estimate appropriate waypoints, coordinates, or segment lengths of the curve. These formulas are used because they work in conjunction with current software of road design, but they are not an appropriate reference for vehicles. The primary disadvantage of these formulas for V2I usage is to store all different road design formulas and have to look-up for the appropriate set as different streets are encountered. Analytical models of the road horizontal alignment need to be represented for creating an appropriate road reference for autonomous vehicles. These analytical models will be derived from differential geometry and will be discussed in detail in Chapter 3.

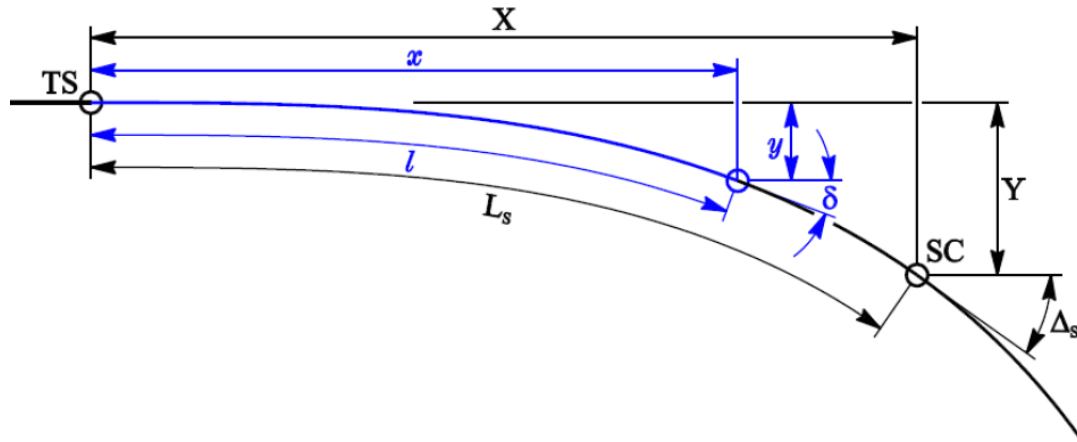


Figure 2.5 Half-Spiral Curve with Design Parameters [73]

2.2 Superelevation/Friction

When traveling on a horizontal curve, if the road is not a straight line, centrifugal forces act on vehicles trying to pull them outward. At low speeds or large radius curves, these effects are neglected. However, at high speeds or small radius curves, the effects of centrifugal forces increase. An excessive amount of these forces may cause lateral movement of the turning vehicle, thus causing dynamic instability where the vehicle may deviate from the road [74][75].

To prevent these instabilities, superelevation and road friction are used. Superelevation is the banking of the roadway, such that the outside edge of pavement is higher than the inside edge. This superelevation reduces the amount of centrifugal forces by creating a component to this force that is balanced with the vehicle's weight. The use of superelevation allows a vehicle to travel through a curve safely at a higher speed that would otherwise be impossible [71][74]. Side friction developed between the tires and the road surface also acts to counterbalance the outward pull on the vehicle. Side friction is reduced

when water, ice, or snow is present or when tires become excessively worn. When side friction is considerably low, driving should change accordingly to avoid instabilities.

Analysis on superelevation and side friction is performed by point particle dynamics as per the AASHTO Green Book [71]. The dynamics are formulated using Newton's Second Law of motion. A Free Body Diagram of the front vehicle is shown in

Figure 2.6.

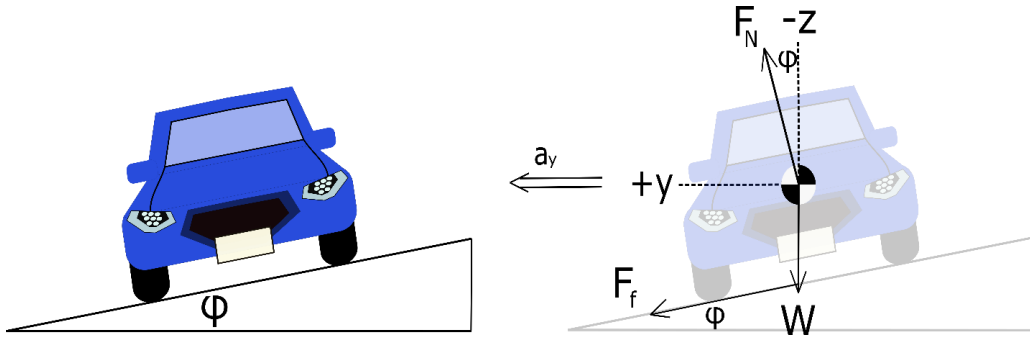


Figure 2.6 Vehicle FBD in Road with Superelevation

By performing a force analysis on the front and top view of a vehicle, the following formula is obtained [71]:

$$\frac{v^2}{g\rho} = \frac{\mu + 0.01e}{1 - 0.01\mu e} \quad (2.1)$$

v = Vehicle velocity (m/s)

e = Superelevation (as a percentage)

g = Gravitational acceleration (9.81 m/s^2)

μ = Coefficient of side road friction

ρ = Radius of curvature (m)

AASHTO provides graphs of different combinations for superelevation, friction, velocity, and radius of curvature, as shown in Figure 2.7. Similarly, the Green Book provides tabulations for interpolation of values as it is decided by the road design engineer. In road design, it is desired that roads contain a range of suitable parameters for a large classification of vehicles. This process consider that small car vehicles and trailers can maneuver and co-exist in the same road with similar driving parameters.

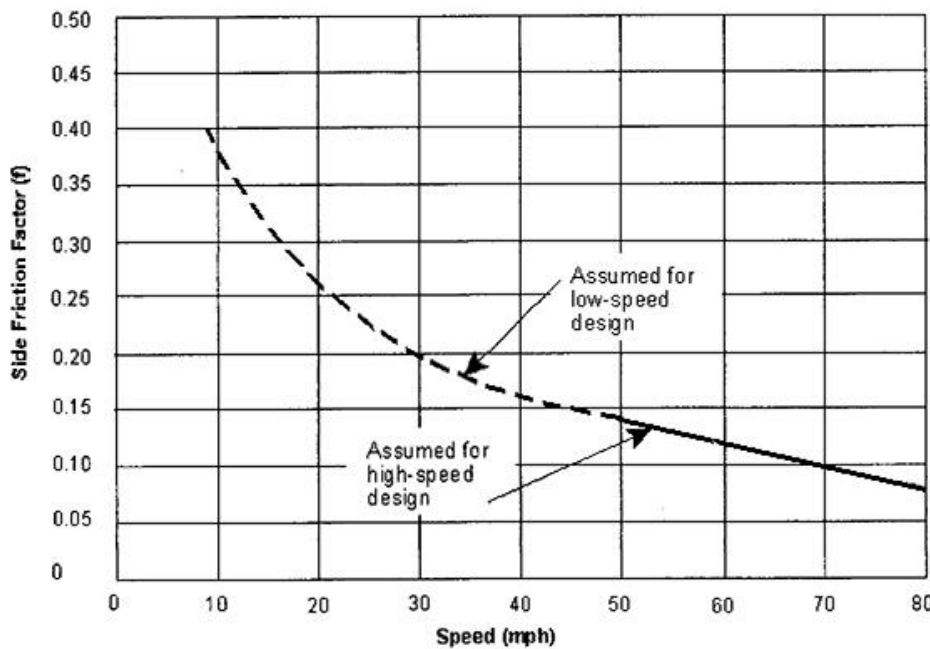


Figure 2.7 Side Friction against Speed [71]

Some limitations within the Green Book are that point particle dynamics does not take into consideration many dynamic factors that are dependent on vehicle characteristics, such as track width or length.

In practice, the data to create horizontal alignment curves is based on high accuracy GPS data, survey data, and a line creation tool. For this work, the road reference will be

based on a numerical and analytical representation. The analytical portion will be analyzed next based on the differential geometry study of space curves.

2.3 Vehicle Dynamics Considerations

The Green Book procedures are limited to primarily road parameters and point-particle dynamic analysis. During high-speed and low-speed cornering, a more thorough analysis of vehicle dynamics is necessary to develop a relationship between road data and vehicle data.

The model that will be assumed is the Bicycle Model as shown in Figure 2.8 [74]. This model assumes that the behavior of the right and left tires is symmetric across the Center-of-Gravity (CG) longitudinal axis. Note in Figure 2.8, subscript denotes either rear or front, and superscripts denote either longitudinal or transverse directions.

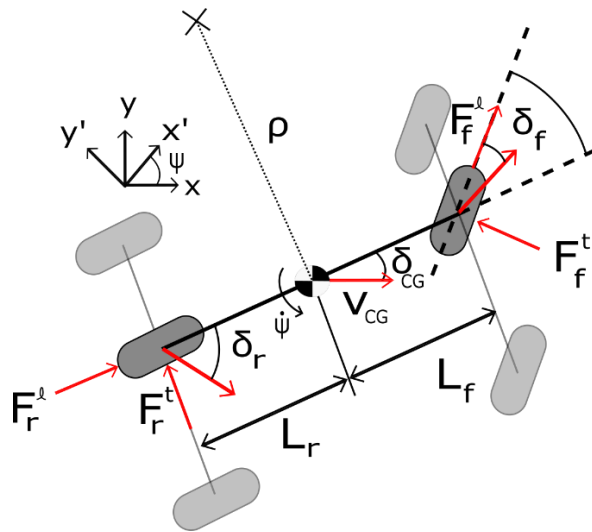


Figure 2.8 Bicycle Kinematic Model [74]

The Bicycle Model relates vehicle geometry and Newton's Second Law of motion through the famous Ackerman Steering formula [74][75]:

$$\delta_f = (57.3L + \eta v^2)\rho^{-1} \quad (2.2)$$

Where:

δ_f = Front wheel directional angle (deg)

ρ = Radius of curvature (m)

v_{CG} = CG Vehicle velocity (m/s)

L = Total sum of rear length L_r and front length L_f (m)

η = Understeer gradient (deg-s²/m)

Equation (2.2) relates the wheel steering angle (or Ackerman's angle) to the vehicle parameters and offers more information on vehicle behavior at curves. Ackerman's angle controls the change of the vehicle's heading angle. Thus, maintaining wheel steering angle at low values is crucial to prevent vehicle yaw instabilities (e.g., spin off road).

CHAPTER 3. DIFFERENTIAL GEOMETRY OVERVIEW

As described on Chapter 1, CAVs require a mathematical model to reference given a road section. However, the techniques for road designs, do not offer analytical models to represent the roads a vehicle can use.

The objective of the current chapter is to develop a mathematical foundation that will be used in later chapters to represent roads in an analytical form that vehicles can reference during autonomous navigation. Fundamental principles come from classical and differential geometry. A basic understanding of geometry is assumed, preliminary geometry formulae will be presented on this chapter and serve as an establishment of the notations used throughout this work.

On Chapter 2, radius of curvature was explained as a main characteristic that road designers use. However, for representation of analytical curves, the inverse function is used, such that curvature κ is presented as:

$$\kappa(s) = \frac{1}{\rho(s)} \quad (3.1)$$

The curvature is defined as the rate of change of the tangent of the arc length. Let ρ represent the radius of a perfect circle, ds being its differential arc length, and $d\theta$ being the angle between any axis (i.e., horizontal axis), and ρ . As it is shown in Figure 3.1, assuming small angles, the curvature of a curve can be denoted as:

$$\sin d\theta = \frac{ds}{\rho} \rightarrow d\theta = ds\kappa \rightarrow \kappa = \frac{d\theta}{ds}$$

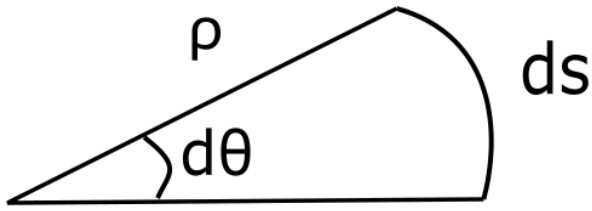


Figure 3.1 Radius of Curvature with respect to a Segment Section

3.1 Clothoids

Let a curve be represented by the form $x = x(s)$ where the arbitrary parameter s can represent arc length. By looking at the representation $x = x(s)$, there is a dependence on the choice of coordinate system in space. In this work, it is needed to represent a curve by invariant terms, such that it is independent of coordinate systems. Earliest investigations of the invariance of curve representation come from Kreyszig [76].

Invariance is defined as an intrinsic property that a curve has that is independent of the coordinate system chosen. In Euclidean 3D space, the distance represented with the norm of two points is the simplest invariant quantity that can be found, such that if $d = y - x$:

$$\|d\| = \sqrt{\sum_{i=1}^3 (y_i - x_i)^2} = \sqrt{\sum_{i=1}^3 (d_i)^2} = \sqrt{(d \cdot d)} \quad (3.2)$$

Where:

d = Euclidean distance

y_i = Vertical coordinate

x_i = Horizontal coordinate

Previous studies in the theory of curves have developed the existence and uniqueness of an invariant representation of curves [76][77]. The theory shows that arc length, curvature, and torsion are invariant functions that can describe any general curve. By making the arc length the independent variable of curvature and torsion, the following two equations are found:

$$\kappa = \kappa(s) \quad & \quad \tau = \tau(s) \quad (3.3)$$

These are called the *intrinsic* or *natural equations* of the curve, such that the natural equations represent an invariant form for any general curve. Curvature can be pictured as the amount of deviation of a curve from a straight line, and torsion as the deviation of a curve from being constrained to a plane. Thus, torsion will always be zero for two-dimensional space curves.

If $\theta(s)$ is the angle to the tangent vector $t(s)$ to the curve from a horizontal axis. Then, $t(s) = [\cos(\theta) \sin(\theta)]$. As it was previously determined, curvature can be expressed as:

$$\kappa = \frac{d\theta}{ds} \quad (3.4)$$

Considering the case of a 2D curve, a representation can be found such that the natural equations are:

$$\kappa = \frac{s}{c^2} \quad & \quad \tau = 0 \quad (3.5)$$

Where c represents an arbitrary constant. This set of natural equations are known as a Cornu Spiral [77][78]. Recalling equation (3.4) and $\theta(s)$, the angle can be found as follows:

$$\kappa = \frac{d\theta}{ds} \rightarrow d\theta = \kappa ds \rightarrow \theta = \int \kappa ds + \theta_0 \quad (3.6)$$

Assuming zero initial conditions, substituting the natural equations (3.5), and applying a change of variable:

$$\theta = \int_0^s \frac{1}{c^2} \sigma d\sigma \rightarrow \theta = \frac{s^2}{2c^2} \quad (3.7)$$

Where:

θ = Curve tangent angle

c = Arbitrary constant

s = Segment length

σ = Arbitrary constant

By recalling the tangent of a curve C , $dx = \cos(\theta(s))ds$ and $dy = \sin(\theta(s))ds$, and using equation (3.4), the following known as Cosine/Sine Fresnel Integrals are found [77]:

$$x = \int_0^s \cos(\theta(\sigma))d\sigma = \int_0^s \cos\left(\frac{\sigma^2}{2c^2}\right) d\sigma \quad (3.8)$$

$$y = \int_0^s \sin(\theta(\sigma))d\sigma = \int_0^s \sin\left(\frac{\sigma^2}{2c^2}\right) d\sigma \quad (3.9)$$

The integrals (3.8) and (3.9) are computationally expensive to evaluate as they cannot be evaluated in terms of elementary functions. Examples of the Fresnel Integrals is shown in Figure 3.2 and Figure 3.3.

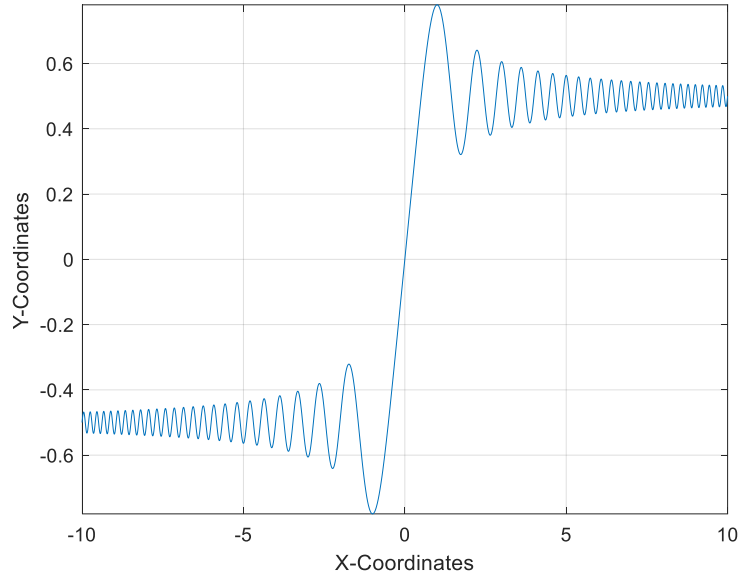


Figure 3.2 Cosine Fresnel Integral

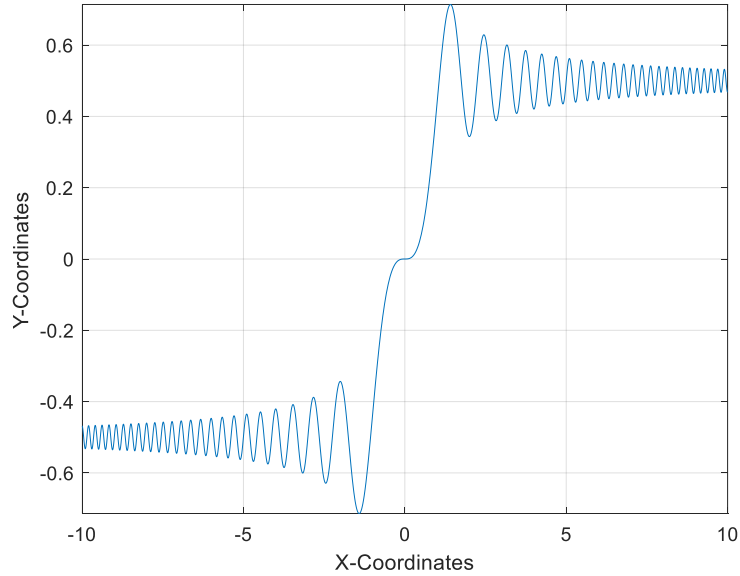


Figure 3.3 Sine Fresnel Integral

When these two functions are plotted together, a clothoid is formed. An example clothoid is shown in Figure 3.4. Clothoids are often used as the main resource on curve design, because clothoids have a linear curvature profile. So that, when travelled at a

constant speed, the curvature varies in proportion to time to provide a smooth ride. An example of the top section of the clothoid is shown along with its curvature profile on Figure 3.5, where the linear relationship is noticeable.

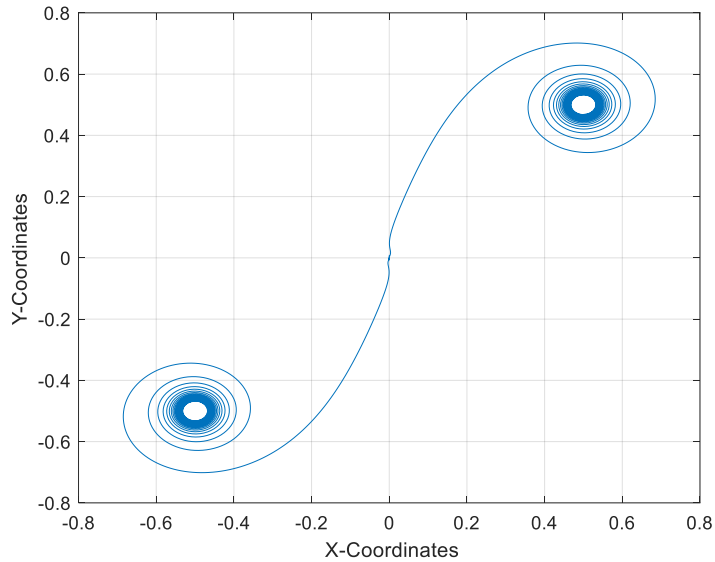


Figure 3.4 Clothoid Example

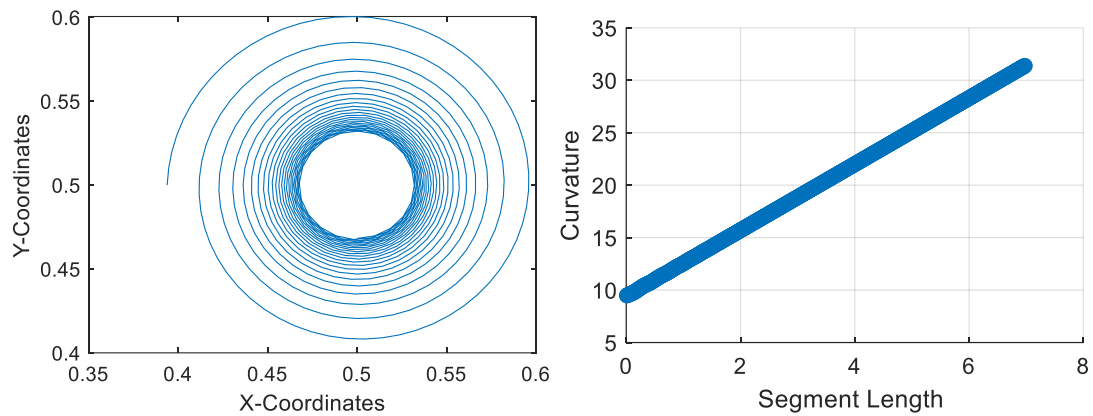


Figure 3.5 Clothoid Section (left) and Clothoid Curvature (right)

3.2 Serret-Frenet Coordinates

This subsection will elaborate on the formulation of the Serret-Frenet formulas and their canonical representations. At this point, it will be assumed that all vectors are functions of segment length s , unless otherwise stated. Considering a curve C be defined by a vector in three-dimensional space with $\mathbf{r} = [r_1, r_2, r_3]$. For C , the unit tangent vector \mathbf{T} can be defined as the unit vector of the derivatives of \mathbf{r} :

$$\mathbf{T} = \frac{\mathbf{r}'}{\|\mathbf{r}'\|} = \frac{d\mathbf{r}}{ds} \quad (3.10)$$

As it was defined previously, the curvature can be related for small angles through (3.4) to obtain:

$$\kappa = \left\| \frac{d\mathbf{T}}{ds} \right\| \quad (3.11)$$

The principal normal \mathbf{N} will be defined as

$$\mathbf{N} = \frac{\frac{d\mathbf{T}}{ds}}{\left\| \frac{d\mathbf{T}}{ds} \right\|} = \frac{1}{\kappa} \frac{d\mathbf{T}}{ds} \rightarrow \frac{d\mathbf{T}}{ds} = \kappa \mathbf{N} \quad (3.12)$$

Noting that $\|\mathbf{T}\| = \mathbf{T} \cdot \mathbf{T} = 1$, it follows that $\left(\frac{d\mathbf{T}}{ds} \mathbf{T} + \mathbf{T} \frac{d\mathbf{T}}{ds} \right) = 0$. This indicates that for the dot product of two unit tangent vectors to be zero, the principal normal has to be zero as well, proving that both unit tangent and principal normal are perpendicular [76].

Lastly, the binormal product is defined by the cross product of the unit tangent and principal normal:

$$\mathbf{B} = \mathbf{T} \times \mathbf{N} \quad (3.13)$$

The Serret-Frenet triad (**T**, **N**, **B**) can now be illustrated with their corresponding plane names in Figure 3.6. Where their respective plane names are T-N: Osculating Plane, N-B: Normal Plane, and B-T: Rectifying Plane [76][78].

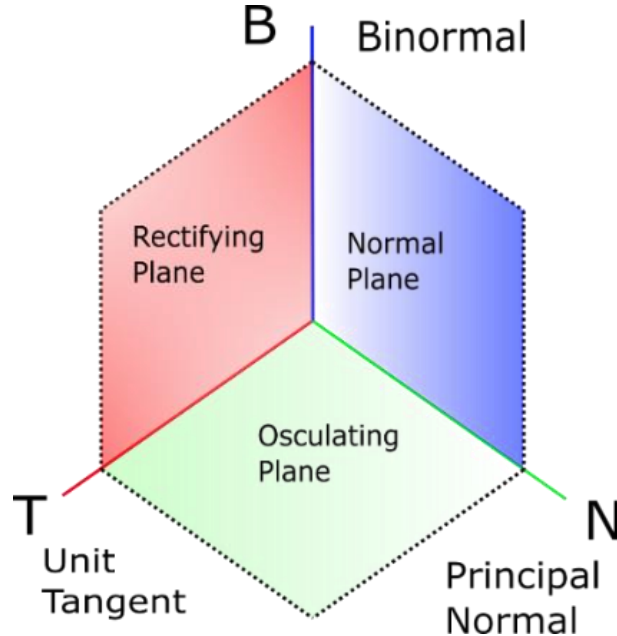


Figure 3.6 Labeled Serret-Frenet Triad

Similar to the unit tangent vector, the principal normal can be derived as follows:

$$\|N\| = N \cdot N = 1 \xrightarrow{\frac{d}{ds}} \left(\frac{dN}{ds} N + N \frac{dN}{ds} \right) = 0 \quad (3.14)$$

Equation (3.14) implies that the unit principal normal has to be perpendicular to its derivative with respect to s. To find this derivative, first assume that $\frac{dN}{ds}$ is a superposition of the three unit vectors (**T**, **N**, and **B**) with arbitrary constants such that:

$$\frac{dN}{ds} = \alpha T + \tau B + \gamma N \quad (3.15)$$

Noting that $\frac{dN}{ds} \perp N$, the vector $\frac{dN}{ds}$ is now constrained to the rectifying plane:

$$\frac{d\mathbf{N}}{ds} = \alpha\mathbf{T} + \tau\mathbf{B} \quad (3.16)$$

Where α and τ are arbitrary constants. Since the binormal vector is defined to be perpendicular to the osculating plane, the constant τ can be defined as a deviation from the osculating plane. This τ will be denoted as torsion. Deriving the cross product used earlier:

$$\begin{aligned} \frac{d\mathbf{B}}{ds} &= \frac{d(\mathbf{T} \times \mathbf{N})}{ds} = \frac{d\mathbf{T}}{ds} \times \mathbf{N} + \mathbf{T} \times \frac{d\mathbf{N}}{ds} \\ \frac{d\mathbf{B}}{ds} &= \kappa\mathbf{N} \times \mathbf{N} + \mathbf{T} \times (\alpha\mathbf{T} + \tau\mathbf{B}) = \mathbf{T} \times \tau\mathbf{B} = -\tau\mathbf{N} \end{aligned} \quad (3.17)$$

This approach can be repeated with the principal normal to find α :

$$\begin{aligned} \mathbf{N} &= \mathbf{B} \times \mathbf{T} \\ \frac{d\mathbf{N}}{ds} &= \frac{d(\mathbf{B} \times \mathbf{T})}{ds} = \frac{d\mathbf{B}}{ds} \times \mathbf{T} + \mathbf{B} \times \frac{d\mathbf{T}}{ds} \\ \frac{d\mathbf{N}}{ds} &= -\tau\mathbf{N} \times \mathbf{T} + \mathbf{B} \times \kappa\mathbf{N} = \tau\mathbf{B} - \kappa\mathbf{T} \end{aligned} \quad (3.18)$$

By comparison of (3.18) with (3.16), it is noticed that $\alpha = -\kappa$. Formulas (3.12), (3.17), and (3.18) together are called the Serret-Frenet Formulas [77][78][79]:

$$\frac{d\mathbf{T}}{ds} = \kappa\mathbf{N} \quad (3.19)$$

$$\frac{d\mathbf{N}}{ds} = -\kappa\mathbf{T} + \tau\mathbf{B} \quad (3.20)$$

$$\frac{d\mathbf{B}}{ds} = -\tau\mathbf{N} \quad (3.21)$$

3.3 Acceleration in Serret-Frenet Coordinates

Recall from the chain rule that the following is true when deriving with respect to segment length:

$$\frac{d}{ds} = \frac{dt}{ds} \frac{d}{dt} = \left(\frac{1}{\frac{ds}{dt}} \right) \frac{d}{dt} = \frac{1}{\dot{s}} \frac{d}{dt} \rightarrow \frac{d}{dt} = \dot{s} \frac{d}{ds} \quad (3.22)$$

This equation denotes that, for unity constant velocity, deriving with respect to time or segment length is the same. Equation (3.22) will be used throughout the following formulations rather consistently. Using a curve with the vector representation $\mathbf{r} = [r_1, r_2, r_3]$, the following time derivative can be found [78]:

$$\begin{aligned} \mathbf{v} &= \frac{d\mathbf{r}}{dt} = \dot{s} \frac{d\mathbf{r}}{ds} = \dot{s} \mathbf{T} \\ \frac{d^2\mathbf{r}}{dt^2} &= \frac{d}{dt}(\dot{s}\mathbf{T}) = \frac{d}{dt}(\dot{s})\mathbf{T} + \frac{d\mathbf{T}}{dt}\dot{s} = \ddot{s}\mathbf{T} + \dot{s}\left(\frac{d\mathbf{T}}{ds}\frac{ds}{dt}\right) = \ddot{s}\mathbf{T} + \dot{s}^2\left(\frac{d\mathbf{T}}{ds}\right) = \ddot{s}\mathbf{T} + \dot{s}^2(\kappa\mathbf{N}) \\ \mathbf{a} &= \frac{d^2\mathbf{r}}{dt^2} = \ddot{s}\mathbf{T} + \dot{s}^2\kappa\mathbf{N} \end{aligned} \quad (3.23)$$

This formula denotes the classical acceleration of a particle on an arbitrary curve in Serret-Frenet coordinates. By construction, the acceleration vector in Equation (3.23) will never contain a component in the binormal direction. This construction can only be valid for a planar curve assumption [76]. When considering three-dimensional or space curves, the assumption is no longer valid [79].

For most practical purposes, analysis of space curves simplifies the motion of particles to be plane. This is if a curve can be represented through a vector representation where $\mathbf{r} \neq \mathbf{r}(\kappa, \tau)$ and $\tau = 0$. This assumption becomes invalid when the desired trajectory is a space curve, such that the vector $\mathbf{r} = \mathbf{r}(\kappa, \tau)$.

To implement the general case of acceleration in a space curve, a canonical representation $\mathbf{r} = \mathbf{r}(\kappa, \tau)$ will be used. The primary advantage is that the resulting vector will be invariant under any coordinate transformation. Starting from Taylor's approximation [76]:

$$\mathbf{r}(s) = \mathbf{r}(0) + \sum_{n=1}^3 \frac{s^n}{n!} \left(\frac{d^n \mathbf{r}(0)}{ds^n} \right) + o(s^3) \quad (3.24)$$

For this work, applying Taylor's approximation up to a third term, we can approximate any curve in terms of its invariant forms with the following:

$$\mathbf{r}(s) = \mathbf{r}(0) + \frac{s^1}{1!} \left(\frac{d^1 \mathbf{r}(0)}{ds^1} \right) + \frac{s^2}{2!} \left(\frac{d^2 \mathbf{r}(0)}{ds^2} \right) + \frac{s^3}{3!} \left(\frac{d^3 \mathbf{r}(0)}{ds^3} \right) + o(s^3) \quad (3.25)$$

The terms can be populated from previous equations. Recalling equation (3.10) the first derivative with respect to segment length:

$$\frac{d\mathbf{r}}{ds} = \mathbf{T}$$

Recalling equation (3.12), the second derivative:

$$\frac{d^2 \mathbf{r}}{ds^2} = \frac{dT}{ds} = \kappa \mathbf{N}$$

Finally, deriving (3.12) the third derivative is found as:

$$\frac{d^3 \mathbf{x}}{ds^3} = \frac{d}{ds} (\kappa \mathbf{N}) = \frac{d\kappa}{ds} \mathbf{N} + \kappa \frac{d\mathbf{N}}{ds} = \frac{d\kappa}{ds} \mathbf{N} - \kappa^2 \mathbf{T} + \kappa \tau \mathbf{B} \quad (3.26)$$

Assuming zero initial condition for unit vectors:

$$\mathbf{T}(0) = (1, 0, 0) \quad \mathbf{N}(0) = (0, 1, 0) \quad \mathbf{B}(0) = (0, 0, 1) \quad (3.27)$$

Substituting equations (3.10), (3.12), (3.26), and (3.27) into (3.25) it leads to following representation:

$$\begin{aligned}\mathbf{r}(s) &= r(0) + s \mathbf{T} + \frac{s^2}{2} (\kappa \mathbf{N}) + \frac{s^3}{6} \left(\frac{d\kappa}{ds} \mathbf{N} - \kappa^2 \mathbf{T} + \kappa \tau \mathbf{B} \right) + o(s^3) \\ \mathbf{r}(s) &= \left(s - \frac{\kappa^2 s^3}{6} \right) \mathbf{T} + \left(\frac{s^2}{2} \kappa + \frac{d\kappa}{ds} \frac{s^3}{6} \right) \mathbf{N} + \left(\frac{\kappa \tau s^3}{6} \right) \mathbf{B} + o(s^3)\end{aligned}\quad (3.28)$$

Equation (3.28) can be split into its constituent components, leading to a canonical representation of a curve:

$$r_1(s) = s - \frac{\kappa^2}{6} s^3 + o(s^3) \quad (3.29)$$

$$r_2(s) = \frac{\kappa}{2} s^2 + \frac{d\kappa}{ds} \frac{1}{6} s^3 + o(s^3) \quad (3.30)$$

$$r_3(s) = \frac{\kappa \tau}{6} s^3 + o(s^3) \quad (3.31)$$

This canonical representation $\mathbf{r} = \mathbf{r}(\kappa, \tau)$, now contains the necessary parameters to be invariant, while being independent to the space curve case. However, the acceleration of the particle needs to be found such as equation (3.23). The necessary steps make use of (3.22) denoting the difference between deriving with respect to time and segment length. Assuming only first term approximations, the curve representation is:

$$\mathbf{a} = \frac{d^2}{dt^2} (s \mathbf{T}) + \frac{d^2}{dt^2} \left(\frac{\kappa}{2} s^2 \mathbf{N} \right) + \frac{d^2}{dt^2} \left(\frac{\kappa \tau}{6} s^3 \mathbf{B} \right) \quad (3.32)$$

The mathematical procedure is available on the Appendix A.1, but the resulting acceleration components are found to be:

$$\frac{d^2}{dt^2} (s \mathbf{T}) = ((1 - s \ddot{s} \kappa^2) \ddot{s} \mathbf{T} + 2 \dot{s}^2 \kappa \mathbf{N} + \tau \mathbf{B}) \quad (3.33)$$

$$\begin{aligned}
\frac{d^2}{dt^2} \left(\frac{\kappa}{2} s^2 \mathbf{N} \right) = & m \left(\left((\ddot{\kappa} \dot{s} \kappa + \ddot{\kappa}) \left(-\frac{1}{2} s^2 \right) + (\dot{s}^2 \kappa^2 + \kappa \dot{s})(-s) \right) \mathbf{T} \right. \\
& + \left. \left((\ddot{\kappa} - \kappa^3 \dot{s} - \kappa \tau^2 \dot{s}) \frac{1}{2} s^2 + 2s \dot{\kappa} \dot{s} + \kappa \dot{s}^2 + \kappa s \ddot{s} \right) \mathbf{N} \right. \\
& + \left. \left(\left(\frac{\ddot{\kappa}}{2} s \dot{s} + \kappa \dot{s}^2 + \frac{\dot{\kappa}}{2} s + \kappa \dot{s} \right) s \tau + \frac{\kappa}{2} s^2 \dot{\tau} \right) \mathbf{B} \right) \\
\frac{d^2}{dt^2} \left(\frac{\kappa \tau}{6} s^3 \mathbf{B} \right) = & \left(\left(\frac{1}{6} (\ddot{\kappa} \tau + 2\dot{\kappa} \dot{\tau} + \kappa \ddot{\tau}) s^3 + \left((\dot{\kappa} \tau + \kappa \dot{\tau}) \dot{s} + \frac{\kappa \tau}{2} \ddot{s} \right) s^2 + \kappa \tau s \dot{s}^2 \right) \mathbf{B} \right. \\
& - \left. \left(\frac{1}{6} (\dot{\kappa} \tau^2 \dot{s} + 2\kappa \tau \dot{\tau} \dot{s} + \kappa \tau^2 \ddot{s} - \kappa \tau^2 \dot{s}^2 + \dot{\kappa} \tau^2 \dot{s} + \kappa \dot{\tau} \dot{s} \tau) s^3 \right. \right. \\
& \left. \left. + \kappa \tau^2 \dot{s}^2 s^2 \right) \mathbf{N} \right)
\end{aligned} \tag{3.34}$$

Comparing the acceleration of the invariant form compared to (3.23), the level of mathematical complexity and numerical computations increases drastically. Thus, proving that analytical solutions for invariant curves are not satisfied in the current approach used to solve the acceleration components.

3.4 Bertrand (Parallel) Curves

When two curves share a common principal normal \mathbf{N} at any of their points, they are called Bertrand curves. If C is a plane (2D) curve, it is always possible to find a curve C' , such that C and C' are Bertrand curves. By definition of involute, all curves orthogonal to the tangents of C are located in the plane E [76]. Thus, if E is the plane evolute of C , all involutes C' of E have the same principal normal as C . If these statements are satisfied, the curves are parallel and with a constant distance separating them.

The relationship between curve C and C' can be expressed by a linear operation with a shared principal tangent such that if $C: r(s)$ and $C': r'(s)$, then the following equation can be used:

$$r' = r + dN \quad (3.36)$$

Where:

d = Constant distance between curves

N = Principal normal function

To verify the existence of a curve C' such that C and C' are parallel, the curvature and torsion of C have to satisfy the following linear relationship with constant coefficients:

$$a_1\kappa + a_2\tau = 1 \quad (3.37)$$

If the previous relation is verified, the parallel curve C' will have the following description where $d = a_1$:

$$r' = r + a_1N \quad (3.38)$$

In the special case of 2D curves, $\tau(s) = 0$ such that:

$$a_1 = \frac{1}{\kappa(s)} \quad (3.39)$$

Equation (3.39) can be plugged into equation (3.38) to obtain the following parallel curve relationship:

$$r'(s) = r(s) + \frac{N(s)}{\kappa(s)}$$

Thus, as long as the curvature of curve C is found, a curve C' can be found to be proportional to the curvature of C and its corresponding principal normal.

It is worth noting that design formulas used in street design as discussed in Chapter 2 employ many independent equations to avoid the analytical construction of these curves presented in this chapter. However, this tends to neglect the relationship that both street designs and differential curvature have. In this dissertation, the relationships between road design standards, and vehicle dynamics will be used to formulate a new guiding reference system for CAVs.

3.5 References

- [1] Andrews, S. (2012). Vehicle-to-Vehicle (V2V) and Vehicle-to-Infrastructure (V2I) Communications and Cooperative Driving. *Eskandarian A. (eds) Handbook of Intelligent Vehicles*. doi:https://doi.org/10.1007/978-0-85729-085-4_46
- [2] Jurgen, R. K. (2012). *V2V/V2I Communications for Improved Road Safety and Efficiency*. SAE International.
- [3] Oisin, D., & O'Mahony, M. (2018). Assessing the Benefits of Installing V2I Communications on an Urban Orbital Motorway in a Medium-Sized European City. *97th Annual Meeting of the Transportation Research Board*. Washington D.C.
- [4] Rahman, M. S., Abdel-Aty, M., Wang, L., & Lee, J. (2018). Understanding the Highway Safety Benefits of Different Approaches of Connected Vehicles in Reduced Visibility Conditions. *Journal of the Transportation Research Board*, 91-101. doi:10.1177/0361198118776113

- [5] WYDOT. (2020, May 16). *WYDOT Connected Vehicle Pilot Program*. Retrieved from <https://wydotcvp.wyoroad.info/>
- [6] VDOT. (2018). *Smarter Roads VDOT*. Retrieved 2020, from <https://smarterroads.org/login>
- [7] USDOT. (2020, June 30). *USDOT Intelligent Transportation Systems Office - Connected Vehicle Pilot Deployment Program*. Retrieved from <https://www.its.dot.gov/pilots/index.htm>
- [8] SAE. (2018). J3016 Taxonomy and Definitions for Terms Related to Driving Automation Systems for On-Road Motor Vehicles. *SAE International*, 35.
- [9] NHTSA. (2018). *Automated Vehicles for Safety*. (USDOT National Highway Traffic Safety Administration) Retrieved 2020, from nhtsa.gov: <https://www.nhtsa.gov/equipment/driver-assistance-technologies>.
- [10] Pendleton, S. D., Andersen, H., Du, X., Shen, X., Meghjani, M., Eng, Y. H., . . . Ang, M. H. (2017). Perception, Planning, Control, and Coordination for Autonomous Vehicles. *Machines*, 5(1). doi:10.3390/machines5010006
- [11] J. Kocić, N. Jovičić and V. Drndarević, "Sensors and Sensor Fusion in Autonomous Vehicles," 2018 26th Telecommunications Forum (TELFOR), Belgrade, Serbia, 2018, pp. 420-425, doi: 10.1109/TELFOR.2018.8612054.
- [12] Mohammed , A. S., Amamou , A., Ayevide, F. K., Kelouwani, S., Agbossou, K., & Zioui, N. (2020, November). The Perception System of Intelligent Ground

- Vehicles in All Weather Conditions: A Systematic Literature Review. *Sensors (Basel)*, 20(22). doi:10.3390/s20226532
- [13] Zang, S., Ding, M., Smith, D., Tyler , P., Rakotoarivelo, T., & Kaafar, M. A. (2019, March 12). The Impact of Adverse Weather Conditions on Autonomous Vehicles. IEEE Vehicular Technology Magazine. doi:10.1109/MVT.2019.2892497
- [14] Claussmann, L., Revilloud, M., Gruyer, D., & Glaser, S. (2019). A Review of Motion Planning for Highway Autonomous Driving. IEEE Transactions on Intelligent Transportation Systems, 21(5), 1826 - 1848. doi:10.1109/TITS.2019.2913998
- [15] González, D., Pérez, J., Milanés, V., & Nashashibi, F. (2015, November). A Review of Motion Planning Techniques for Automated Vehicles. IEEE Transactions on Intelligent Transportation Systems, 17(4), 1135 - 1145. doi:10.1109/TITS.2015.2498841
- [16] Jeon, S.J., Kang, C.M., Lee, S., & Chung, C. (2015). GPS waypoint fitting and tracking using model predictive control. *2015 IEEE Intelligent Vehicles Symposium (IV)*, 298-303.
- [17] Bétaille, D., & Toledo-Moreo, R. (2010). Creating Enhanced Maps for Lane-Level Vehicle Navigation. IEEE Transactions on Intelligent Transportation Systems, 11(4), 786 - 798. doi: 10.1109/TITS.2010.2050689
- [18] Guo, C., Kidono, K., Meguro, J., Kojima, Y., Ogawa, M., & Naito, T. (2016). A Low-Cost Solution for Automatic Lane-Level Map Generation Using Conventional

- In-Car Sensors. *IEEE Transactions on Intelligent Transportation Systems*, 17(8), 2355 - 2366. doi:10.1109/TITS.2016.2521819
- [19] Chen, A., Ramanandan, A., & Farrell, J. A. (2010). High-precision lane-level road map building for vehicle navigation. *Position Location and Navigation Symposium (PLANS), 2010 IEEE/ION*. IEEE Xplore. doi:10.1109/PLANS.2010.5507331
- [20] Gwon, G.-P., Hur, W.-S., Kim, S.-W., & Seo, S.-W. (2016). Generation of a Precise and Efficient Lane-Level Road Map for Intelligent Vehicle Systems. *IEEE Transactions on Vehicular Technology*, 66(6), 4517 - 4533. doi:10.1109/TVT.2016.2535210
- [21] Huang, A. S., Moore, D., Antone, M., Olson, E., & Teller, S. J. (2008). Multi-Sensor Lane Finding in Urban Road Networks. *Robotics: Science and Systems IV*, Eidgenössische Technische Hochschule Zürich. Zürich. doi:10.15607/RSS.2008.IV.001
- [22] Li, K., Tan, H.-S., Misener, J. A., & Hedrick, J. K. (2008). Digital map as a virtual sensor – dynamic road curve reconstruction for a curve speed assistant. *Vehicle System Dynamics*, 1141–1158. doi:10.1080/00423110701837110
- [23] Liu, C., Jiang, K., Yang, D., & Xiao, Z. (2016). Design of a Multi-layer Lane-Level Map for Vehicle Route Planning. *MATEC Web of Conferences*, 124(1). doi:10.1051/matecconf/201712403001
- [24] Reeds J. and Shepp L. (1990). Optimal paths for a car that goes both forwards and backwards. *Pacific J. Math.*, vol. 145, no. 2, pp. 367–393.

- [25] Hsieh M. F. and Ozguner U. (2008). A parking algorithm for an autonomous vehicle. *Proc. IEEE Intell. Veh. Symp.*, pp. 1155–1160.
- [26] Villagra J., Milanes V., Rastelli, J. P., Godoy, J., and Onieva E. (2012) Path and speed planning for smooth autonomous navigation. *IEEE Intelligent Vehicles Symposium (IV)*.
- [27] Vanholme B., Gruyer D., Lusetti B., Glaser S., and Mammar S. (2013) Highly automated driving on highways based on legal safety. *IEEE Trans. on Intelligent Transportation Systems*, vol. 14, no. 1, pp. 333–347.
- [28] Cherubini A., Spindler F., and Chaumette F. (2012). A new tentacles-based technique for avoiding obstacles during visual navigation, in *IEEE Int. Conf. on Robotics and Automation (ICRA)*.
- [29] Funke J. et al. (2012). Up to the limits: Autonomous Audi TTS. *Proc. IV Symp*, pp. 541–547.
- [30] Fraichard T. and Scheuer A. (2004). From Reeds and Shepp’s to continuous curvature paths. *IEEE Trans. Robot.*, vol. 20, no. 6, pp. 1025–1035.
- [31] Broggi A., Medici P., Zani P., Coati A., and Panciroli M. (2012). Autonomous vehicles control in the vislab intercontinental autonomous challenge. *Annu. Rev. Control*, vol. 36, no. 1, pp. 161–171.
- [32] Vorobieva H., Minoiu-Enache N., Glaser S., and Mammar S. (2013). Geometric continuous-curvature path planning for automatic parallel parking. *Proc. IEEE 10th ICNSC*, pp. 418–423.

- [33] Vorobieva, H., Glaser S., Minoiu-Enache N., and Mammar S. (2014). Automatic parallel parking with geometric continuous-curvature path planning. *Proc. IEEE Intell. Veh. Symp.*, pp. 465–471.
- [34] Fuji H., Xiang J., Tazaki Y., Levedahl B., and Suzuki T. (2014). Trajectory planning for automated parking using multi-resolution state roadmap considering non-holonomic constraints. *Proc. IEEE Intell. Veh. Symp.*, pp. 407–413.
- [35] Brezak M. and Petrovic I. (2014). Real-time approximation of clothoids with bounded error for path planning applications. *IEEE Trans. Robot.*, vol. 30, no. 2, pp. 507–515.
- [36] Coombs D., Murphy K., Lacaze A., and Legowik S. (2000). Driving autonomously off-road up to 35 km/h. *Proc. IEEE IV Symp.*, pp. 186–191.
- [37] Lima P. F., Trincavelli M., Martensson J., and Wahlberg B. (2015). Clothoid based speed profiler and control for autonomous driving. *IEEE Int. Conf. on Intelligent Transportation Systems (ITSC)*.
- [38] Chebly A., Tagne G., Talj R., and Charara A. (2015). Local trajectory planning and tracking of autonomous vehicles, using clothoid tentacles method. *IEEE Intelligent Vehicles Symposium (IV)*.
- [39] Sheckells M., Caldwell T. M., and Kobilarov M. (2017) Fast approximate path coordinate motion primitives for autonomous driving. *IEEE Annual Conf. on Decision and Control (CDC)*, 2017.
- [40] Mouhagir H., Talj R., Cherfaoui V., Aioun F., and Guillemard F. (2016). Integrating safety distances with trajectory planning by modifying the occupancy

- grid for autonomous vehicle navigation. *IEEE Int. Conf. on Intelligent Transportation Systems (ITSC)*.
- [41] McNaughton M., Urmson C., Dolan J., and Lee J.-W. (2011). Motion planning for autonomous driving with a conformal spatiotemporal lattice. *Proc. IEEE ICRA*, pp. 4889–4895.
 - [42] Petrov P. and Nashashibi F. (2014). Modeling and nonlinear adaptive control for autonomous vehicle overtaking. *IEEE Trans. Intell. Transp. Syst.*, vol. 15, no. 4, pp. 1643–1656.
 - [43] Piazz A., Lo Bianco C. G., Bertozzi M., Fascioli A., and Broggi A. (2002). Quintic g^2 -splines for the iterative steering of vision-based autonomous vehicles. *IEEE Trans. Intell. Transp. Syst.*, vol. 3, no. 1, pp. 27–36.
 - [44] Glaser S., Vanholme B., Mammar S., Gruyer D., and Nouveliere L., (2010) Maneuver-based trajectory planning for highly autonomous vehicles on real road with traffic and driver interaction. *IEEE Trans. Intell. Transp. Syst.*, vol. 11, no. 3, pp. 589–606.
 - [45] Lee J. W. and Litkouhi B. (2012). A unified framework of the automated lane centering/changing control for motion smoothness adaptation. *Proc. 15th IEEE Int. ITSC*, pp. 282–287.
 - [46] Simon A. and Becker J., (1999). Vehicle guidance for an autonomous vehicle. *Proc. IEEE/IEE/JSAI Int. Conf. Intell. Transp. Syst.*, pp. 429–434.
 - [47] Keller C. G. et al., (2011). Active pedestrian safety by automatic braking and evasive steering. *IEEE Trans. Intell. Transp. Syst.*, vol. 12, no. 4, pp. 1292–1304.

- [48] Gu T., Snider J., Dolan J., and Lee J.-W. (2013). Focused trajectory planning for autonomous on-road driving. *IEEE Intelligent Vehicles Symposium (IV)*.
- [49] Tehrani H., Do Q. H., Egawa M., Muto K., Yoneda K., and Mita S. (2015). General behavior and motion model for automated lane change. *IEEE Intelligent Vehicles Symposium (IV)*.
- [50] McNaughton M., Urmson C., Dolan J. M., and Lee J.-W. (2011). Motion planning for autonomous driving with a conformal spatiotemporal lattice. *IEEE Int. Conf. on Robotics and Automation (ICRA)*.
- [51] Xu W., Wei J., Dolan J. M., Zhao H., and Zha H. (2012). A real-time motion planner with trajectory optimization for autonomous vehicles. *IEEE Int. Conf. on Robotics and Automation (ICRA)*.
- [52] Bacha A. et al. (2008). Odin: Team Victortango's entry in the DARPA urban challenge. *J. Field Robot.*, vol. 25, no. 8, pp. 467–492.
- [53] Trepagnier P. G., Nagel J., Kinney P. M., Koutsougeras C., and Dooner M. (2006). Kat-5: Robust systems for autonomous vehicle navigation in challenging and unknown terrain. *J. Field Robot.*, vol. 23, no. 8, pp. 509–526.
- [54] Shiller Z. and Gwo Y.-R. (1991). Dynamic motion planning of autonomous vehicles. *IEEE Trans. Robot. Autom.*, vol. 7, no. 2, pp. 241–249.
- [55] Berglund T., Brodnik A., Jonsson H., Staffanson M., and Soderkvist I. (2010). Planning smooth and obstacle-avoiding b-spline paths for autonomous mining vehicles. *IEEE Trans. Autom. Sci. Eng.*, vol. 7, no. 1, pp. 167–172.

- [56] Schubert R., Scheunert U., and Wanielik G., (2008). Planning feasible vehicle maneuvers on highways. *IET Intelligent Transport Systems*, vol. 2, no. 3, pp. 211–218.
- [57] Ziegler J. and Stiller C. (2009). Spatiotemporal state lattices for fast trajectory planning in dynamic on-road driving scenarios. *IEEE/RSJ Int. Conf. on Intelligent Robots and Systems (IROS)*.
- [58] Gonzalez D., Perez J., Lattarulo R., Milanes V., and Nashashibi F. (2014). Continuous curvature planning with obstacle avoidance capabilities in urban scenarios. *Proc. IEEE 7th Int. ITSC*, pp. 1430–1435.
- [59] Perez J., Lattarulo R., and Nashashibi F. (2014). Dynamic trajectory generation using continuous-curvature algorithms for door-to-door assistance vehicles. *Proc. IEEE Intell. Veh. Symp*, pp. 510–515.
- [60] Pérez J., Godoy J., Villagra J., and Onieva E. (2013). Trajectory generator for autonomous vehicles in urban environments. *Proc. IEEE ICRA*, pp. 409–414.
- [61] Han L., Yashiro H., Nejad H. T. N., Do Q. H., and Mita S. (2010). Bezier curve-based path planning for autonomous vehicle in urban environment. *Proc. IV Symp.*, pp. 1036–1042.
- [62] Liang Z., Zheng G., and Li J. (2012). Automatic parking path optimization based on bezier curve fitting. *Proc. IEEE ICAL*, pp. 583–587.
- [63] Montes N., Herraez A., Armesto L., and Tornero J. (2008). Real-time clothoid approximation by rational bezier curves. *Proc. IEEE ICRA*, pp. 2246–2251.
- [64] Montes N., Mora M., and Tornero J. (2007). Trajectory generation based on rational bezier curves as clothoids. *Proc. IEEE Intell. Veh. Symp*, pp. 505–510.

- [65] Choi J., (2014). Kinodynamic motion planning for autonomous vehicles. *Int. J. of Advanced Robotic Systems*, vol. 11, no. 6, p. 90.
- [66] Chen J., Zhao P., Mei T., and Liang H. (2013). Lane change path planning based on piecewise bezier curve for autonomous vehicle. *IEEE Int. Conf. on Vehicular Electronics and Safety (ICVES)*.
- [67] Huy Q., Mita S., Nejad H. T. N., and Han L. (2013). Dynamic and safe path planning based on support vector machine among multi moving obstacles for autonomous vehicles. *IEICE Trans. on Information and Systems*, vol. 96, no. 2, pp. 314–328.
- [68] NHTSA. (2016). *Fatal Accident Reporting System (FARS) Encyclopedia*. Retrieved from National Highway Transportation Safety Administration: <http://www-fars.nhtsa.dot.gov/Main/index.aspx>
- [69] IIHS. (2018). *Roadway and environment: Fatality Facts*. Retrieved from Insurance Institute for Highway Safety, Highway Loss Data Institute: <https://www.iihs.org/topics/fatality-statistics/detail/collisions-with-fixed-objects-and-animals>
- [70] Stolle, C. S., Lechtenberg, K. A., Faller, R. K., & Yim, T. (2017). Initial Developments Supporting a Roadside Tree Removal Safety Campaign. *Journal of the International Conference of Roadside Safety*.
- [71] AASHTO. (2011). *A Policy on Geometric Design of Highways and Streets (The Green Book)* (Sixth Edition ed.). Washington D.C.: American Association of State Highway and Transportation Officials.

- [72] IDOT. (2010). *Street Design Manual: Spiral Curves*. Iowa Department of Transportation.
- [73] WYDOT. (2011). *Horizontal Alignment and Superelevation*.
- [74] Gillespie, T. D. (1992). *Fundamentals of Vehicle Dynamics*. SAE International.
- [75] Pacejka, H. B. (2006). *Tyre and Vehicle Dynamics*. Butterworth-Heinemann.
- [76] Kreyszig, E. (1991). *Differential Geometry* (1st ed.). Dover Publications.
- [77] do Carmo, M. P. (1976). *Differential Geometry of Curves and Surfaces*. Englewood Cliffs, N.J: Prentice-Hall.
- [78] Pressley, A. N. (2010). *Elementary Differential Geometry*. London: Springer Undergraduate Mathematics Series. doi:10.1007/978-1-84882-891-9
- [79] Meriam, J. L., & Kraige, L. G. (2002). *Engineering Mechanics, Dynamics*. Wiley, John & Sons, Incorporated.

CHAPTER 4. ROAD CURVATURE DECOMPOSITION FOR AUTONOMOUS GUIDANCE

Ricardo O. Jacome*, Cody S. Stolle, and Michael Sweigard

*The University of Nebraska – Lincoln, Department of Mechanical Engineering, Lincoln, NE 68588

Abstract

Vehicle autonomy is critically dependent on an accurate identification and mathematical representation of road and lane geometries. Many road lane identification systems are ad hoc (e.g., machine vision and lane keeping systems) or utilize finely-discretized path data and vehicle tracking systems such as GPS. A novel Midwest Discrete Curvature (MDC) method is proposed in which geodetic road data is parsed along road directions and digitally stored in a road data matrix. Road data is discretized to geospatial points and curvature and road tangent vectorization, which can be utilized to generate consistent, mathematically-defined road profiles with deterministic boundary conditions, consistent non-holonomic boundary constraints, and a smooth, differentiable path which connects critical road coordinates. The method was evaluated by discretizing three road segments: a hypothetical road consistent with the American Association of State Highway and Transportation Officials (AASHTO) Green Book design standards, a road segment discretized using satellite photography and GPS data points, and an in-vehicle GPS trace collected at 10 Hz. Improvements and further research were recommended to expand findings, but results indicated potential for implementation into road modeling which could be the foundation of new autonomous vehicle guidance systems that are complimentary to existing autonomous systems.

Keywords: Trajectory Generation, Path Generation, Curvature, AASHTO, V2I, Vehicle-to-Infrastructure

4.1 Introduction

4.1.1 Motivation

Vehicle autonomy has been touted as the future of transportation, but there are significant challenges which remain to be addressed. The electronic replacement or augmentation of dynamic driving tasks performed by human drivers, such as steering, braking, and applying throttle, requires the accurate perception of the environment, potential safety risks in a decision tree, and selection of optimal outcomes [1].

Driving augmentation devices, collectively termed “Advanced Driver Assistance Systems” or ADAS, have undergone tremendous growth and development [2]. Safety organizations such as the Institute for Highway Safety (IIHS), Highway Loss Data Institute (HLDI), and the National Highway Traffic Safety Administration reviewed recent U.S. traffic data and confirmed that ADAS systems directly contributed to an overall reduction in annual crashes, and likely prevented deaths and serious injuries [3][4].

However, road navigation remains the biggest hurdle for fully-autonomous vehicle implementation. Current vehicle guidance techniques have relied on one of two possible techniques: high-precision tracking using a redundant network of position tracking sensors in low-speed, urban environments; and lane edge identification using either Light Detection and Ranging (LIDAR) or machine optics. Both techniques develop an ad hoc estimation of the desired position within a lane (i.e., the lane centerline), estimate the vehicle’s current offset from that desired path, and identify what corrective factors are necessary for the vehicle’s trajectory to rejoin the desired path. Therefore, before

determining what vehicle controls are necessary to follow a target path, the geometry of the target path must first be identified.

A research study conducted at the University of Nebraska-Lincoln (UNL) identified techniques for generating a highly-accurate, algorithmic road path which could be utilized within a framework of autonomous vehicle operations or as a driver assistance system. The system utilizes precisely-mapped road path coordinates, vehicle-to-roadside infrastructure (V2I) wireless communication to relay updates in road path and to assist with vehicle triangulation, and a vehicle positioning and reaction algorithm.

The objective of this paper is to describe the framework for identifying boundary conditions for highly accurate road path descriptions, including geospatial and non-holonomic boundary conditions, and to use those boundary conditions to formulate highly accurate mathematical representations of lane corridors. The lane paths must be smooth, differentiable, and comprise deterministic and reproducible representations of geospatial road data.

4.1.2 Path Prediction in Autonomous Vehicles

In this paper, a path is defined a connection in between two points (i.e. Point A to Point B). Any curve which connects two points is therefore a possible path, as shown in Figure 4.1. The optimized path is identified as the path which closely follows the geometry of a lane centerline, is continuous and differentiable across segments, and minimizes mathematical instabilities or irregularities. Vehicle trajectory is defined as the path that the vehicle CG follows between two points (i.e., trace-line).

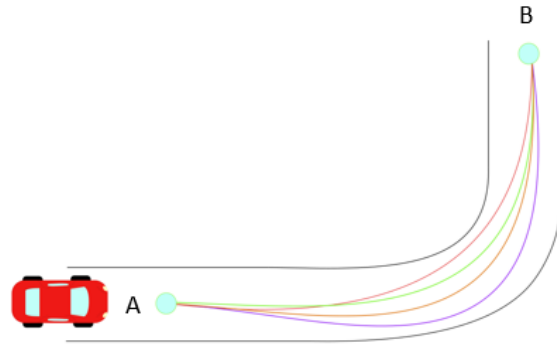


Figure 4.1 Different Trajectories in Path from Point A to Point B.

Human and autonomous drivers both operate the vehicle using Path Planning, which consists of the estimation of the vehicle's future trajectory given the vehicle's current position, velocity, acceleration, and operational constraints. Characteristically, optimal paths are selected based on the evaluation of path intersections of traversable and non-traversable zones, as well as the evaluation of input controls required to produce the trajectory. Path planning for vehicles and robotics applications utilize physics models, geospatial curve modeling and estimation, and feedback controls [5].

Path planning applied to vehicle guidance may include sampling-based planning, which uses sampling from sensors to create a path based on limited data sets; probabilistic methods, which rely on approximating the free space available for navigation such as Probabilistic Road Maps and Rapidly Exploring Random Trees [5][6]; and Phase Space Planning, which incorporates different sampling-based planning algorithms and compares them to extract the most optimal path [6].

All currently implemented Path Planning algorithms for autonomous vehicle controls rely on narrow sample spacing to limit error. Path planning formulations are either ad hoc (e.g., LIDAR, machine vision) or driven by low-speed, continuously-monitored GNSS

triangulation with external ground-based monitoring compared to a highly-discretized road coordinate map. Vehicle sensors are also used to generate navigational maps, for example, discretizing areas of space from an image to determine if they are feasible for navigation.

During on-road driving, parameters such as velocity and acceleration dictate which possible paths may result in feasible trajectories. Path descriptions have been described using variational methods, clothoids, and velocity profiles [7][8][9]. Variational methods arise from optimizing functionals with non-holonomic constraints (i.e., constraints on the velocity and acceleration) [10]. These methods yield polynomial solutions of high order that are treated as boundary value problems (BVP) during vehicle navigation [11][12]. Clothoid functions (Cornu Spirals or Euler Spiral), and spline functions are also studied in autonomous research because of their effectiveness in connecting a straight line with a constant radius curve [13][14][15].

These trajectory estimates are then combined with optimization theory to be implemented into controllers for navigation purposes [16]. In general, these trajectories focus on providing a continuous function (up to the third derivative) while being smooth (i.e., minimizing the jerk $\frac{d^3x}{dt^3}$) [17][18].

4.2 Method Formulation

4.2.1 Vehicle Dynamics and Road Design

Researchers utilized principles of vehicle dynamics in order to generate a road mapping technique which would automatically resolve limitations on vehicle stability and control. It was noted that all vehicle-road interactions are governed by the force generated at the wheels, and all vehicle controls are dictated by the direction and magnitude of friction force

[19][20]. Using Newton's 2nd Law, those forces can be related to the fundamental kinematic constraints of path motion.

A Frenet-Serret reference frame is used along with unit vectors of \mathbf{N} (normal), \mathbf{T} (tangential), and \mathbf{B} (binormal, out of plane), as shown in Figure 4.2. For this paper, it is assumed that the vehicle navigates on a 2D Euclidean Space.

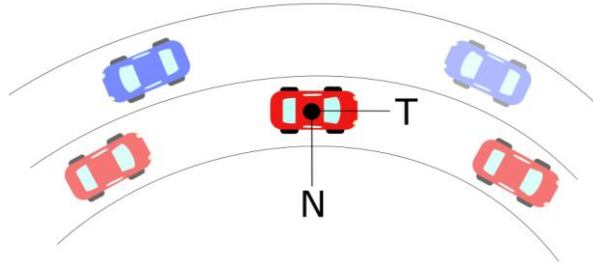


Figure 4.2 Normal-Tangential Coordinates Example in Vehicle's Center of Mass.

The net acceleration acting on the vehicle at an instant in time is described by the time variance of the path. These limits are related to the acceleration of a vehicle under circular motion, which is denoted as:

$$\mathbf{a} = \dot{v} \mathbf{T} + \kappa v^2 \mathbf{N}$$

Where:

\mathbf{a} = Total acceleration of vehicle (m/s^2)

v = Tangential velocity of vehicle (m/s)

κ = Curvature at an instantaneous point (m^{-1})

\mathbf{N} = Normal unit vector

\mathbf{T} = Tangential unit vector

Longitudinal accelerations are produced by a net longitudinal force, which either increases or decreases vehicle speed. Lateral accelerations in the normal direction

(perpendicular to the velocity vector) do not affect speed and instead turn the vehicle's trajectory. Lateral forces are generated during turns and from road cross-section geometry (superelevation, banks, crowning). Curvature κ , which is the reciprocal of the radius of curvature, is related to the instantaneous rate of change of the tangential unit vector T with respect to time or distance traveled [21][22][23].

In recognition of measurable data on the vehicle and vehicle dynamics constraints, AASHTO standardized road designs which control for tire-pavement friction using equations for superelevation, crowning, and turn radius [24]. These road design parameters are based on numerous historical studies of driver tolerance for lateral accelerations [25]. Speed limits are controlled on roadways based on measured reductions in friction during wet travel conditions [26]. Hence, the Frenet-Serret coordinates are highly compatible with onboard vehicle systems and prevailing road geometrical design.

Moreover, determining target vehicle path geometries using Frenet-Serret formulation is highly conducive for autonomous vehicle control systems. For example, accelerometers measure acceleration along principal axes; rate transducers record vehicle angular rates of change; gyroscopes identify instantaneous vehicle inclinations; wheel sensors and GPS are useful for estimating current speeds; and steering wheel rotational sensors can detect wheel steer angles. Wheel steer angles can be related to the instantaneous curvature using Ackerman estimates and corrections for understeer gradient [19][20]. For vehicles whose orientation closely follows the roadway tangent vector T , the lateral acceleration can provide an additional evaluation of the instantaneous curvature of the vehicle.

Researchers developed target path geometry constraints using Frenet-Serret coordinates in local space and then mapped those coordinates to the surface of the earth

using transformation matrices based on GPS coordinates. Thus, curvature can be expressed in a vector form that has a direction parallel to the Normal Unit Vector shown in Figure 4.3. Similarly, a vector perpendicular to the curvature direction will provide a velocity tangent vector approximation at that point. This velocity vector provides a heading angle to the desired trajectory that is needed to follow a road path. Researchers therefore generated mathematical relationships to identify the non-holonomic constraints which aligned with Frenet-Serret formulation using discrete geospatial point data.

4.2.2 Spatial Curvature Formulation

The instantaneous curvature of a geospatial point (deemed “A”) was obtained using the spatial coordinates of adjacent points. The technique may be scaled with smaller or larger segmentation, leading to an optimized computational cost, $O(n)$ [27].

Let a scalene triangle with corners A, B, and C have a circumscribed circle of radius ρ in Euclidean 2D space as shown in Figure 4.3. The vertices of the triangle are connected using vectors AB, AC, and BC.

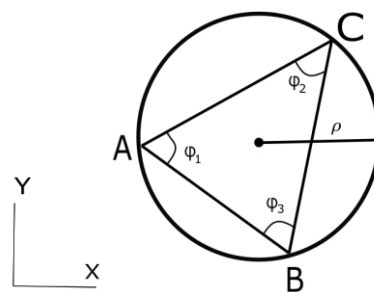


Figure 4.3 Circumscribed Circle in Scalene Triangle.

A vector \mathbf{AD} , equal to the cross product in between the vectors \mathbf{AB} and \mathbf{AC} , will be normal to the plane defined by the intersection of \mathbf{AB} and \mathbf{AC} . The magnitude for vector \mathbf{AD} may be identified based on the cross product:

$$\|\mathbf{D}\| = \|\mathbf{AB} \times \mathbf{AC}\| = \|\mathbf{AB}\| \|\mathbf{AC}\| \sin \phi_1$$

Let a vector \mathbf{E} be the cross product of \mathbf{AD} with the vector \mathbf{AB} defining this new vector in the direction of \mathbf{e} , as shown in red in Figure 4.4. The magnitude of vector \mathbf{E} is defined as:

$$\|\mathbf{E}\| = \|\mathbf{D} \times \mathbf{AB}\| = \|\mathbf{AB}\|^2 \|\mathbf{AC}\| \sin \phi_1$$

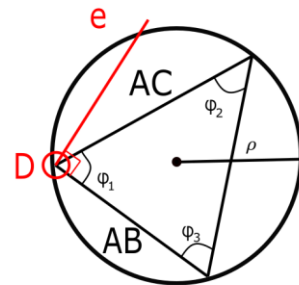


Figure 4.4 First Unit Vector Direction on Triangle.

Similarly, let a vector \mathbf{F} be the cross product of \mathbf{AD} with the vector \mathbf{AC} , defining this new vector in the direction of \mathbf{f} shown in blue in Figure 4.5. The magnitude of vector \mathbf{f} is defined as:

$$\|\mathbf{F}\| = \|\mathbf{D} \times \mathbf{AC}\| = \|\mathbf{AB}\| \|\mathbf{AC}\|^2 \sin \phi_1$$

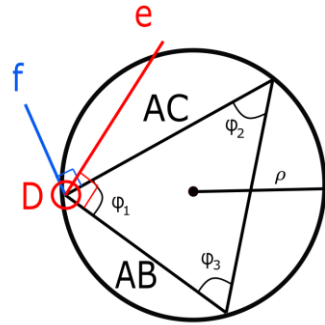


Figure 4.5 First- and Second-Unit Vectors on Triangle.

The unit vectors of e and f are defined by the following:

$$e = \frac{E}{\|AB\|^2 \|AC\| \sin \phi_1}$$

$$f = \frac{F}{\|AB\| \|AC\|^2 \sin \phi_1}$$

The midsection of any triangle's side intersects with each other at a point P corresponding to the center of the circle inscribing points A, B, and C. These intersecting lines denote two triangles with the same angle ϕ_1 in between the unit vectors and their corresponding midsections, as shown in Figure 4.6.

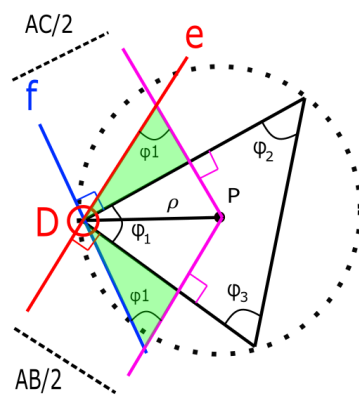


Figure 4.6 Radius of Curvature obtained from Geometric Relationships.

From these triangles, the radial vector AP may be described using components along unit vectors \mathbf{e} and \mathbf{f} . As a result, vector AP is described as:

$$AP_1 = \frac{AC}{2 \sin \phi_1} e = \frac{E}{2\|AB\|^2 \sin^2 \phi_1}$$

$$AP_2 = \frac{-AB}{2 \sin \phi_1} f = \frac{-F}{2\|AC\|^2 \sin^2 \phi_1}$$

From our previous definition of the vector AD, it is possible to simplify further:

$$AP_1 = \frac{\|AC\|^2 E}{2\|D\|^2}$$

$$AP_2 = \frac{-\|AB\|^2 F}{2\|D\|^2}$$

With these components, it is possible to obtain the magnitude as follows:

$$AP = \frac{\|AC\|^2 E}{2\|D\|^2} - \frac{\|AB\|^2 F}{2\|D\|^2}$$

$$\rho = \frac{\|AC\|^2 E - \|AB\|^2 F}{2\|D\|^2}$$

Using previous definitions of E and F:

$$\rho = \frac{\|AC\|^2 \|AD \times AB\| - \|AB\|^2 \|AD \times AC\|}{2\|D\|^2}$$

Using previous definition of AD, it is possible to obtain the radius of the prescribed circle in terms of only the difference in between points A, B and C.

$$\rho = \frac{\|AC\|^2 \|(AB \times AC) \times AB\| - \|AB\|^2 \|(AB \times AC) \times AC\|}{2\|(AB \times AC)\|^2} \quad (4.1)$$

Noting that $\kappa = 1/\rho$, it is possible to calculate curvature as:

$$\kappa = \frac{2\|(AB \times AC)\|^2}{\|AC\|^2\|(AB \times AC) \times AB\| - \|AB\|^2\|(AB \times AC) \times AC\|} \quad (4.2)$$

This process can be executed for small and large spacing between consecutive points along a curve, as shown in Figure 4.7. As a result, both finely-sampled and coarsely-sampled data may be utilized to generate geospatial curvature maps.

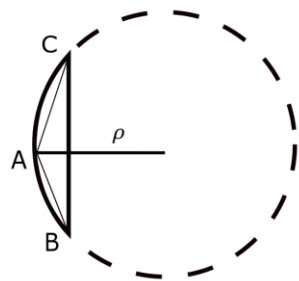


Figure 4.7 Scalene Triangle in Small Arc-Segment.

Curvature is related to the second-order differential of position and has strong association with the limits on lateral acceleration. Given that the second order differential equations are used to condition non-holonomic boundary conditions, determination of instantaneous curvature provides half of the data needed to fully define smooth, continuous, and deterministic target path formulations.

In addition to the second order curvature-based non-holonomic constraint, a 1st-order boundary condition was also identified based on the roadway tangent vector. The roadway tangent vector, T, is determined using an orthogonal phase shift of the curvature vector, such that:

$$T = \frac{(AD \times \kappa)}{\|(AD \times \kappa)\|} \quad (4.3)$$

Imposing local curvature and tangent coordinate vectors at each geospatial road data-point ensures that the target road path will be consistent with Frenet-Serret formulation. Then, roadway data checking can be performed to ensure that the curvature and point data is consistent with road design parameters and useful for identifying potential errors or skew datasets.

4.2.3 Segment Length Estimation

Between each consecutive set of geospatial points, the optimized roadway target path length, s , may be known to assist with relating vehicle current position to an equivalent position along the roadway target path. This error calculation is essential for determining if the vehicle's trajectory angle, speed, and current position combination put the vehicle at risk of departing the lane or roadway.

The length of each segment of the road path may be identified using the fundamental determination of arc length to radius based on included angle. The arc-length s of a curve is defined as the length traveled by the angle θ along a constant radius ρ :

$$\theta = \frac{s}{\rho}$$

Recalling curvature is the inverse of the radius of curvature, it follows that:

$$\theta = \kappa s$$

A differential form may be used to relate the change in angle to the segment length, s :

$$ds = \frac{d\theta}{\kappa}$$

By separation of variables and integration:

$$\int ds = \int \frac{d\theta}{\kappa}$$

Finally, the segment lengths can be determined through numerical integration of the curvature and angle changes:

$$\Delta s = \int \frac{d\theta}{\kappa} \quad (4.4)$$

4.2.4 Road Curvature Decomposition

The curvature formulation shown in (4.2) and road segment calculations shown in (4.4) may be applied to a discrete point cloud collected from a road geometry to determine the instantaneous curvature for every point, except at terminal ends of roadways. An example of the determination of curvature is shown in Figure 4.8.

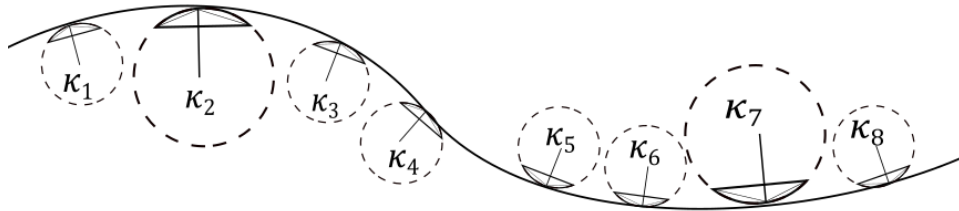


Figure 4.8 Road with Discrete Curvature Sections.

When roadway curvature is tangent, the curvature evaluates to zero and is stable; in contrast, the instantaneous radius of curvature of a tangent road is infinite for a 2D Cartesian map or may be related to the earth radius in 3D maps. An example of the radius vector map is shown in Figure 4.9.

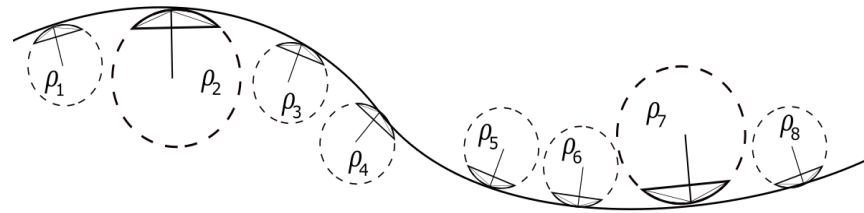


Figure 4.9 Road with Discrete Radius of Curvature Sections.

With the use of different technologies such as Aerial Photography, LIDAR scanning, GPS collection, or Road Surveying, it is possible to obtain a geospatial map of roadway centerlines or roadway lane edges (or limits of travelway for rural, unmarked roads). This data may be processed to identify the instantaneous curvature and heading angle of road points, and the segment length connecting consecutive points on the roadway. Continuous mathematical curve formulations may then be used to connect the geospatial point data in accordance with the curvature and heading angle calculations calculated previously. An example of this technique would be a parametric polynomial representation for X and Y road coordinates. An example of the road curvature decomposition scheme is represented in Figure 4.10.

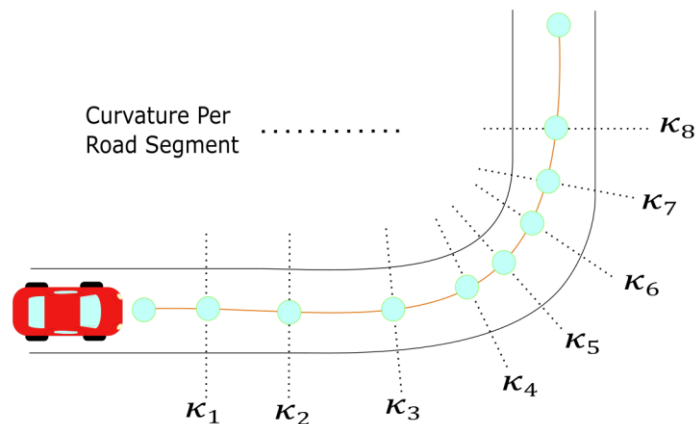


Figure 4.10 Road Curvature Decomposition Example.

Using the discrete curvatures calculated for each point, a piecewise-linear, continuous curvature model was developed. Road profiles may be deterministically modeled using relationships for curvature points, heading angles, and roadway segment lengths. Application of this technique to the creation of target paths was deemed the “Midwest Discrete Curvature” (MDC) method. The efficacy of this method in estimating road profiles was evaluated in the following sections.

4.3 Implementation

Typical highway roads are designed based on AASHTO guidelines to provide a natural, easy-to-follow path for drivers, such that the lateral accelerations increase and decrease gradually as the vehicle begins and ends curved road segments [24]. The continuity of the road curvature and adaptability for road tangents using the MDC method were compared by calculating the curvature throughout a road segment constructed consistently with AASHTO design guidelines, then compared using real-world data from satellite photography and point selection as well as GPS data.

4.3.1 Roadway Decomposition: AASHTO Base Model

This model strictly used AASHTO guidelines to design an ideal highway road for a vehicle traversing at constant 60 mph. The curve consisted of five different sections that can be classified as: straight section, entrance transition, constant radius curve, exit transition, and straight section. The road path constructed in accordance with AASHTO Green Book design guidelines is shown schematically in Figure 4.11.

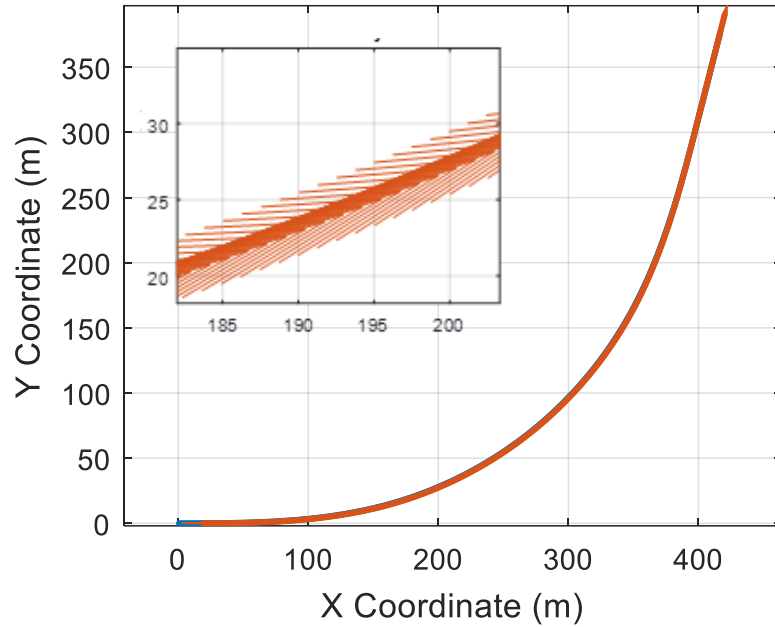


Figure 4.11 Finely-Discretized AASHTO Base Model: Road with Velocity Vectors.

Applying the MDC approach to this curve, curvature vectors were plotted with respect to the road segments, as shown Figure 4.12. The curvature magnitude was plotted with respect to road segments to obtain a base curvature profile, as shown in Figure 4.13.

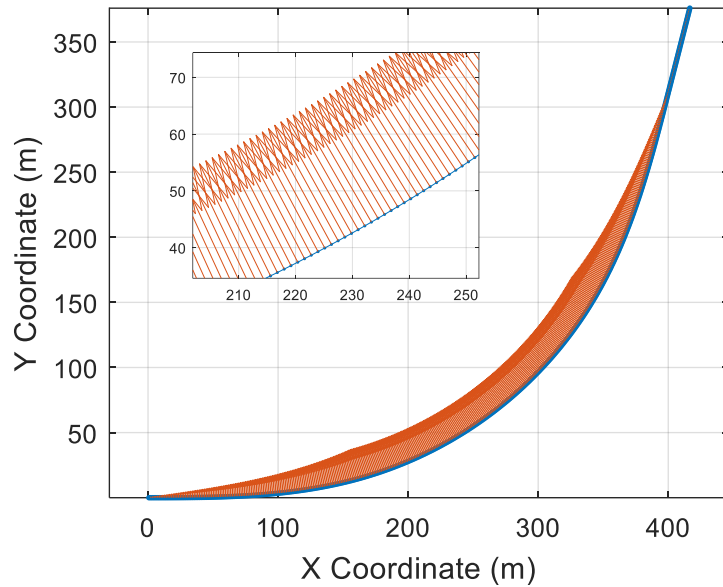


Figure 4.12 Finely-Discretized AASHTO Base Model: Road with Curvature Vectors.

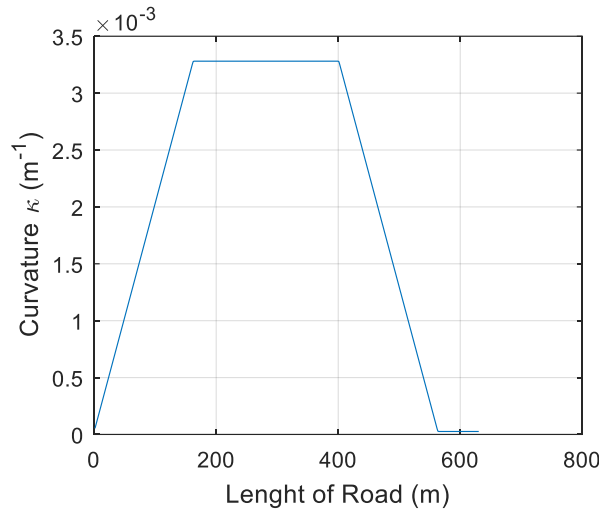


Figure 4.13 Finely-Discretized AASHTO Base Model: Curvature κ vs. Cumulative Curve

Length.

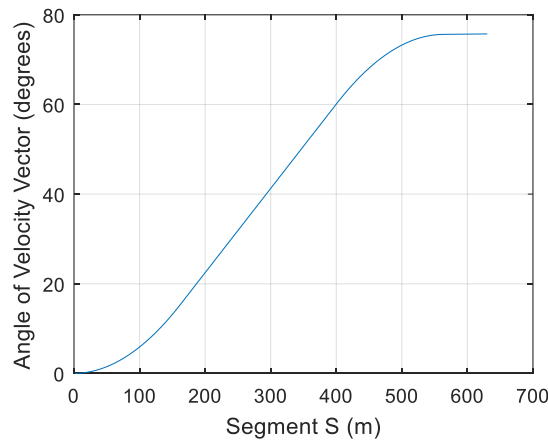


Figure 4.14 Finely-Discretized AASHTO Base Model: Orthogonal Phase Shift of Curvature Vector to Calculate Tangent Vectors.

4.3.2 Roadway Decomposition: Google Earth Images

Next, researchers evaluated the efficacy of the continuous curvature model using finely-discretized data collected from aerial photography of a real road segment with a design speed of 60 mph. The road segment is a part of Interstate 80 (I-80), which connects

Lincoln and Omaha in Nebraska, as shown in Figure 4.15. The points were picked as close as possible to resemble the road centerline of the highway. The road profile and resulting vectors from applying the discrete geometry approach are shown in Figure 4.16. It is noticeable that the fine discretization of the road points led to some inconsistencies between consecutive tangent vectors. The curvature magnitude with respect to length was also plotted in Figure 4.17, and it was observed that magnitude deviations also increased considerably compared to the AASHTO Green Book theoretical road design model. However, these inconsistencies are strongly related to very short segment lengths relative to curve radii. By using longer segment lengths or averages spanning multiple longitudinal points, results are considerably smoother.

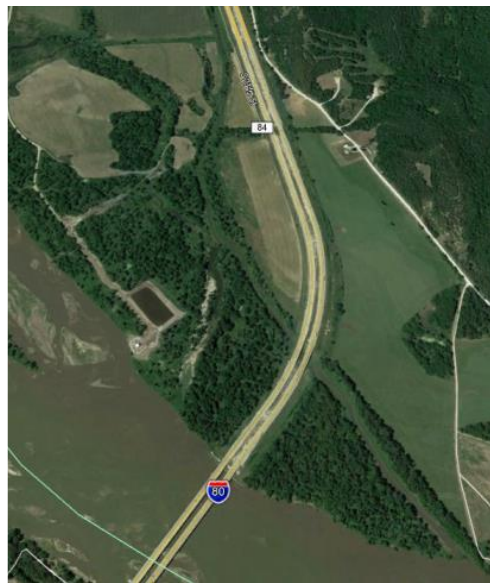


Figure 4.15 Google Earth: I-80 Road Example.

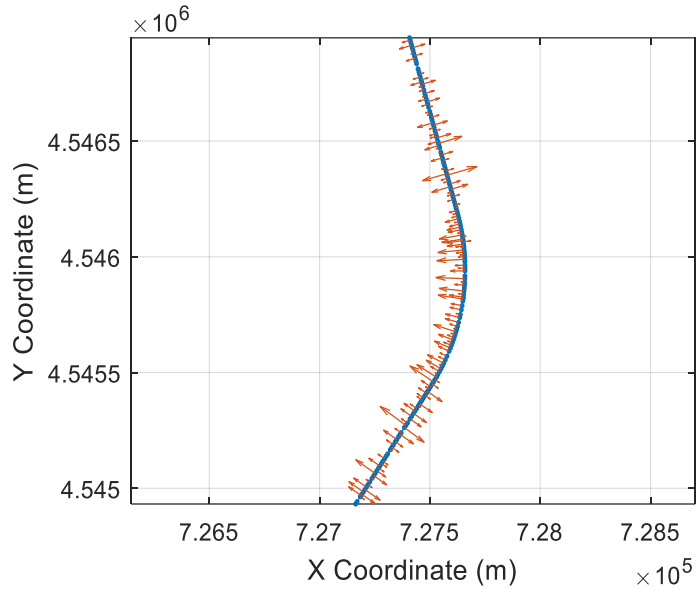


Figure 4.16 Google Earth Model: Road with Curvature Vectors.

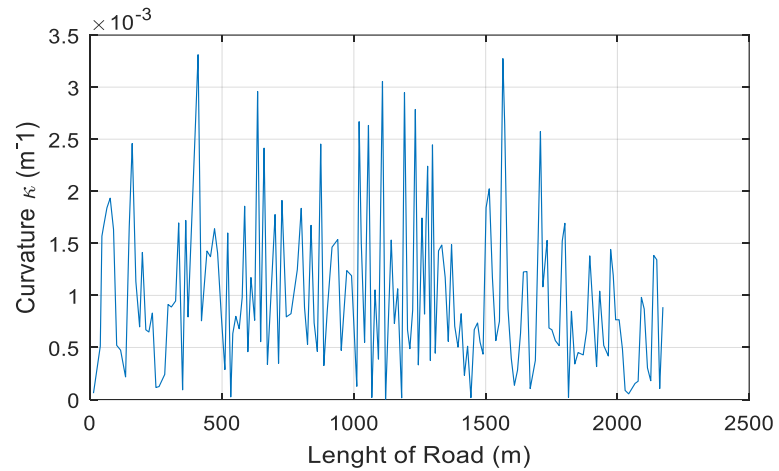


Figure 4.17 Google Earth Model: Curvature κ vs. Cumulative Curve Length.

Although curvature magnitudes varied significantly due to short segment lengths, the velocity vector angles were observed to be smooth overall along the segments, as shown in Figure 4.18.

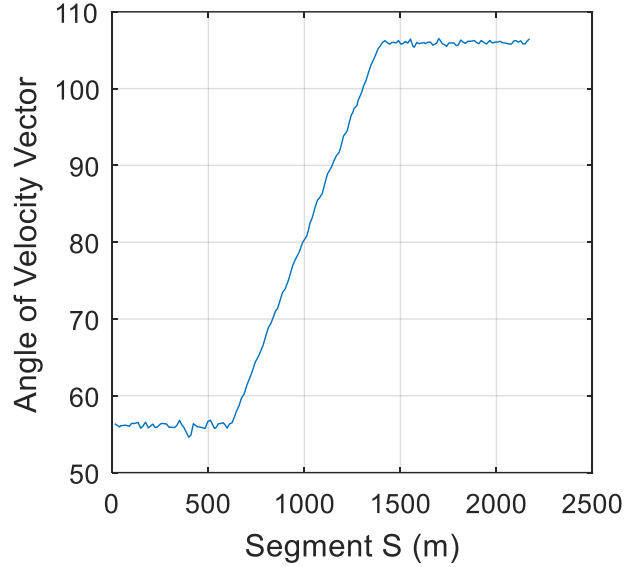


Figure 4.18 Google Earth Model: Orthogonal Phase Shift Approach.

Despite noise in the segmented curvature and heading angle discretization, the resulting plot of estimated lane centerline matched the road profile with excellent accuracy. An overplot of the calculated road profile based on the MDC method is shown in Figure 4.19.

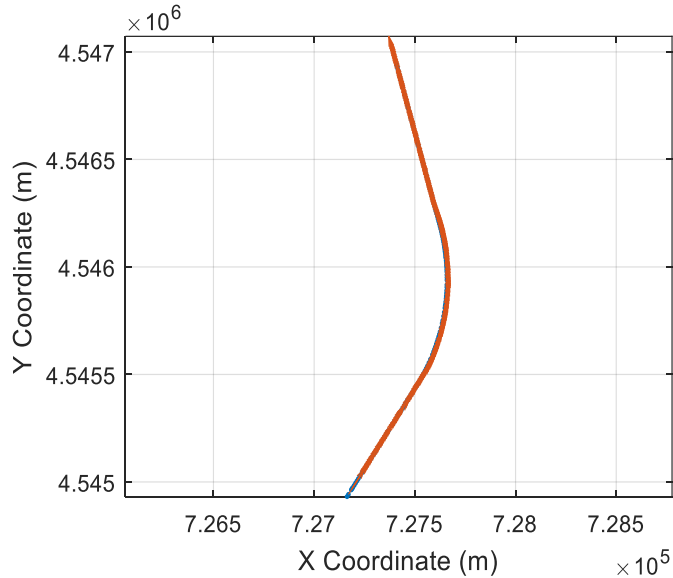


Figure 4.19 Google Earth Model: Road with Tangent Vectors.

4.3.3 Roadway Decomposition: GPS Model

The last evaluation of the value of the MDC method utilized GPS data collected while driving along a road with speed limit of 60 mph. The data was collected with a VC4000 Unit produced by Vericom Computers, Inc., at a frequency rate of 10 Hz. It should be noted that using single-trip GPS data with L1-rated accuracy provides a nominal error estimate of 1.981 m per data point [28], and therefore was the least accurate and smallest dataset evaluated. Nonetheless, applying the MDC method to identify the lane centerline coordinates demonstrated the power of this method in modeling road geometries, as shown in Figure 4.20, Figure 4.21, and Figure 4.22. It is expected that with larger datasets from multiple vehicle trips, highly precise lane centerline data may be identified even using GPS without differential accuracy estimates.

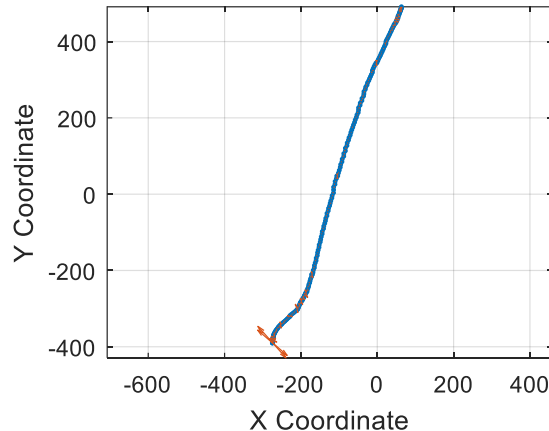


Figure 4.20 GPS Model: Road with Curvature Vectors.

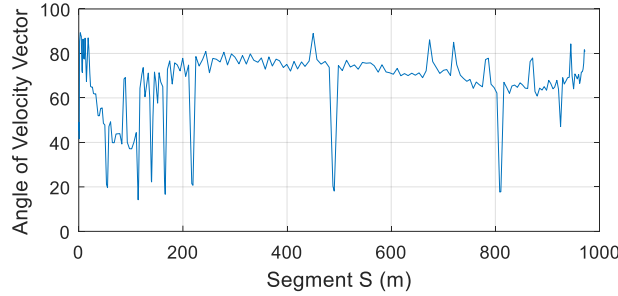


Figure 4.21 GPS Data: Tangent Vector Evaluation using Orthogonal Phase Shift Approach.

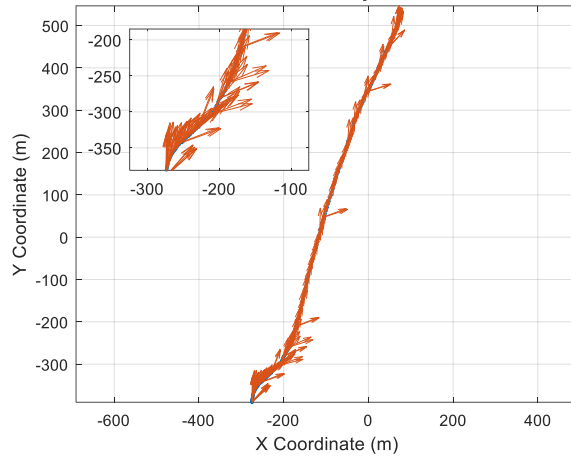


Figure 4.22 GPS Model: Road Construction with Tangent Vectors.

4.3.4 Smoothing Techniques

On trajectory generation, many techniques focus on interpolation restrict the motion of vehicles to maintain certain level of commodity and stability [29][30]. Given that the presented approach obtains heading angle based on discrete data sets for later storage, smoothing techniques may be required to sustain a better approximation of road centerlines while offering a different option to store road decompositions.

Many methods, such as Lagrange's interpolation and Linear Regressions, are used in fitting data for analysis [31]. However, for this application, a local regression with

weighted linear least squares was selected to maintain a minimum contribution of the data outliers. This avoids misrepresentation of data often provided by GPS sampling, shown in Figure 4.21 as peaks.

The data was given a span of 15% for outlier acceptance, and the resulting smoothed GPS data is shown in Figure 4.23, in which outliers are not part of the desired prescribed angle values. Smoothed data was plotted and compared to the original GPS model in Figure 4.24. It is noticeable how the data is easily smoothed from a GPS receiver. However, there is an initial swerving behavior on the heading data which could be due to initialization of the GPS.

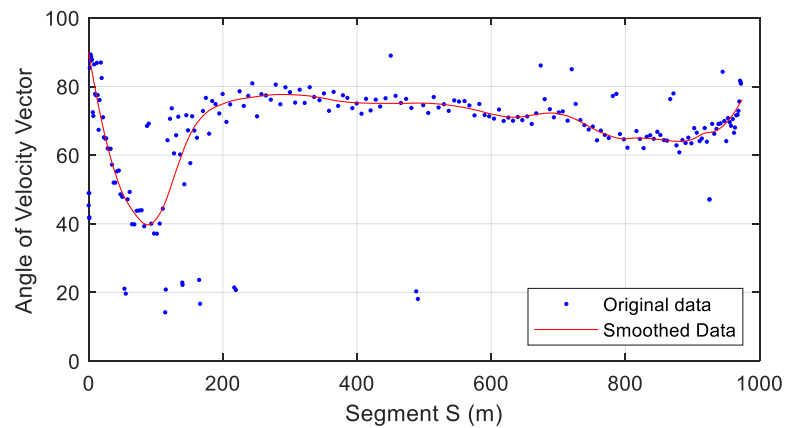


Figure 4.23 GPS Data: Smoothed Tangent Vector Data.

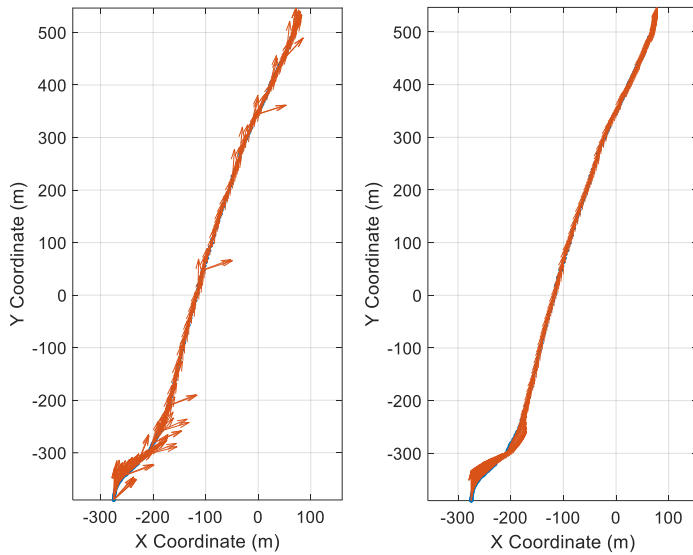


Figure 4.24 GPS Model: Original Data (Left) and Smoothed Data (Right).

4.3.5 Discussion

Road sampling data is critical to use the MDC method for identifying non-holonomic boundary constraints on target road paths. Aerial data and LIDAR or survey data are two methods discussed herein.

4.3.5.1 Aerial or Satellite Photography

Similar to Google Earth, this method requires identification (either manually or through software) of the lane. This method may be easily integrated into machine learning applications to preselect estimated road geometries without manual selection. The principal disadvantage from this method is susceptibility to error around unclear lane markings, such as adjacent to heavy tree foliage, road segments under construction, or roads affected by environmental effects. Furthermore, care must be taken to identify changes to the road network caused by road construction, including additional lanes or closed lanes.

4.3.5.2 Survey, LIDAR, or Photogrammetry Point Clouds

If road geometries are surveyed using conventional survey equipment or through LIDAR sampling, very high-precision lane geometries may be identified. Nonetheless, the process of point selection and the narrow spacing between consecutive lane edge points may introduce considerable numerical noise. This noise may be augmented by other vehicles or visual obstructions which interfere with clear lane edge identification.

4.4 Recommendations

The presented study has the potential to be implemented in a distributed model of vehicle automatization, but is not limited solely to passenger vehicles. Examples of other vehicle types which could utilize the target path formulation for positional error estimation and corrections include agricultural vehicles, transport vehicles (e.g., autonomous trucks), unmanned aerial systems, or mobile robots.

To achieve this goal, the following scheme is proposed for an implementation of the discrete road decomposition, as shown Figure 4.25. The first step involves collection of road data through any convenient means: GPS data, surveying, or aerial scanning. This road data contains a representation of the road centerlines which can be exported in different formats. These road centerlines are decomposed with the proposed method, stored in a road target path matrix, and transmitted wirelessly to a vehicle in motion. The infrastructure may also assist with precise vehicle localization to improve error estimation, allowing the vehicle onboard systems to have excellent real-time observation of potential deviations from the target path. Finally, a controller is developed to consider the heading based on the discrete road decomposition and navigate safely through the road.

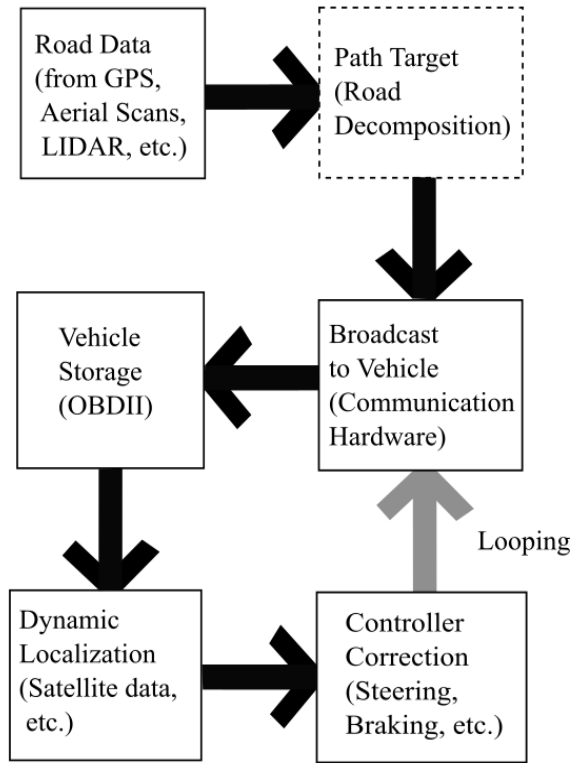


Figure 4.25 Implementation Scheme for Road Curvature Decomposition.

Because the system does not rely on local ad hoc determination of lane boundaries and does not utilize machine vision or de facto external tracking systems, the system is well-positioned to provide guidance system for autonomous vehicles even in adverse weather conditions, poor visibility, and even for temporary road or lane closures. The dynamic road network relay to autonomous vehicles may allow for alternative route selection in the event of congestion or crash events, and external guidance information such as tire-pavement friction reductions reported by other vehicles or estimated from weather reports may also be broadcast to the vehicle in targeted geospatial areas. As such, this technique for vehicle guidance systems could be complimentary to existing lane keeping and ADAS systems for crash avoidance or mitigation.

Research is ongoing at the University of Nebraska-Lincoln to confirm the accuracy of this technique and the applicability to autonomous vehicle guidance systems. More research including empirical testing and simulation are recommended to integrate the MDC method into a broader vehicle guidance paradigm.

4.5 Summary/Conclusions

In conclusion, a method was proposed to calculate trajectories based on discrete curvature and road tangent calculations. The proposed method is consistent with AASHTO design guidelines and can be made to be compatible with vehicle performance limits by controlling allowable speed based on geospatial road curvature. Additional research was recommended to consider smoothing techniques for onboard driving and should be verified using empirical testing and computer simulation. Successful implementation of this method could offer a new key piece to solve the autonomous vehicle paradigm under weather disruptions and/or other navigation technologies.

4.6 References

- [1] Stolle, C., Jacome, R., and Sweigard, M., “Autonomous Technology, A Review - MATC Year One Report,” Internal Report, 2018.
- [2] Huetter, J. “IIHS: HLDI Estimates 24% of Fleet Had Backup Cameras, 17% Had Parking Sensors in 2016.” Repairer Driven News (blog), February 2, 2018.
<https://www.repairerdrivennews.com/2018/02/02/iihs-hldi-estimates-24-of-fleet-had-backup-cameras-17-had-parking-sensors-in-2016/>.
- [3] HLDI Bulletin, “Compendium of HLDI collision avoidance research,” vol. 35, No. 34: September 2018.

- [4] Benson, A.J., Tefft, B.C., Svancara, A.M., and Horrey, W.J. (2018). Potential Reductions in Crashes, Injuries, and Deaths from Large-Scale Deployment of Advanced Driver Assistance Systems (Research Brief). Washington, D.C.: AAA Foundation for Traffic Safety.
- [5] LaValle, S.M. “Planning Algorithms,” 2006. <https://doi.org/10.1017/cbo9780511546877>.
- [6] Heinrich, S., “Planning Universal On-Road Driving Strategies for Automated Vehicles,” AutoUni – Schriftenreihe. Springer, 2018. <https://doi.org/10.1007/978-3-658-21954-3>.
- [7] Kelly, A., and Nagy, B., “Reactive Nonholonomic Trajectory Generation via Parametric Optimal Control.” *I. J. Robotics Res.* 22 (2003): 583–602. <https://doi.org/10.1177/02783649030227008>.
- [8] Dubins, L.E., “On Curves of Minimal Length with a Constraint on Average Curvature, and with Prescribed Initial and Terminal Positions and Tangents,” *American Journal of Mathematics* 79, no. 3 (1957): 497–516. <https://doi.org/10.2307/2372560>.
- [9] Ziegler, J., Bender, P., Dang, T., and Stiller, C., “Trajectory Planning for Bertha — A Local, Continuous Method.” In 2014 IEEE Intelligent Vehicles Symposium Proceedings, 450–57, 2014. <https://doi.org/10.1109/IVS.2014.6856581>.
- [10] Fox, C., “An Introduction to the Calculus of Variations. Courier Corporation,” 1987.
- [11] Takahashi, A., Hongo, T., Ninomiya, Y., and Sugimoto, G., “Local Path Planning And Motion Control For AGV In Positioning.” In Proceedings. IEEE/RSJ

- International Workshop on Intelligent Robots and Systems'. (IROS '89) The Autonomous Mobile Robots and Its Applications, 392–97, 1989.
<https://doi.org/10.1109/IROS.1989.637936>.
- [12] Piazzì, A., and Guarino Lo Bianco, C. “Quintic G₂-Splines for Trajectory Planning of Autonomous Vehicles.” In Proceedings of the IEEE Intelligent Vehicles Symposium 2000 (Cat. No.00TH8511), 198–203, 2000.
- [13] Sun, Y., Zhan, Z., Fang, Y., Zheng, L. et al., “A Dynamic Local Trajectory Planning and Tracking Method for UGV Based on Optimal Algorithm,” 2019-01-0871, 2019. <https://doi.org/10.4271/2019-01-0871>.
- [14] Wilde, D., “Computing Clothoid-Arc Segments for Trajectory Generation,” In 2009 IEEE/RSJ International Conference on Intelligent Robots and Systems, 2440–45, 2009. <https://doi.org/10.1109/IROS.2009.5354700>.
- [15] Delingette, H., Hebert, M., and Ikeuchi, K. “Trajectory Generation with Curvature Constraint Based on Energy Minimization.” In Proceedings IROS '91:IEEE/RSJ International Workshop on Intelligent Robots and Systems '91, 206–11 vol.1, 1991.
<https://doi.org/10.1109/IROS.1991.174451>.
- [16] Werling, M., Ziegler, J., Soren, K., and Thrun, S., “Optimal Trajectory Generation for Dynamic Street Scenarios in a Frenet Frame,” In 2010 IEEE International Conference on Robotics and Automation, 987–93. Anchorage, AK: IEEE, 2010.
<https://doi.org/10.1109/ROBOT.2010.5509799>.
- [17] Werling, M., Kammel, S., Ziegler, J., and Groll, L., “Optimal Trajectories for Time-Critical Street Scenarios Using Discretized Terminal Manifolds.” The International

- Journal of Robotics Research 31, no. 3 (March 2012): 346–59.
<https://doi.org/10.1177/0278364911423042>.
- [18] Sun, Y., Zhan, Z., Fang, Y., Zheng, L. et al., “A Dynamic Local Trajectory Planning and Tracking Method for UGV Based on Optimal Algorithm,” 2019-01-0871, 2019. <https://doi.org/10.4271/2019-01-0871>.
 - [19] Gillespie, T.D. “Fundamentals of Vehicle Dynamics,” SAE Int. ISBN 1-56091-199-9, 1992.
 - [20] Pacejka, H.B. Tyre and Vehicle Dynamics. Butterworth-Heinemann, 2006.
 - [21] do Carmo, M.P. Differential Geometry of Curves and Surfaces. 1st ed. Englewood Cliffs, N.J: Prentice-Hall, 1976.
 - [22] Pressley, A.N. Elementary Differential Geometry. 2nd ed. Springer Undergraduate Mathematics Series. London: Springer-Verlag, 2010. <https://doi.org/10.1007/978-1-84882-891-9>.
 - [23] O'Reilly, O.M. Engineering Dynamics: A Primer. Springer Science & Business Media, 2010.
 - [24] A Policy on Geometric Design of Highways and Streets, (The Green Book) 6th ed. American Association of State Highway and Transportation Officials, 2011.
 - [25] Morral, J.F., and Talarico, R.J., “Side Friction Demanded and Margin of Safety on Horizontal Curves,” Journal of the Transportation Research Board, 1994, pp. 145-152.
 - [26] Henry, J.J. “Evaluation of Pavement Friction Characteristics, a Synthesis of Highway Practice.” 2000, NCHRP Synthesis 291, 7p.

- [27] Are Mjaavatten (2019). Curvature of a 2D or 3D curve (<https://www.mathworks.com/matlabcentral/fileexchange/69452-curvature-of-a-2d-or-3d-curve>), MATLAB Central File Exchange. Retrieved May 24, 2019.
- [28] William J. Hughes Technical Center, “Global Positioning System (GPS) Standard Positioning Service (SPS) Performance Analysis Report,” Federal Aviation Administration, 2017.
- [29] Levien, R.L., “From Spiral to Spline: Optimal Techniques in Interactive Curve Design,” n.d., 191.
- [30] Akima, H. “A New Method of Interpolation and Smooth Curve Fitting based on Local Procedures,” J. ACM 17, no. 4 (October 1970): 589–602. <https://doi.org/10.1145/321607.321609>.
- [31] Heath, M.T. Scientific Computing: An Introductory Survey, Revised Second Edition. SIAM, 2018.

CHAPTER 5. A DYNAMICALLY-CONCISE ROADMAP FRAMEWORK FOR GUIDING CONNECTED AND AUTOMATED VEHICLES

Ricardo O. Jacome*, Cody Stolle *, Ronald K. Faller *, and George Grispos[^]

* Midwest Roadside Safety Facility with The University of Nebraska – Lincoln, Department of Mechanical
Engineering, Lincoln, Nebraska, USA

^School of Interdisciplinary Informatics with University of Nebraska-Omaha, Omaha, Nebraska, USA

Abstract

A new map framework is proposed to improve the guidance and trajectory prediction capabilities of connected and automated vehicles (CAVs), even in challenging conditions of low visibility and adverse environmental effects. Based on the fusion of vehicle dynamics and road design standards, the map framework provides a consolidated collection of critical reference points of roadways, such as centerlines and information about the shape of the roadway in the vicinity of a vehicle, including curvature and road alignment angle. Roads are discretized using reference points, and simple parameters are used to connect adjacent segments representing the road shape. Additional data can be appended to the map, including elevation and roadside slope data, variable speed limits, and lane controls.

Index Terms—Connected and Automated Vehicles, Curvature, Framework, Vehicle Dynamics, Street Design

5.1 Introduction

Full vehicle autonomy is one of the most coveted achievements in contemporary transportation research. These “intelligent” vehicles fall under a broad class of Connected and Automated Vehicles (CAVs) with an ultimate goal of providing destination travel without any driver input other than starting and final locations. Ongoing efforts provide incremental improvements on safety and functionality until full autonomy is achieved. According to National Highway Traffic Safety Administration (NHTSA), on-vehicle Advanced Driver Assistance Systems (ADAS) contributed to reductions in annual crashes and prevention of serious injuries since their introduction in production vehicles [1], and existing technologies are often utilized in newer systems to further expand their benefits. For example, anti-lock brake systems (ABS) improved vehicle control by increasing the average tire-pavement friction coefficient during braking [2]. ABS systems became a significant component contributing to Electronic Stability Control, which resists out-of-control vehicle trajectories and the associated risk of rollovers [3], as well as lane departure warning and automated crash prediction and mitigation (pre-crash braking) systems [4][5].

Evolving from ADAS, CAVs added communications with the environment as part of an Internet-of-Things (IoT) approach. CAVs aim to be the state-of-the-art technology for the foreseeable future and could lead to a renaissance of transportation-related opportunities: Transportation-as-a-Service (TaaS), automated shipping; convenient carpooling or ride-shares; and automated tour industry. The United States Department of Transportation (DOT) has developed programs to promote traffic optimization with CAVs, with partnering agencies including NYCDOT, THEA, VDOT, the Connected Vehicle

Pooled Fund, and WYDOT [6]. For example, the THEA project relies on providing CAVs with information such as Wrong Way Entries, or End of Ramp Deceleration Warnings [7]. This pilot system is currently restricted to urban areas and exclusively provides in-vehicle driver warnings. For highway projects, WYDOT utilizes Roadside Units (RSUs) to provide properly-equipped CAVs with information about the current weather (i.e. snow weather warnings), for primarily cargo vehicles and trucks [8][9].

Several approaches have resolved very difficult vehicle navigation challenges, including automated parking assistance [10][11] and lane navigation during passing maneuvers [12]. Multiple urban-navigation efforts have culminated in solutions; the Defense Advanced Research Projects Agency (DARPA) Grand Challenge for automated driving in 2004, 2006, and 2007 led to many of the principal concepts for automated vehicle guidance frameworks, some of which are still utilized today. For example, “Boss”, the Chevrolet Tahoe vehicle which ultimately won the DARPA challenge, utilized fundamental vehicle dynamics principles, extracted lane curvature from optical measurements, estimated occupied space from moving and stationary objects, and adjusted the trajectory to follow routes in real time up to 48 km/h [13]. Numerous studies have been conducted evaluating improvements to similar computer vision-based feature navigation, most recently equipped with dynamic artificial intelligence and deep learning [12][14][15]. However, using the attributes and criteria described by the Society of Automotive Engineers (SAE) J3016 “Levels of Driving Automation” [16], few vehicles have been able to accomplish a fully “Level 4” automation [17]. Some are publicly questioning if it is still impractical with current technological limitations to achieve full vehicle autonomy [18]. If

such a vehicle were to be developed, it may require a different operational framework than has currently been implemented.

Researchers at the University of Nebraska Lincoln (UNL) have proposed a new framework for CAV guidance based on a mathematically-compact and dynamically-consistent map formulation as an enhancement for existing road map and localization approaches. The proposed map formulation integrates preferred travel corridors, reference vector definitions for curvature and heading, and updatable fields including elevation, variable speed limit, and options for additional expansion fields. The map framework is intended to improve navigation information with remote management of some road parameters from DOT control locations and to complement existing technologies for a more robust vehicle guidance solution. The purpose of this paper is to review existing map frameworks and develop the foundations of the new proposed map framework.

5.2 Review of Transportation Guidance Frameworks

5.2.1 Machine-Driven Guidance Systems

Most existing ADAS guidance frameworks follow a data-processing scheme similar to Figure 1 [19]. These strategies are a combination of five multi-layered sections, which for the purposes of this paper, will be assumed to occur in a sequential order: (1) Sensors receive data from the environment (e.g., image recognition, positional data) [15][20]; (2) State estimation identifies the location of the vehicle (and its parameters) in reference to the data obtained from sensors [21][22]; (3) Local planning identifies the geometrical and dynamic constraints on all possible vehicle actions (denoted in this paper as workable space, i.e., street) [23][24][25]; (4) Trajectory Generation predicts trajectory

paths of the vehicle (e.g., clothoid paths, polynomials) based on vehicle controls and physics constraints (e.g., kinodynamic constraints). The name comes from determining which trajectories (inside of the workable space) are possible for the vehicle to perform, based on its current state [26][27]; (5) Controllers implement vehicle controls using data from the Trajectory Generation phase (e.g., throttling, braking, steering, or disengaging the automatic mode), which are decided by different control theory approaches that depend on the previously-established trajectories [28][29][30].

Each strategy has its own research field [31], but further exploration of the development of each component of the framework is beyond the scope of this paper. Examples of the different combinations available for the main five steps that are performed during autonomous driving are shown in Figure 5.1.

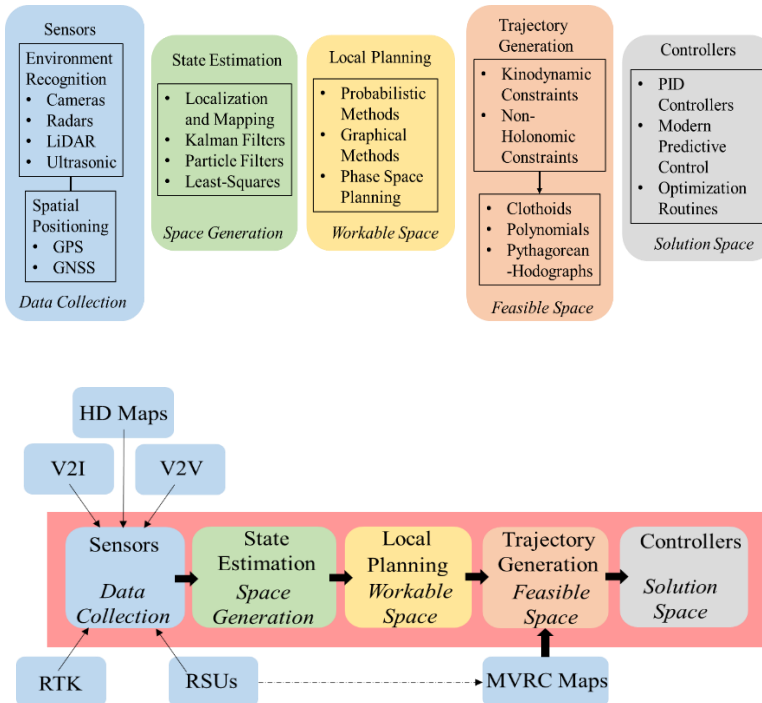


Figure 5.1 Sample of Current CAV Guidance Framework

While these intelligent vehicle systems continue to improve in quality, no ADAS guidance systems have yet demonstrated the capability to perform according to SAE's "Level 4" autonomy; further, industry experts have predicted that a level 5 autonomy solution are still on a horizon beyond current capabilities [16][32]. In part, the difficulty of advancing to higher autonomy is that current solutions have shown a generally high reliability in only the most favorable conditions: adequate light; clear contrast for lane edge markings; good road maintenance with clear markings on pavement; and no visual obfuscations (precipitation, blowing smoke, dust, fog, or snow). Efforts to improve the existing automated guidance technologies are under evaluation; glass beads added to reflective pavement paint improve optical identification during precipitation and improve lidar reflectivity [33], and wider paint markings or adjusted markings, such as parallel marks, improve optical contrast and lane keeping systems [34]. Object recognition systems using artificial intelligence for feature identification rely on common sign geometries for both positioning and determining critical information [35][36][37][38][39]. However, even minor defects on signs have disrupted feature recognition algorithms [40][41].

Current CAVs adopted a new framework for data collection in which information from external sources establish communication channels for enhancement of previously-established ADAS technology. Multiple external sources are currently available for CAVs, including Vehicle-to-Infrastructure (V2I) communication, Vehicle-to-Vehicle (V2V) communication, Real-Time Kinematics (RTK) used with Global Navigation Satellite System (GNSS), RSUs, and high-definition (HD) maps, as shown in the bottom of Figure 5.1 [42][43][44][45][46]. These sources aim to augment the data collection capabilities of

CAVs, simultaneously increasing their hierachal data processing. Simpler methods from RSUs can provide simple warning messages for the driver (e.g., weather alerts), whereas high-density operations aim to supply high-quality locations and identification data for processing (e.g. three-dimensional LiDAR imagining).

5.2.2 Attributes for an All-Purpose Navigation System

Considering the extensive developments conducted to date on CAVs and intelligent transportation systems, researchers identified attributes that were consistent with a successful transportation system for all-purpose implementation:

- Geographically unconstrained, system should accommodate navigation for all locations on earth
- Operational in range of common, realistic operating conditions:
 - Environmental: ice, snow, rain, cold, heat, dust, wind, hot and cold temperatures
 - Network: high radio frequency noise, low radio, satellite, or cellular connectivity
 - Road: paved, gravel, mud, dirt, wet, snow-covered, leaf-covered
 - Light: twilight, sunrise, daylight, sunset, dusk, darkness
- Updatable:
 - Closures of a lane or roadway as a result of feature loss (bridge collapse), emergency medical services, fire, or police activity
 - Lane geometry or speed adjustments in conjunction with work zones, detours, diversions, emergency evacuations, variable speed limit

- adjustments (e.g., icy or fog conditions), and school zones or political activities (e.g., presidential motorcade)
 - Road expansions, new construction, terrestrial shifts over time
- Accommodations to growth including new features or parameters

Human drivers and mobile vehicles are highly adaptable; drivers are generally able to handle many types of terrain and even navigate areas not explicitly defined as roadways (e.g., off-road or snow-covered roads with no obvious lane markers). Hundreds of millions of people will navigate slick, icy, and snow-covered roads each year. Drivers pass through work zones by navigating around traffic cones and barricades, and obeying traffic signs, and may adjust travel paths based on public service notifications of planned construction or road closures. Likewise, school zones frequently utilize reduced speed limits to promote safety for high pedestrian traffic, which are typically denoted with flashing lights, providing a form of variable speed limit enforcement. Roundabouts, vulnerable road user facilities, bike lanes, flashing turn signals, and changes to highway systems have been implemented to existing roads and intersections, and drivers adapted to these systems. Therefore, successful, complete, automated guidance frameworks should accommodate every one of these common travel conditions and adjust to future changes in transportation.

In the authors' observation, all existing and proposed guidance frameworks are derived from a need to adapt to an existing transportation framework. As such, guidance frameworks are limited to identifying the road geometries, connections, and directions, mapping an optimized local trajectory (tens of meters in front of the vehicle), modifying the vehicle trajectory to adapt to other vehicles, interruptions, or obstructions, and

executing stable maneuvers. As CAVs continue to evolve and adapt, and particularly as new and novel transportation vehicles become available for use, it may be necessary to reimagine the guidance framework operation to implement desirable features and accommodate future growth.

5.3 Introduction to the MVRC Map Framework

To address the attributes from the previous section, a new paradigm is proposed, which utilizes critical vehicle dynamics properties to construct high-fidelity reference data. Authors of this research study deemed this map the Midwest Virtual Road Corridor, or MVRC. Its operating framework is intended to provide a low-memory yet mathematically consistent road representation that can be utilized by all current and proposed guidance methods. Thus, regardless of what navigational method and vehicle control scheme is utilized, consistent map data is available for defining the physical space that a CAV is intended to occupy. Moreover, when combined with vehicle-to-infrastructure communication, a new localization system and thus new guidance framework could be developed based on the data provided by the MVRC map.

The underlying principle of the MVRC map is to provide data, which is directly usable in the trajectory generation and local planning modules for CAVs, while providing a reference on dynamic-trajectory navigation which is independent of vehicle on-board sensors. Thus, the MVRC provides a more robust redundancy layer of data for aiding navigation. This bypass of information is demonstrated in Figure 5.2, where external MVRC data (in this example, coming from RSUs) is inputted as part of the trajectory generation rather than following the typical information flow. With this bypass and after

establishing a proper geospatial location, the vehicle has a dynamic reference on how to navigate the road without requiring image processing. This MVRC reference data can be compared with on-board CAV computed trajectories to increase travel safety.

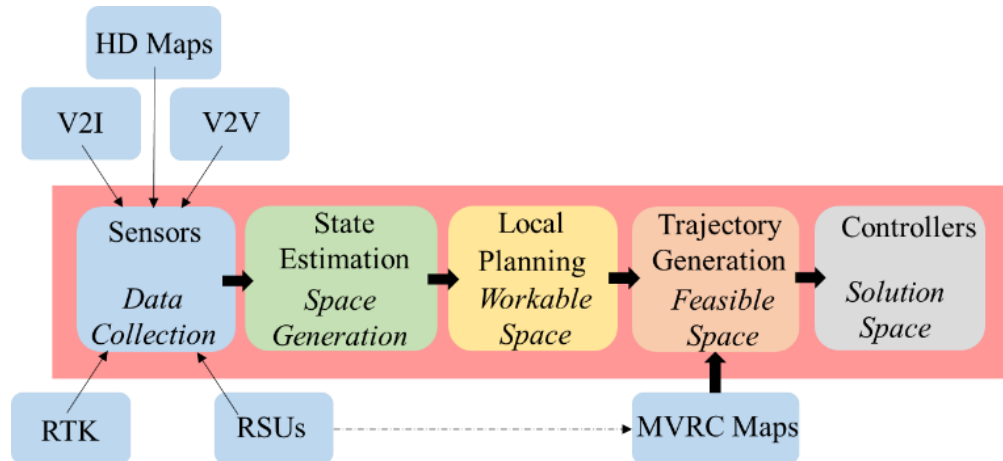


Figure 5.2 Proposed MVRC Framework for CAV Guidance

The MVRC, in technical terms, consists of segmented roadways using high-precision GNSS reference points and consecutive connection anchor points. These points are prescribed with dynamic-attributes, such as curvature, turn direction, lateral angle change per segment, cardinal travel direction, lane width, lane elevation, and lane-specific speed limit data. The numerical values for these data points are derived from the link between vehicle dynamics and road design standards, as described next.

5.3.1 Relationship Between Road Design and Vehicle Dynamics

The principles of vehicle dynamics are well defined in literature: for conciseness, only elements critical to the application of the MVRC are discussed herein. For more

complete discussions of vehicle dynamics, including evaluations of critical stability, readers are encouraged to review additional references [47][48].

In the United States, the prevailing standards for road design come from the American Association of State Highway and Transportation Officials (AASHTO), referred as the Green Book [49]. Road geometries, including lane geometries, are established using design speeds and number of lanes, curvature, and road “banking” (superelevation). Most roads designed to AASHTO specifications assume that the vehicle can successfully navigate, accelerate (including braking), and turn during wet or rainy conditions. The Green Book based its calculations for tire-pavement friction on empirical studies for “friction demand”, the average amount of friction used by drivers when navigating curves [49]. Friction demand is derived from vehicle kinematics and dynamics (speed, acceleration, and turn radii), whereas friction supply between the tires and pavement varies based on inclement weather, road maintenance or smoothness, tire wear and quality, and incidentals (e.g., presence of gravel, sand).

Initially, a simple scenario is considered in which the vehicle is assumed to remain upright and oriented in a typical driving configuration, and vertical changes in the vehicle’s center of gravity (c.g.) that are caused by the road are not considered. Under normal operating conditions, the vehicle remains far below critical stability and non-linearity thresholds; thus, the vehicle may be reasonably represented using a point mass representation, located at the vehicle’s c.g. According to Newton’s second law, the total force acting on the vehicle is the vector sum of all wheel forces, which are the only vehicle components interacting with the ground. An image of the sum of forces acting on the

vehicle is shown in Figure 5.3. Road design parameters include road friction, superelevation, and maximum width, while the vehicle parameters are velocity, acceleration, track width, and vehicle length. The resulting curve and superelevation relationship for road design is shown below, using small angle assumption for ϕ [49]:

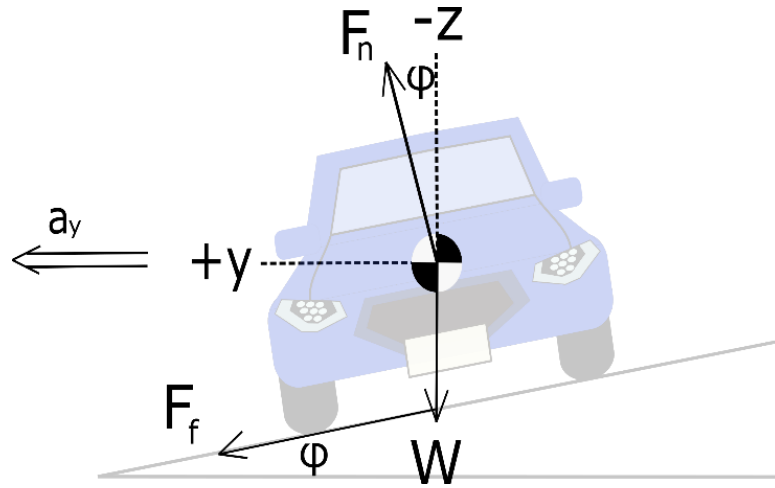


Figure 5.3 Vehicle Dynamics on a Superelevated Curve

$$\frac{v^2}{g\rho} = \frac{\mu \cos(\phi) + \sin(\phi)}{\cos(\phi) - \mu \sin(\phi)} \approx \frac{\mu + 0.01e}{1 - 0.01\mu e} \quad (5.1)$$

v = Vehicle velocity (m/s)

g = Gravitational acceleration (9.81 m/s²)

ρ = Radius of curvature (m)

μ = Coefficient of side road friction

ϕ = Superelevation angle (deg)

e = Superelevation: $e = 100\% * \sin(\phi) \approx 100\% * \tan(\phi)$

In road design, both horizontal and vertical curves are considered. Horizontal curves focus on a top view of street (latitude and longitude), while vertical curves focus on

a profile view of the street (altitude) [49][50]. When the road topology utilizes simultaneous horizontal and vertical curves, the limits on maximum allowable radii in both directions are affected. Horizontal curves are divided into 4 main categories shown in Figure 5.4, where the main difference lies in the radius of curvatures per segment of road. For this discussion, only two-dimensional horizontal curves are shown.

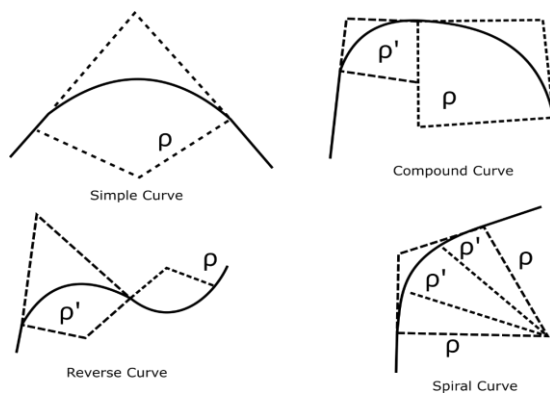


Figure 5.4 Example Horizontal Curves

Where two road segments of different curvatures come together, a transition is usually designed, which allows vehicles to smoothly transition between curves. Curve transitions are typically designed according to AASHTO procedures, which utilize a clothoid or spiral construction [49]:

$$L = \frac{0.0214V^3}{\rho C} \quad (5.2)$$

where:

L = Minimum length of a transition (m)

V = Vehicle speed (km/h)

ρ = Radius of curvature (m)

$$C = \text{Rate of increase of lateral acceleration } \left(\frac{m}{s^3} \right)$$

The trajectory and dynamics of a moving vehicle utilize concepts from particle dynamics and are often described using a Serret-Frenet (or “Normal-Tangential”) coordinate system [51]. This coordinate system definition is shown in Figure 5.5, in which the principal longitudinal axis of the vehicle is parallel with the vector of rigid body velocity in what is referred to as a “tracking” orientation.

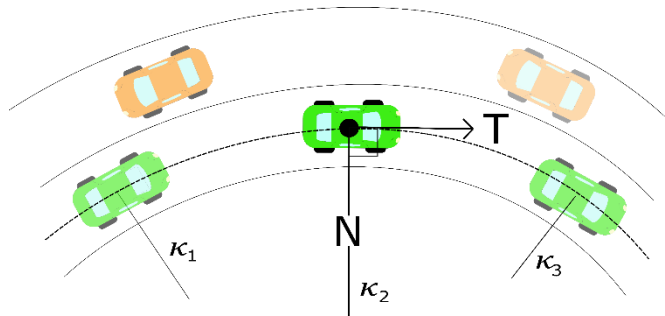


Figure 5.5 Serret-Frenet Coordinate System Definition and Vehicle Alignment

The acceleration of the vehicle is defined by the time derivative of the velocity vector, which may have components in both the longitudinal direction (speeding up or slowing down) and lateral direction (centripetal acceleration). Noting that the curvature κ is defined as the inverse of the radius of curvature ρ per instantaneous road segment, the acceleration vector in Serret-Frenet coordinates can be simplified to:

$$\mathbf{a} = \dot{v} \mathbf{T} + \kappa v^2 \mathbf{N} \quad (5.3)$$

where:

a = Acceleration vector vehicle (m/s^2)

v = Vehicle speed (m/s)

κ = Curvature of vehicle path at an instantaneous point (m^{-1})

N = Normal unit vector

T = Tangential unit vector

Curvature is an advantageous parameter, because it is infinitely differentiable, whereas the radius of curvature is undefined (singularity) as a line becomes tangent. For the MVRC formulation, an adjusted SAE convention is adapted for a 2-dimensional planar problems where the vertical axis of the vehicle (SAE “Z” direction) is collinear with the binormal vector of the Serret-Frenet frame [52], implying that SAE (x,y,z) convention matches (T,N,B), as noted in Figure 5.6.

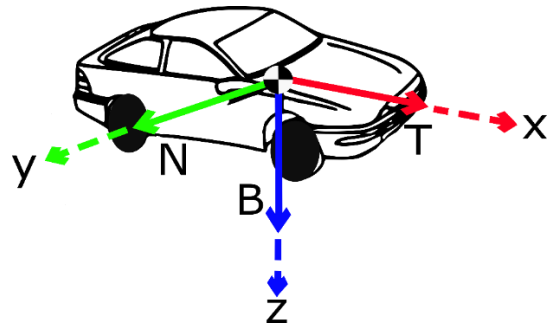


Figure 5.6 Serret-Frenet Frame Imposed on SAE Orientation Convention.

Although curvature is scalar in the Serret-Frenet equations, researchers redefined the product of the curvature and normal vectors as the curvature vector. The resulting mathematical relationships are:

$$K := \kappa N \quad (5.4)$$

$$a = \dot{v} T + v^2 K \quad (5.5)$$

$$N := \frac{K}{\kappa} y \quad (5.6)$$

where:

K = Curvature vector (m^{-1})

y = SAE pitch axis

The scalar representation of κ is therefore positive if the vehicle is performing a right-hand turn, and negative if the vehicle is performing a left-hand turn. For tangent road segments, the horizontal curvature is defined as zero.

5.3.2 Construction of MVRC Map

For most operating conditions, vehicle dynamics is based on particle dynamics relationships. All major lane-keeping or automated guidance systems rely on the curvature estimation to perform longitudinal and lateral vehicle control [29][30][53]. However, this data is rarely, if ever, provided in self-contained maps; therefore, it is either generated locally ad hoc or estimated using a sequence of GNSS waypoints. Hence, curvature was deemed an essential parameter to include in a high-fidelity map. Researchers generated methods of calculating the curvature based on positional data and augmenting position and curvature map data with additional informative reference data.

It was noted that curvature in road design standards, as shown in equations (5.1) and (5.2), can be used to formulate dynamic trajectories using equation (5.3). Geometrically, curvature can be defined as a property of curves that measures the amount

of deviation from a straight line [54][55]. Numerically, this is expressed as the change of the angle made by the tangent of a curve with respect to segment length:

$$\kappa = \frac{d\theta}{ds}$$

which by integration implies the following is true:

$$\theta = \int_0^s \kappa(s) ds + \theta_0$$

In trajectory generation, the well-known parametric representation of a curve $\alpha(s) = (x(s), y(s))$ is used to represent vehicle trajectories in a local two-dimensional Cartesian map, such that:

$$x(s) = x_0 + \int_0^s \cos \left(\int_0^s \kappa(s) ds + \theta_0 \right) ds \quad (5.7)$$

$$y(s) = y_0 + \int_0^s \sin \left(\int_0^s \kappa(s) ds + \theta_0 \right) ds \quad (5.8)$$

Equations (5.7) and (5.8) when describing a trajectory are sometimes denoted as clothoids, Cornu spirals or Euler spirals. These are fundamental in both trajectory generation and street design. However, the difficulty of analytically defining these equations for on-board calculations has led to numerical approximations that can be used with spline interpolation or its alternatives [56]. Although these methods are reasonably accurate, current available data is not sufficient to provide guidance information for a vehicle under all driving conditions when dependent on vehicle on-board sensors only [57].

In this paper, the preferred corridor is assumed to be the centerline of a lane. Several methods for identifying lane boundary lines are applicable, such as utilizing satellite and

aerial photography with “ground truth” corrections, using survey data, or collecting traces of vehicle routes in individual lanes [58]. The convergence of the vehicle SAE coordinate frame with a modified Serret-Frenet frame means that a vehicle’s trajectory curvature, and by extension road centerline curvature, is orthogonal to the desired vector of velocity (tangent to the lane centerline) at any reference position. Therefore, the lane centerline is the geometric center between lane boundaries lines along isocurvature lines (lines of constant curvature, orthogonal to the lane). In other words, adjacent lanes form a family of lane boundary lines consistent with Bertrand Curves [55].

To simplify curvature estimation, spatial coordinate transformations are used to convert spherical data to a localized 2D overhead map in the vicinity of each discrete reference point [59][60]. Discrete reference points on the lane centerlines are converted to (X,Y) pairs. Three consecutive reference points are collected as a data triad, and the approximate curvature at the center of a data triad is estimated using the MDC procedure [61]. This process can be completed per road segment or per lane. Visually, this is denoted in Figure 5.7 where a dynamic trajectory is mapped into the static road data for vehicle reference.

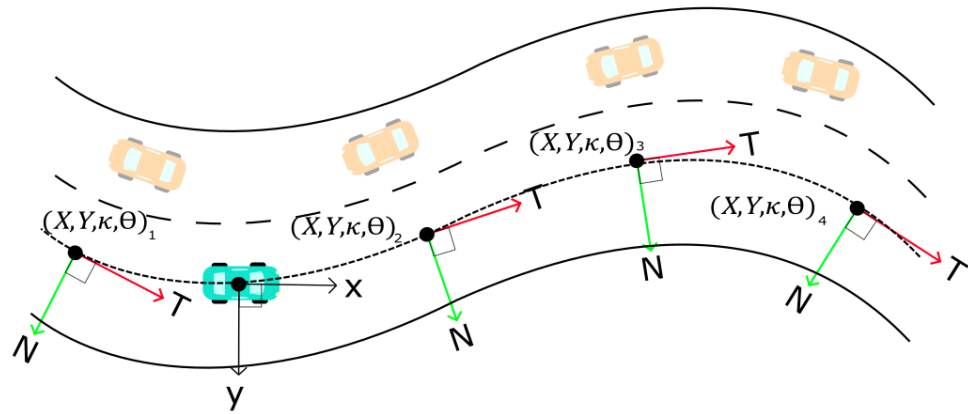


Figure 5.7 MVRC Reference Data on Static Sample Map.

Even though not shown in the previous picture, outcomes of the MVRC are stored in an adjustable matrix for any $i \in [1, n]$ where n denotes the number of data points for a given road:

$$ID_i = [Px_i, Py_i, s_i, \kappa_i, \theta_i] \quad (5.9)$$

where:

ID_i = Road segment identification

Px_i = Latitudinal position

Py_i = Longitudinal position

s_i = Segment length (m)

κ_i = Curvature at segment length (m^{-1})

θ_i = Road tangent angle (degrees)

5.3.3 Example Construction of MVRC Map

As a practical example, a simple curve on a road highway in Lincoln, Nebraska (USA) from Google Earth is shown on the top of Figure 5.8. The map UTM coordinates

are transformed, and the discrete curvature of the road was found, as shown on the bottom of Figure 5.8. Note that a dense point discretization was utilized, leading to numerical noise in curvature calculations; likewise larger road segment lengths generate less numerical noise.

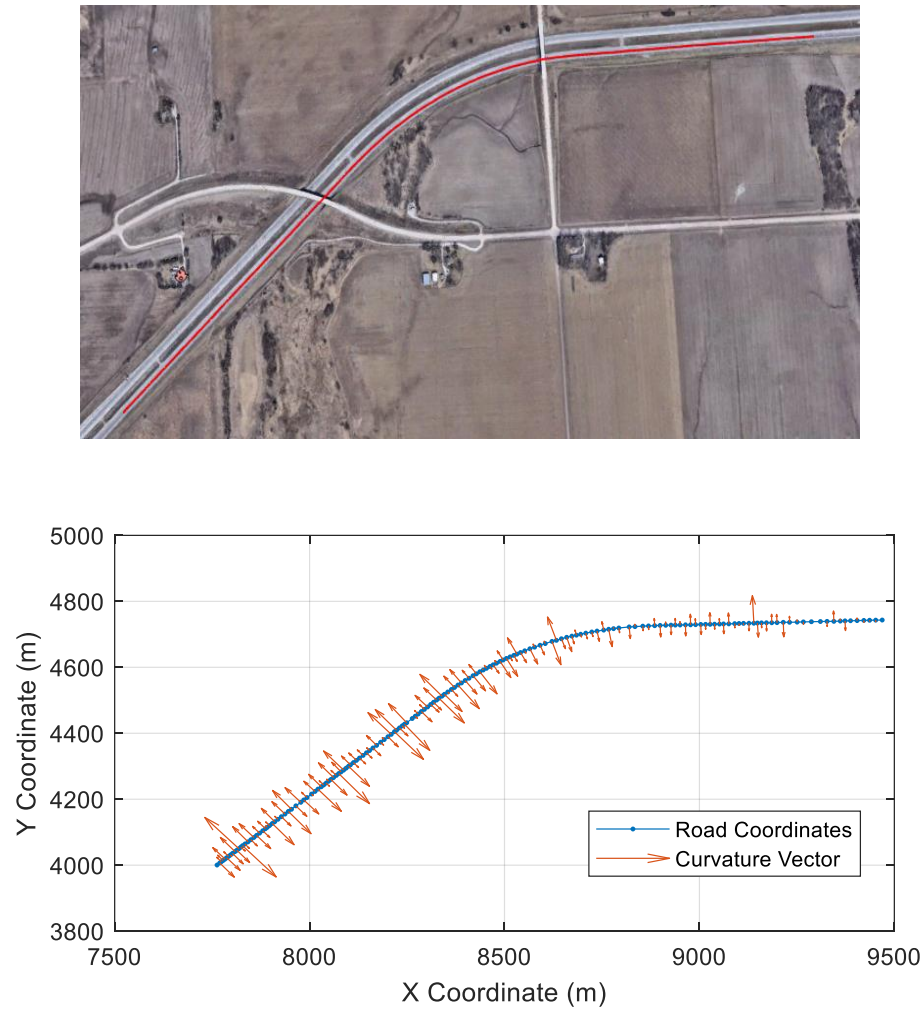


Figure 5.8 Road Highway from Satellite Images (top) and Road Profile with MDC Curvature Vectors (bottom)

Using orthogonality of the curvature data, the road angle was identified through vector rotations. The angle was smoothed through a locally-weighted, quadratic-fit regression as shown in Figure 5.9 [62][63].

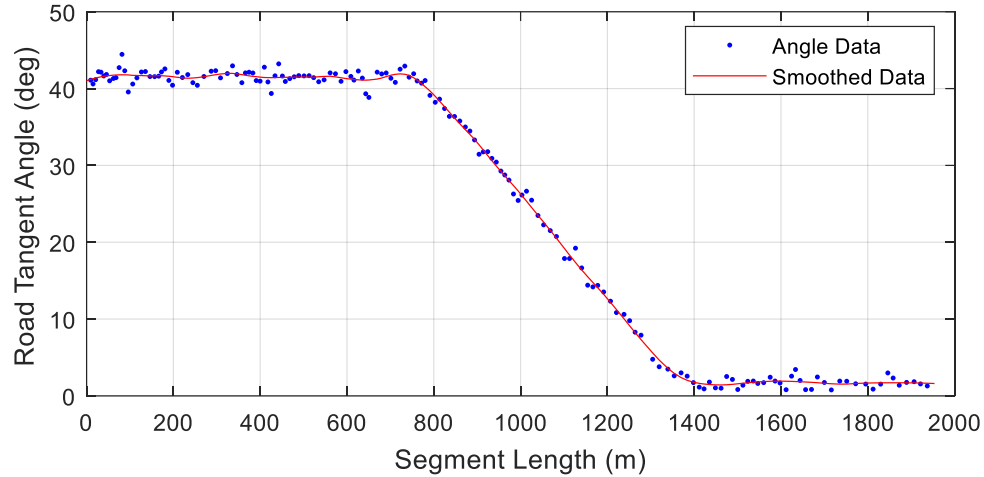


Figure 5.9 Road Tangent Angle and Data Smoothing

The smoothed angle is used to assign a local heading angle reference for the vehicle to use during simple curve maneuvering, as shown in Figure 5.10. Subsequently, a smoothed-curvature calculation was developed, and a simplified, piecewise-linear curvature relationship was used to condense road reference data into a compact segmentation scheme.

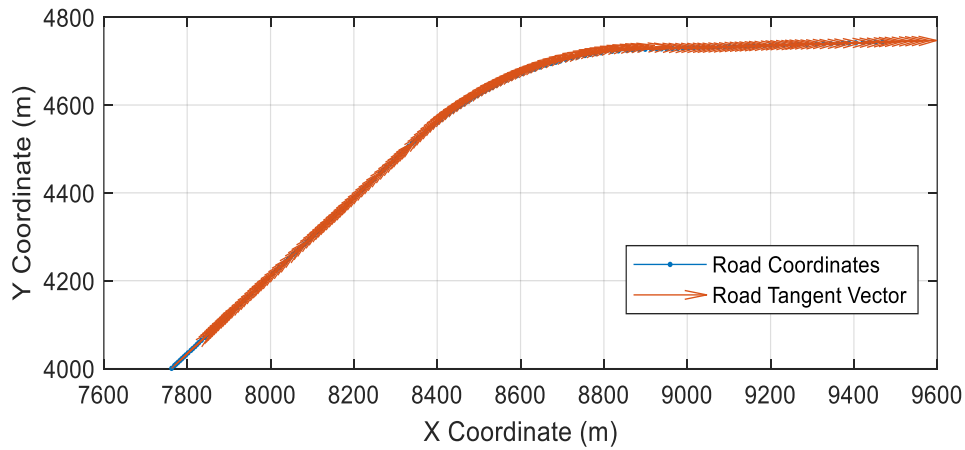


Figure 5.10 High Discretization for Simple Curve with Heading Angle Reference.

As a result, the filtered road angular data is used to identify smoothly varying curvatures with a piecewise-linear curvature function. It has been demonstrated that this

piecewise-linear curvature fit produces pristine, smooth road centerlines and can be used in an optimization routine to map a condensed, segmented, high-precision and adjustable lane location spatial map and augmented curvature and angle data [64].

The dense discretization was shown to illustrate the robustness of the MVRC method. Sparse segmentation of the same road profile was mapped using the MVRC method, which produced very smoothly-varying road heading and curvature vector data without additional smoothing or realignment processing, as shown in Figure 5.11. However, low-density spatial segmentation may require careful selection of road reference points, to accurately identify the transitions in curvature between consecutive road segments.

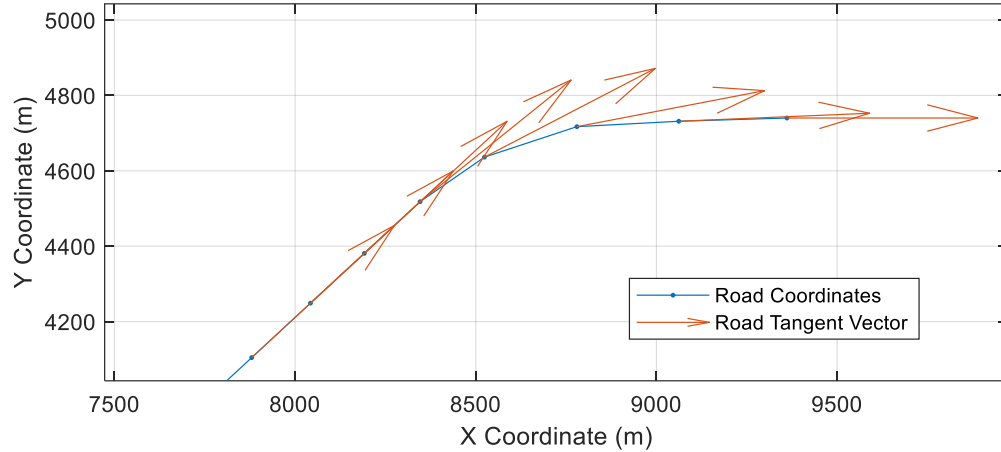


Figure 5.11 Low Discretization Simple Curve with Heading Angle Reference

Furthermore, calculations performed on a single lane can be extrapolated to adjacent, parallel (non-intersecting) lanes along lines of isocurvature using the lane width. All roadways with multiple concurrent lanes in the same travel direction have strictly reinforced parallel lane tangencies relative to the road cross-section. In other words, roads

with multiple lanes in a given travel direction will have parallel heading angles along the curvature vector lines, which are orthogonal to the roadway. As a result, once a single-lane geometry is identified, adjacent lanes may be easily and consistently described by adjusting the local lane curvature magnitude and offsetting lane reference point data by an equivalent amount to the lane centerline separation distance (i.e., lane widths). In addition, branching structures, which conjoin or separate from roads, are currently very difficult to implement into robust map frameworks. Branching structures, such as entrance or off-ramps, lane mergers, etc., may utilize identical data as lanes from a determined starting location, and preliminary research indicates this framework remains functional even for these unique cases. Lane offsets are discussed in detail by Jacome et al [64]. Lastly, rural and largely unmarked roads may not utilize discrete lanes but rather a shared multi-directional lane space. Integrating unmarked roads may require completely novel guidance approaches, as typical trajectories on unmarked roads trend to the center of the roadway, whereas opposite-direction passing on unmarked roads is accomplished when both vehicles shift laterally within the defined road width. Further research is being developed for the MVRC road data set. For further information on the extensions of the MVRC map, readers are referred to [64].

Recall that existing guidance frameworks use either predefined waypoint follower, ad hoc, or high-resolution maps with extracted lane boundary data to estimate curvature, which is essential for automated vehicles to estimate steering angle and safe operating speeds when navigating curves. The MVRC map produces this data a priori and provides it to the vehicle with road reference marker location for lane centerline, representing the

preferred location of the vehicle. The computational efficiency of the MVRC map is easy to identify: the densely-discretized data for the 2 km length of road mapped in this paper was only 8 kB, before compacting and optimizing the road segmentation. Assuming a typical highway speed limit of 25 m/s, the approximate amount of data processed by LiDAR for high-definition maps with the same distance is 80 GB, a $\sim 10^7$ order of magnitude difference for describing the same road [65].

5.3.4 Augmented Road Data

The MVRC map framework is intended to provide dynamically consistent, spatially-discretized data, which can be implemented into kinematic and kinetic trajectory estimations in relationship, to speed and acceleration. Although details of the road data augmentation are beyond the scope of this paper and are addressed in additional papers submitted by the authors, the composition of the augmented data are described here.

First, vertical deviations in the road may affect both road segment lengths between reference points and vehicle stability. MVRC map data is augmented with a lane elevation values (relative to sea level) and dynamic rotations capturing the lateral slope of the road, which may include lane crowning, superelevation, road twist, and road pitch at multiple reference points.

Second, vehicle-control optimization schemes have been identified to obtain velocity profiles based on properly extracting curvature data [64]. These velocity profiles are dependent on the limits of local tire-roadway friction, horizontal and vertical curvature, horizontal wind shear, and lateral road slope. Although the initial concept for the optimization approach was intended for dynamic CAV vehicle planning, an extension of

this technique will allow remote road controllers (e.g., state Departments of Transportation or DOTs) or reference datasets, such as the precipitation and temperature map from the National Oceanographic and Atmospheric Administration (NOAA), to temporarily modify the limiting road friction in a region, achieving a remotely-controlled variable speed limit.

It is possible that augmentation of data provided on [64] can further adjust local parameters such as friction to assess traffic flow in CAVs under multiple scenarios. DOT administrators can manually adjust lane-specific speed limits to accommodate for work zone construction, weather changes (affecting the maximum allowable friction by either ice or snow), lane closings, lane merging, or reducing speed limits not available from signs.

Third, vehicle-to-infrastructure communication may also be conducive to real-time traffic congestion and route planning maps. Using third-party or passive observer (e.g., cellular communication) techniques and vehicle-reported average travel speed through road segments, congestion and travel times may be predictable. Data augmentation may improve end-to-end destination planning and route optimization for enhanced automated vehicle travel.

An example of MVRC road data input is shown in Table 5.1 and an ArcGIS map is show in Figure 5.12 to illustrate the curvature of the road per segment length available to the vehicle.

TABLE 5.1 MVRC ROAD DATA SAMPLE

Latitude	Longitude	Curvature (10^{-3} m^{-1})	Segment Length (m)
40.89054275	-96.67512273	0	0
40.89169123	-96.67331671	0.0107	198.59
40.89301687	-96.67124164	0.0155	228.60
40.89414874	-96.66945791	0.013	195.96
40.89506415	-96.66800844	0.888205	158.93
40.89592139	-96.66612935	1.164702	184.77
40.89655836	-96.66329365	1.039262	249.23
40.89663343	-96.66050674	0.129552	235.01
40.89664038	-96.65733051	0.0107	267.67
40.89664966	-96.65503712	0	193.27
40.89054275	-96.67512273	0	0
40.89169123	-96.67331671	0.0107	198.59

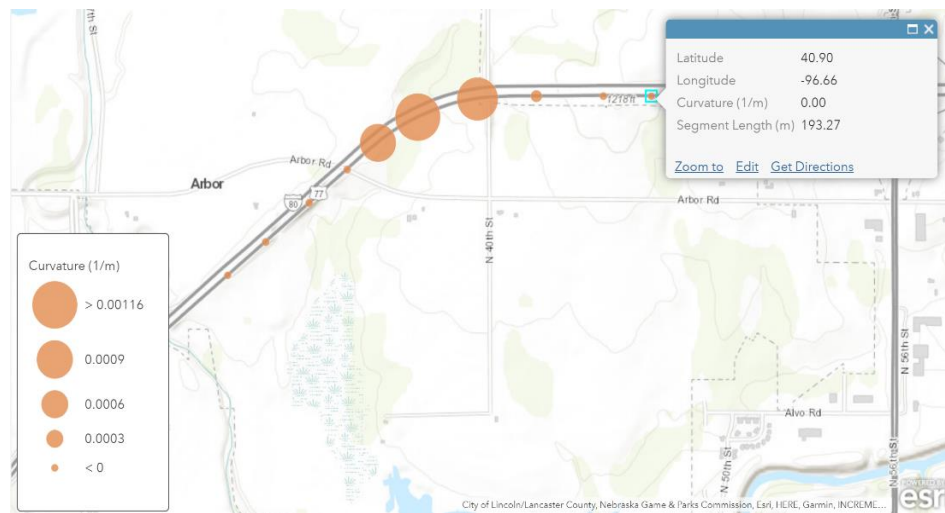


Figure 5.12 ArcGIS Road Data Example

5.4 Discussion and Implementation of Map Framework

The MVRC road database was constructed to complement current CAV efforts by making a road dynamic reference output as concise and simplified as possible. Currently, multiple data exchange methods exist for CAVs including: conventional GPS applications in phones, RSUs vehicle On-Board Units with Dedicated Short-Range Communications,

and simultaneous communication with vehicle's On-Board Units. The MVRC map can provide current CAVs and controller technologies, a sensor-independent driving reference constructed from external sources.

The fidelity of the method is dependent on the initial data map extraction, which can be complemented by multiple road-data extraction techniques such as LiDAR, or satellite imaging as previously shown. Current work in progress is focused on the extraction of lane edge coordinates, and trajectory generations based on differential geometry principles, and supplementary vehicle positioning research. Investigators are encouraged to use the provided findings to implement the MVRC data into their own research. This can be achieved by exploring multiple sources of data map and evaluate the performance of the method. Implementation of the MVRC map data into automated systems may require some adaptation but was intended for smooth, convenient integration.

5.5 Conclusions

The presented work aimed to provide the reader with a complete and thorough overview of CAV technology frameworks available. Multiple efforts to arrive at a level five autonomous vehicle were described, and an alternative framework was constructed based on the characteristics wherein other methods were not designed to operate. The method provided reasonable road-tangent angle profiles to aid autonomous navigation from satellite imaging and GPS coordinates. Roads were segmented into curved and straight segments for continuous roads.

Further augmentation of the MVRC map data is possible to better synergize with other existing technologies and guidance frameworks. Researchers encourage the broad

collaboration and expansion of the data to bridge gaps between multiple contributors and end-users of the data. Once the vehicle's position can be established, the map provides an outlook beyond what sensors are capable of estimating. As a result, even rural, unpaved, unmarked low-traffic roads could be reasonably mapped with enough accuracy to permit automated navigation; however, new reaction and control methods may need to be developed to address opposite-direction vehicle navigation on these roads that are frequently narrow. When coupled with a wireless vehicle communication system, the value of the detailed MVRC map increases with rapid road network updates, vehicle data feedback about current travel speeds, road conditions (including friction), crash events, disruptions, road congestion, and a potential for arbitrary point-to-point navigation.

It is worth noting that the proposed framework is intended to complement the guidance and trajectory prediction techniques utilized by CAVs. Data provided by the MVRC system could compliment systems such as machine vision and waypoint follower techniques, offering an extra layer of redundancy for normal driving operations and for critical information when sensor-extracted data is poor (e.g., snow). Further investigation, testing, and augmentation on the proposed MVRC method could pose a vehicle reference independent of environmental sensors that limit current CAV navigation. Thus, providing the ability to navigate under impairing conditions such as harsh weather and considerably improve the performance of CAVs.

5.6 References

- [1] J. Benson, B. C. Tefft, A. M. Svancara, and W. J. Horrey, "Potential Reductions in Crashes, Injuries, and Deaths from Large-Scale Deployment of Advanced Driver

- Assistance Systems,” Research Brief. Washington, D.C.: AAA Foundation for Traffic Safety, 2018.
- [2] M. A. Mollenhauer, T. A. Dingus, C. Carney, J. M. Hankey, and S. Jahns, “Anti-Lock Brake Systems: An Assessment of Training on Driver Effectiveness”, Accident Analysis and Prevention, Vol 29 Issue 1, 1997, pp 97-108.
- [3] National Highway Transportation Safety Administration (NHTSA), Federal Motor Vehicle Safety Standards; Electronic Stability Control Systems; Controls and Displays, Notice of final rule, 49 CFR Parts 571 and 585 (Docket No. NHTSA-2007-27662), March 2007.
https://www.nhtsa.gov/sites/nhtsa.dot.gov/files/fmvss/ESC_FR_03_2007_0.pdf
- [4] “Front crash prevention slashes police-reported rear-end crashes”, Insurance Institute for Highway Safety (IIHS) and Highway Loss Data Institute (HLDI), January 28, 2016. <https://www.iihs.org/news/detail/front-crash-prevention-slashes-police-reported-rear-end-crashes>
- [5] “Lane departure warning, blind spot detection help drivers avoid trouble”, Insurance Institute for Highway Safety (IIHS) and Highway Loss Data Institute (HLDI), August 23, 2017. <https://www.iihs.org/news/detail/stay-within-the-lines-lane-departure-warning-blind-spot-detection-help-drivers-avoid-trouble>
- [6] USDOT Intelligent Transportation Systems Office - Connected Vehicle Pilot Deployment Program, Retrieved from, <https://www.its.dot.gov/pilots/index.htm>. Accessed on: May 16, 2019.

- [7] Tampa (THEA) Pilot - Connected Vehicle Pilot Deployment Program [Online] Available: https://www.its.dot.gov/pilots/pilots_thea.htm, Accessed on: May 16, 2020
- [8] WYDOT Connected Vehicle Pilot Program, Date of Access: 5/16/2020. Retrieved from, <https://wydotcvp.wyoroad.info/>
- [9] J. Chang, An Overview of USDOT Connected Vehicle Roadside Unit Research Activities, USDOT May 2017, Publication Number: FHWA-JPO-17-433.
- [10] Y. Song and C. Liao, "Analysis and review of state-of-the-art automatic parking assist system," 2016 IEEE International Conference on Vehicular Electronics and Safety (ICVES), Beijing, 2016, pp. 1-6, doi: 10.1109/ICVES.2016.7548171.
- [11] C. Chen, B. Wu, L. Xuan, J. Chen, T. Wang, and L. Qian, "A Trajectory Planning Method for Autonomous Valet Parking via Solving an Optimal Control Problem", Sensors, Published November 11, 2020. doi:10.3390/s20226435
- [12] S. Xu, H. Peng, P. Lu, M. Zhu, Y. Tang, "Design and Experiments of Safeguard Protected Preview Lane Keeping Control for Autonomous Vehicles", IEEE, Published February 7, 2020. doi: 0.1109/ACCESS.2020.2972329
- [13] D. Urmson, et al, "Autonomous Driving in Urban Environments: Boss and the Urban Challenge", Journal of Field Robotics, Vol 25 Issue 8, pp 425-466, 2008. doi: 10.1002/rob.20255
- [14] I. Maqueda, A. Loquercio, G. Gallego, N. Garcia, and D. Scaramuzza, Event-based Vision meets Deep Learning on Steering Prediction for Self-driving Cars, Presented at the 2018 IEEE/CVF Conference on Computer Vision and Pattern Recognition, Salt Lake City, Utah, June 18-23, 2018.

- [15] J. Janai, F. Güney, A. Behl, and A. Geiger, "Computer Vision for Autonomous Vehicles: Problems, Datasets and State of the Art", Foundations and Trends® in Computer Graphics and Vision: Vol. 12: No. 1–3, pp 1-308, 2020. doi:10.1561/0600000079
- [16] "Taxonomy and Definitions for Terms Related to On-Road Motor Vehicle Automated Driving Systems", SAE Ground Vehicle Standard J3016, January 16, 2014. doi:10.4271/J3016_201401
- [17] Ohnsman, "Waymo Says More of its Self-Driving Cars Operating 'Rider-Only' With No one at Wheel", Forbes, Published October 28, 2019.<https://www.forbes.com/sites/alanoehnsman/2019/10/28/waymos-autonomous-car-definition-if-you-need-a-drivers-license-its-not-self-driving/?sh=692308056478>
- [18] Chin, Key Volkswagen Exec Admits Full Self-Driving Cars 'May Never Happen', TheDrive, January 13, 2020. <https://www.thedrive.com/tech/31816/key-volkswagen-exec-admits-level-5-autonomous-cars-may-never-happen>
- [19] NHTSA. Driver Assistance Technologies. Retrieved from nhtsa.gov: <https://www.nhtsa.gov/equipment/driver-assistance-technologies>, 2019.
- [20] B. S. Jahromi, T. Tulabandhula, and S. Cetin, "Real-Time Hybrid Multi-Sensor Fusion Framework for Perception in Autonomous Vehicles", Sensors, Vol 19 Issue 4357, October 9, 2019. doi:10.3390/s19204357
- [21] K. Jo, C. Kim, and M. Sunwoo, "Simultaneous Localization and Map Change Update for the High-Definition Map-Based Autonomous Driving Car", Sensors, Vol 18 Issue 9, 2018. doi:10.3390/s18093145

- [22] D. Simon, “Optimal State Estimation: Kalman, H Infinity, and Nonlinear Approaches,” Wiley-Interscience. 2006.
- [23] S. M. LaValle, Planning Algorithms, Cambridge University Press. 2006.
doi:10.1017/CBO9780511546877
- [24] S. Liu, L. Li, J. Tang, W. Shuang, & J. L. Gaudiot. Creating Autonomous Vehicle Systems, vol. 6. Morgan & Claypool Publishers. 2017,
doi:10.2200/S00787ED1V01Y201707CSL009
- [25] L. Claussmann, M. Revilloud, D. Gruyer, & S. Glaser, “A Review of Motion Planning for Highway Autonomous Driving,” IEEE Transactions on Intelligent Transportation Systems, 1826-1848. 2019 doi:10.1109/TITS.2019.2913998
- [26] J. Horst, & A. Barbera, “Trajectory Generation for an On-Road Autonomous Vehicle,” Journal of Research of the National Institute of Standards and Technology. 2005.
- [27] R. T. Farouki, Pythagorean-Hodograph Curves: Algebra and Geometry Inseparable, Springer. 2008
- [28] D. Liberzon “Calculus of Variations and Optimal Control Theory: A Concise Introduction,” Princeton University Press. 2012.
- [29] P. Falcone, H. E. Tseng, F. Borrelli, F. Asgari, & D. Hrovat, “Predictive Active Steering Control for Autonomous Vehicle Systems,” IEEE Transactions on Control Systems Technology, 15(3), 566-580. 2007.
- [30] N. M. Enache, S. Mammar, M. Netto, & B. Lusetti, “Driver Steering Assistance for Lane Departure Avoidance Based on Hybrid Automata and Composite Lyapunov

- Function,” IEEE Transactions on Intelligent Transportation Systems, 11(1), 28-29. 2010.
- [31] D. González, J. Pérez, V. Milanés, and F. Nashashibi, “A Review of Motion Planning Techniques,” IEEE Transactions On Intelligent Transportation Systems, 17(4), 2016, pp 1135-1145.
- [32] NHTSA. “Automated Driving Systems,” Retrieved from nhtsa.gov: <https://www.nhtsa.gov/es/vehicle-manufacturers/automated-driving-systems>. 2020
- [33] M. J. Olsen, C. Parrish, E. Che, J. Jung, and J. Greenwood, “Lidar for Maintenance of Pavement Reflective Markings and Retroreflective Signs”
- [34] J. Kalchbrenner, “Large Glass Beads for Pavement Markings,” Transportation Research Board, Washington, D.C., Jan. 1989, ISSN: 0361-1981
- [35] M. Gao, C. Chen, J. Shi, S. Lai, Y. Yang, and Z. Dong, “A Multiscale Recognition Method for the Optimization of Traffic Signs Using GMM and Category Quality Focal Loss,” Sensors 20, no. 17: 4850. 2020.
- [36] S. Eickeler, M. Valdenegro, T. Werner, and M. Kieninger “Future Computer Vision Algorithms for Traffic Sign Recognition Systems,” Advanced Microsystems for Automotive Applications. Springer, Cham. 2016. doi:10.1007/978-3-319-20855-8_6
- [37] J. Cao, C. Song, S. Peng, F. Xiao, and S. Song, “Improved Traffic Sign Detection and Recognition Algorithm for Intelligent Vehicles,” Sensors 19, no. 18: 4021, 2019.

- [38] L. Abdi and A. Meddeb. “Deep learning traffic sign detection, recognition and augmentation,” SAC '17: Proceedings of the Symposium on Applied Computing, April 2017 Pages 131–136, doi: 10.1145/3019612.3019643
- [39] Y. Yang, S. Liu, W. Ma, Q. Wang, and Z. Liu, “Efficient Traffic-Sign Recognition with Scale-aware CNN,” British Machine Vision Conference 2017.
- [40] K. Eykholt, I. Evtimov, E. Fernandes, B. Li, A. Rahmati, C. Xiao, A. Prakash, T. Kohno, and D. Song, “Robust Physical-World Attacks on Deep Learning Visual Classification,” Conference on Computer Vision and Pattern Recognition. 2018.
- [41] C. Sitawarin, A. N. Bhagoji, A. Mosenia, P. Mittal, and M. Chiang, “Rogue Signs: Deceiving Traffic Sign Recognition with Malicious Ads and Logos”. 2018.
- [42] S. Temel, M. C. Vuran, and R. K. Faller, “A Primer on Vehicle-to-Barrier Communications,” Vehicular Technology Conference. 2016.
- [43] S. Glaser, S. Mammar, and C. Sentouh, “Integrated Driver-Vehicle-Infrastructure Road Departure Warning Unit,” IEEE Transactions on Vehicular Technology, 59(6), 2757-2771, 2010.
- [44] R. K. Jurgen, “V2V/V2I Communications for Improved Road Safety and Efficiency,” SAE International. 2012.
- [45] S. Temel, M. C. Vuran, M. M. Lunar, Z. Zhao, A. Salam, R. K. Faller, & C. Stolle, “Vehicle-to-Barrier Communication During Real-World Vehicle Crash Tests,” Computer Communications. 2018, doi:10.1016/j.comcom.2018.05.009
- [46] S. Andrews, “Vehicle-to-Vehicle (V2V) and Vehicle-to-Infrastructure (V2I) Communications and Cooperative Driving,” Eskandarian A. (eds) Handbook of Intelligent Vehicles. 2012, doi:10.1007/978-0-85729-085-4_46

- [47] H. B., Pacejka, “Tyre and Vehicle Dynamics,” Butterworth-Heinemann. 2006.
- [48] T. D. Gillespie, “Fundamentals of Vehicle Dynamics,” SAE International. 1992.
- [49] AASHTO. “A Policy on Geometric Design of Highways and Streets (The Green Book),” (Sixth Edition ed.). Washington D.C.: American Association of State Highway and Transportation Officials. 2011.
- [50] IDOT. “Street Design Manual: Spiral Curves,” Iowa Department of Transportation. 2010.
- [51] O. M. O'Reilly, “Engineering Dynamics: A Primer,” Springer Science & Business Media. 2010.
- [52] SAE. “J670 Vehicle Dynamics Terminology,” SAE International. 2008.
- [53] M. Werling, J. Ziegler, K. Soren, and S. Thrun, “Optimal Trajectory Generation for Dynamic Street Scenarios in a Frenet Frame,” IEEE International Conference on Robotics and Automation, pp. 987-993. 2010, doi:10.1109/ROBOT.2010.5509799
- [54] M. P. do Carmo, “Differential Geometry of Curves and Surfaces,” Englewood Cliffs, N.J: Prentice-Hall. 1976.
- [55] E. Kreyszig, “Differential Geometry,” (1st ed.). Dover Publications. 1991
- [56] M. Brezak and I. Petrović, “Real-time Approximation of Clothoids With Bounded Error for Path Planning Applications,” IEEE Transactions On Robotics, 30(2), 507-515. 2014.
- [57] L. Tang, Y. Shi, Q. He, A. W. Sadek, and C. Qiao, “Performance Test of Autonomous Vehicle Lidar Sensors Under Different Weather Conditions,” SAGE Journals, 319-329, 2020, doi:10.1177/0361198120901681

- [58] B. Hillel, R. Lerner, D. Levi, and G. Raz, “Recent progress in road and lane detection: a survey,” Springer. 2010, doi:10.1007/s00138-011-0404-2
- [59] J. P. Snyder, 1987; Map Projections - A Working Manual. U.S. Geological Survey Professional Paper 1395, 383 p.
- [60] Department of Army, 1973; Universal Transverse Mercator Grid, U. S. Army Technical Manual TM 5-241-8, 64 p. Superseded by DMATM 8358.2 The Universal Grids. UTM and Universal Polar Stereographic.
- [61] R. Jacome, C. Stolle, and M. Sweigard “Road Curvature Decomposition for Autonomous Guidance,” SAE Technical Paper 2020-01-1024. 2020, doi:10.4271/2020-01-1024
- [62] W. S. Cleveland, and C. Loader, “Smoothing by Local Regression: Principles and Methods,” In Statistical Theory and Computational Aspects of Smoothing. 1996.
- [63] M. T. Heath, “Scientific Computing: An Introductory Survey,” SIAM. 2018.
- [64] R. Jacome, C. Stolle, and M. Sweigard, “Smart-Barrier Concept for Mitigating Road Crashes Year 3 Report,” Mid-America Transportation Center, 2020.
- [65] I. Maksymova, C. Steger, and N. Druml, Review of LiDAR Sensor Data Acquisition and Compression for Automotive Applications, Proceedings 2018, 2, 852; doi:10.3390/proceedings2130852

CHAPTER 6. OPTIMIZATION OF ROAD REFERENCE PROFILES FOR CONNECTED AND AUTOMATED VEHICLES

Ricardo O. Jacome¹, Cody S. Stolle¹, George Grispos¹

University of Nebraska-Lincoln, WHIT 136, Lincoln, NE 68588, USA

¹Corresponding author. E-mail addresses: rjacome@unl.huskers.unl.edu (R.O. Jacome),
cstolle2@unl.edu (C. S. Stolle), ggrispos@unomaha.edu (G. Grispos)

Abstract

Vehicles with self-driving capabilities have been improving occupant safety in the last decade by reducing crash risks. Their operations rely on the effective use and interpretation of sensor data. However, data collected by sensors during adverse environmental conditions may be less reliable, and could lead to poor vehicle guidance resulting in severe crashes. Consequently, research on Vehicle-to-Infrastructure (V2I) technology may provide a beneficial compliment to fully or partially “ad hoc” guidance from Sensor Fusion. To address the research gaps previously outlined on the roadmap database “Midwest Virtual Road Corridor” (MVRC), a speed optimization methodology is proposed to efficiently control the vehicle while navigating MVRC-defined routes. The routines are based on vehicle dynamics and street design standards as per the American Association of State Highway and Transportation Officials (AASHTO). Outcomes including guidance reference parameters such as curvature, velocity, and wheel angle are analyzed. Results show that the reference velocity control profiles generated can be optimized to enhance existing V2I and autonomous vehicle technology.

Keywords: Accident prevention; Connected and Automated Vehicles; Vehicle dynamics; AASHTO; Vehicle-to-Infrastructure (V2I)

6.1 Introduction

Current automated vehicle applications use optic sensors that perform object detection/classification, lane identification, blind spot monitoring and automatic braking for crash avoidance or mitigation [1][2][3][4]. At the same time, V2I communications is under development to augment or replace “ad hoc” optic guidance techniques, providing insights of traffic data to connected vehicles [5][6]. Information exchanged includes traffic jams locations and traffic light “signal phase and timing” (SPAT) or weather change notifications [7][8][9]. However, vehicle guidance evolution to support connected and automated vehicle (CAV) navigation in difficult circumstances such as fog, snow, blowing dust, and in rural conditions including unpaved roads has proven very difficult.

Previous efforts at The University of Nebraska-Lincoln have develop a compact road map denoted as the Midwest Virtual Road Corridor or MVRC containing high-precision lane geometry data with supplementary discretized data including curvature, heading angle, segment length, and elevation, in support for an alternative V2I-based vehicle navigation approach for CAVs [10]. This paper uses the road reference path from the MVRC and demonstrates how vehicle inputs such as steering wheel angle and velocity can lead to optimized localized road conditions, and highway-specific designs. It is worth noting that the proposed routines do not overwrite current vehicle controller functions. By pairing the speed optimization functionality described in this paper with the MVRC road data, an essential safety complement can be realized for situations where vision or object

recognition faces difficulties, existing in conjunction with current controlling techniques. Control theory for autonomous vehicles is not explored nor discussed in this paper; the discussion is intended to denote the interaction between speed controllers and the new road data paradigm.

The structure of this paper continues with Section 6.2 on background information regarding road standard practices and vehicle dynamics. Section 6.3 introduces the optimization routine and layout of the methodology to produce it. Section 6.4 explains different mathematical road models to be studied based on road curvature. Section 6.5 details out the formulation of the proposed optimization algorithms. Section 6.6 views the implementation and results from Section. Finally, section 6.7 and 6.8 offer a discussion for further development and conclusions.

6.2 Background

The following section explains the background necessary to establish the proposed optimized reference path.

6.2.1 MVRC Overview

The MVRC consists of segmented roadways using high-precision GNSS reference points and consecutive connection anchor points. These points are prescribed with dynamic-attributes, such as curvature, turn direction, travel direction, lane width, lane elevation, and speed limit data [10]. The attributes are meant to be a reference from the standard Serret-Frenet Frame dynamics where the acceleration of a vehicle is described with [11]:

$$a = \dot{v}T + \frac{v^2}{\rho}N \quad (6.1)$$

a = Acceleration vector (m/s²)

v = Vehicle speed (m/s)

ρ = Radius of curvature of vehicle path at an instantaneous point (m)

N = Normal unit vector

T = Tangential unit vector

The numerical values for these data points are derived from multiple sources including geometric aspects. In this paper, only the connection between vehicle dynamics and road design standards is explored.

6.2.2 Road Design

Highway design is based on a balance of friction supply and demand while performing turns. During cornering, centripetal forces are developed and if unsafe or unstable maneuvers are attempted, could result in vehicle rollover or yaw spinouts. Therefore, road designs use limiting curvatures based on point-particle dynamic analysis formulated through Newton's Second Law of motion using both road and vehicle characteristics. Road design parameters include road friction, superelevation, and maximum width, while the vehicle parameters are velocity, acceleration, track width, and vehicle length. These are summarized with the following formula [12]:

$$\frac{v^2}{g\rho} = \frac{\mu + 0.01e}{1 - 0.01\mu e} \quad (6.2)$$

Where:

v = Vehicle velocity (m/s)

e = Superelevation (as a percentage)

g = Gravitational acceleration (9.81 m/s^2)

μ = Coefficient of side road friction

ρ = Radius of curvature (m)

In road design, curves are divided in two categories, horizontal and vertical curves.

Horizontal curves focus on an overhead view of street (latitude and longitude perspective), while vertical curves focus on a profile or elevation view of the street (altitude perspective) with reference to the horizontal curves [12]. Horizontal curve design can affect and govern vertical curve design. Horizontal curves are divided into 4 main categories shown in Figure 6.1, with the main difference related to radius of curvatures (denoted sometimes as spiral transitions) per road segment. In this paper, only two-dimensional horizontal curves are considered because their design is often the most relevant to prevent vehicles from departing a reference road. Further exploration of the influence of vertical curves will be explored in subsequent papers regarding the MVRC concise road map concept.

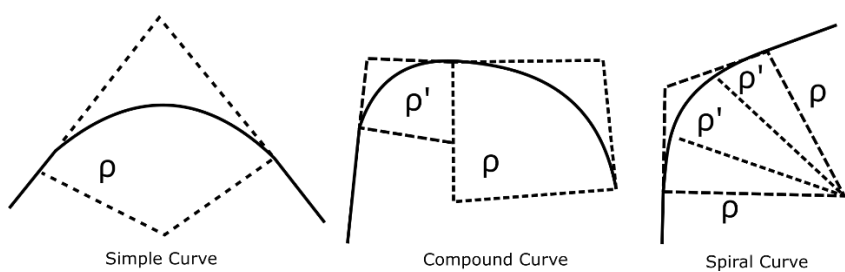


Figure 6.1 Example Horizontal Curves.

6.2.3 Vehicle Dynamics

AASHTO analysis is limited to primarily road parameters and point-particle dynamic analysis. During high-speed and low-speed cornering, a more thorough analysis of vehicle dynamics is necessary to develop a relationship between road data and vehicle data. From geometric considerations and Newton's Second Law and a limited-tire slip approximation, the Ackerman Steering relationship was developed [13]:

$$\delta = (57.3L + \eta v^2)\rho^{-1} \quad (6.3)$$

Where:

δ = Wheel directional angle (deg)

ρ = Radius of curvature (m)

v = Vehicle velocity (m/s)

L = Vehicle length (m)

η = Understeer gradient (deg-s²/m)

This formula relates the approximate “effective” wheel steer angle (or Ackerman’s angle) with the vehicle current state, offering more information of vehicle behavior while turning. Wheel steering angle controls the change of the heading vehicle angle. Thus, a proper maneuvering maintains the wheel steering angle under a range that does not cause the current vehicle angle to go on yaw instabilities. Since equations (6.1) through (6.3) present the radius of curvature as a shared parameter, the proposed routines optimize curvature $\kappa = \rho^{-1}$ to uniquely define a road reference.

6.3 Proposed Optimized References

With the MVRC, the tangent of the curvature vectors can be used as reference for vehicle heading angle at an instantaneous point in time [10][14]. In this paper, the previously developed MVRC data is optimized to offer extra guiding factors for CAV navigation independent of sensor data. Briefly, the proposed methodology is divided in four steps: obtaining curvature data, selecting a mathematical curvature model, perform least squares optimization, perform a general non-linear optimization for driving parameters. The four steps are summarized in Figure 6.2 below.

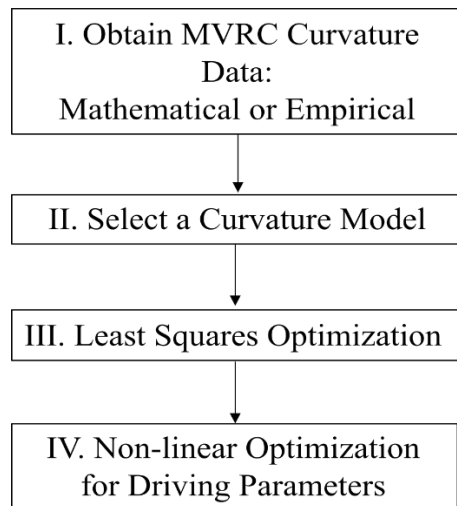


Figure 6.2 Organizational Flowchart of Study

This reference can be adjusted for multiple scenarios and parameters as desired by the user. However, on this paper, only changes in road friction due to weather conditions will be presented. For example, when rain is present, the coefficient of rolling friction in between the tire and roads is less than under dry, ideal conditions. Recalling equation (6.2), friction plays a role with the supply of friction available to the vehicle and therefore controls a maximum coupled vehicle velocity and curvature. Since the weather, and road

conditions are region-dependent, this reference will be denoted as regional road reference. The obtained regional road reference is useful for quantifying a safety-based speed management technique to accommodate curves, tire-pavement friction, and even work zone applications.

The first step to obtain curvature data will not be addressed in this paper, as it has been explored in previous studies [14]. Furthermore, methods for characterizing curvature such as camera recognition, lidar identification, and digital high-definition maps have been explored in the past [15][16]. Since there is a vast availability for road recognition that estimates road centerlines from satellite images, GPS data or any road coordinate collection system, the reader is referred to a more detailed take on the subject [17][18].

6.4 Mathematical Road Curvature Models

Following curvature data collection, a mathematical curvature model needs to be proposed in accordance with the trajectory requirements of CAVs. Most trajectory generation models in CAV research often take the quintic polynomial approximation [19][20]. These quintic models formulate the trajectory's curvature and/or position in 2-dimensional Euclidean space of a car, such that curvature is found as a function of arbitrary segment length s where:

$$\kappa(s) = a_0 + a_1s + a_2s^2 + a_3s^3 + a_4s^4 + a_5s^5$$

a_i = Values that determine the shape of the curvature function with $i \in [1,5]$

Studies of horizontal curves as shown in Figure 6.1 indicate that most highway street designs are made with curvatures having constant, and/or linear slopes. Differing from driving considerations, quintic polynomials do not offer the curvature characteristics for

which a road is designed. In this study, a curvature model is proposed considering aspects of highway design. This model is a semi-linear piecewise model as follows:

$$\begin{aligned}\kappa_1 = & \left(\frac{x_5}{x_2 - x_1} \right) (s - x_1)[\varphi(s - x_1) - \varphi(s - x_2)] \\ & + x_5[\varphi(s - x_2) - \varphi(s - x_3)] \\ & + \left(\left(\frac{x_5}{x_4 - x_3} \right) (-s + x_3) + x_5 \right) [\varphi(s - x_3) - \varphi(s - x_4)]\end{aligned}\quad \text{M.1}$$

Where:

$\varphi(s - a)$ = Unit Step Function with a shift of $a \in \mathbb{R}$

x_i = Values that determine the shape of the curvature function with $i \in [1,5]$

In this paper, it is noted the parameter s will be used exclusively as a position referenced to any general starting location, and not to an actual segment length estimated by other means. Thus, the segment length can be reset (i.e., $s = 0$) at each new or consecutive segment.

The model was mathematically designed to be continuous for all s but are only intended to model a single road section of $s \in [s_{initial}, s_{end}]$ which should contain only one curve section (e.g., not multiple horizontal curves). In this study, road sections are manually selected, but in practice, automated techniques such as machine learning should categorize longer road segments to assign the proposed model as one per road section. M.1 offers the flexibility of having its x_i parameters to be easily identified as basic geometric properties of a trapezoid. M.1 is illustrated in Figure 6.3 for the general model κ_1 along s with parameters x_i .

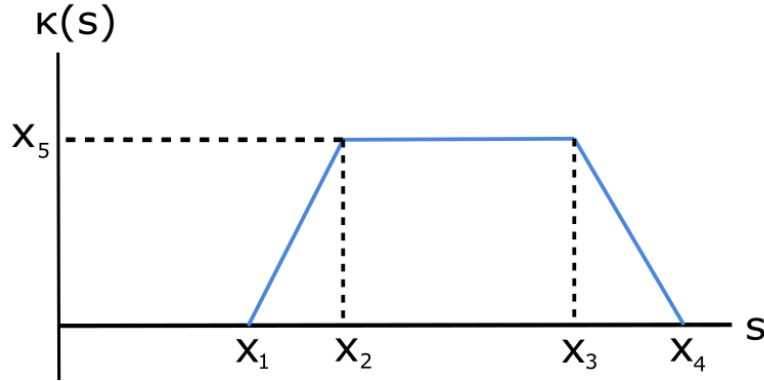


Figure 6.3 General Curvature M.1, with Design Values

6.5 Road Guidance Optimization Problem Formulation

The third step for the road reference is to shape the previous curvature model (from step II) to discrete curvature data (obtained from step I) through least squares minimization.

6.5.1 Least Squares Fitting

The models are subject to an unconstrained Least Squares Error - Minimization problem, denoted as Pr.1, such that [21]:

$$\min_x \|\kappa_M(s) - \hat{\kappa}[s]\|^2 \quad \text{Pr.1}$$

Where:

$\kappa_M(s)$ = Road curvature model M in terms of segment s and constants x_1, \dots, x_n

$\hat{\kappa}[s]$ = Discrete road sampled curvature data

This curve fitting minimization problem denoted as Pr.1 is used to test analytical curvature model M.1 with testing data. Pr.1 will focus on representing models $\kappa_M(x_1, \dots, x_n)$ as a representation of any generic road data input. The output of Pr.1 is

denoted as κ_{opt} or the optimal curvature profile given a dataset $\hat{\kappa}[s]$. Next, κ_{opt} is used in a general optimization routine for guidance parameters.

6.5.2 Regional Road Reference-Numerical Optimization Routine

As a vehicle increases speed, the friction supply available between the road and the tires decreases [13]. A vehicle's frictional demand is based on wheel angles with respect to the vehicle body, tire scrub, and relative speed between the tire and pavement interface. As the friction demand increases closer to the limit of the tire-pavement supply, the probability of a vehicle departing from the road at a curve increases. AASHTO has taken into consideration the reduction of friction supply associated with wet surfaces [12]. However, variability in tire conditions and road degradation affect considerably vehicle handling during cornering.

To enhance CAV driving, the regional road reference model uses (6.1) as an objective function and (6.2) as a constraint relating current AASHTO standards and instantaneous vehicle curvature. In general, there exists velocity ranges, and steering wheel angles such that extra constraints could be added to Pr.2 in the following manner [22][23]:

$$\min_y \frac{y_1^2}{g} \kappa_{opt}(s) - \mu \quad \text{Pr.2}$$

subject to:

$$v_{min} < y_1 < v_{max} \quad \& \quad \delta_{min} < y_2 < \delta_{max} \quad \text{C.1}$$

$$\frac{y_1^2}{g} \kappa_{opt}(s) - \frac{\mu + 0.01e}{1 - 0.01\mu e} = 0 \quad \text{C.2}$$

Where the variables to be optimized are denoted with y to distinguish from Pr. 3. In practice, velocity constraints can be pre-defined to be the same as the typical speed driven

in highways (i.e., 55-85 mph), while steering angle is limited to a range of ± 5 degrees for all four-wheeled vehicles [13]. It is important to note that Pr. 2 must be solved iteratively as many values the vector κ_{opt} contains. The implementation of the objective function minimization at each road segment is presented with the pseudo-code in Figure 6.4.

- Load Road Data
 - Calculate Discrete Curvature for Road Data $\kappa[s]$
 - Select a Curvature Model M.X
e.g., $M.1$
 - Solve Least Squares Optimization of M.X with Curvature Data $\hat{\kappa}[s]$
e.g., $Pr. I$
 - Obtain an Optimized Curvature $\kappa_{opt}(s)$
 - Define Road Parameters as appropriate
e.g., friction
- for Step = Initial Step: Total Steps in $\kappa_{opt}(s)$

 - Objective Function for Pr. 2
e.g., *Equation 1*
 - Define Constraints
e.g., *C.1 and C.2 Constraints*
 - Apply Non-Linear Solver to find Optimal driving parameters
 $[v_{opt}] = \text{Non-linear-Optimization-Solver}(\text{Eq.1}, \text{C.1}, \text{C.2})$
- end

Figure 6.4 Regional Road Reference Numerical Optimization Routine Pseudo Code.

6.6 Implementation of Optimization Routine in Different Datasets

This section implements the proposed curvature model and routines from sections 6.4 and 6.5. Two sample datasets are used: one ideal AASHTO consistent road and one empirical road model, extracted using Google Earth. The codes and datasets used in this section can be found in the references [24]. For this analysis, a constant superelevation profile will be analyzed at different friction levels, the road parameters used for all simulations in this paper are shown in Table 6.1.

Table 6.1 Road Constants for Optimization Model.

Road Parameter	Quantity
e	4%
μ_1	0.1
μ_2	0.3
μ_3	0.6
μ_4	0.8

These models will be defined with starting points $x_i \forall i \in [1, n]$ where n defines the total number of shape function values; for this study, $n = 5$. It is crucial to note, that for convergence of Pr.1 with any model curvature M.X, the initial condition must not be repeated and be incrementing values so that $x_j > x_{j-1} \forall j \in [2, n - 1]$. Excluding x_n , because is dependent on the maximum curvature rather than segment length.

6.6.1 Analysis for AASHTO Dataset

The previous derivation was intended for the selection of an optimized speed for safe navigation of a road in concert with friction supply and demand. The concept is illustrated here using an idealized roadway which was designed to be compliant with AASHTO standards. Least Squares Figure 6.5 shows the highway curve and the obtained fitted curvature model. It is noticeable that the mathematical construction of this road will lead to a perfect fit with no noise. The primary purpose of this was to study the robustness of the routine to fit curvature models under different initial conditions. Since this curve is mathematically compliant to road designs, the curvature profile represents a transition spiral, followed by a constant radius curve, an exit transition spiral, and a last segment of straight line.

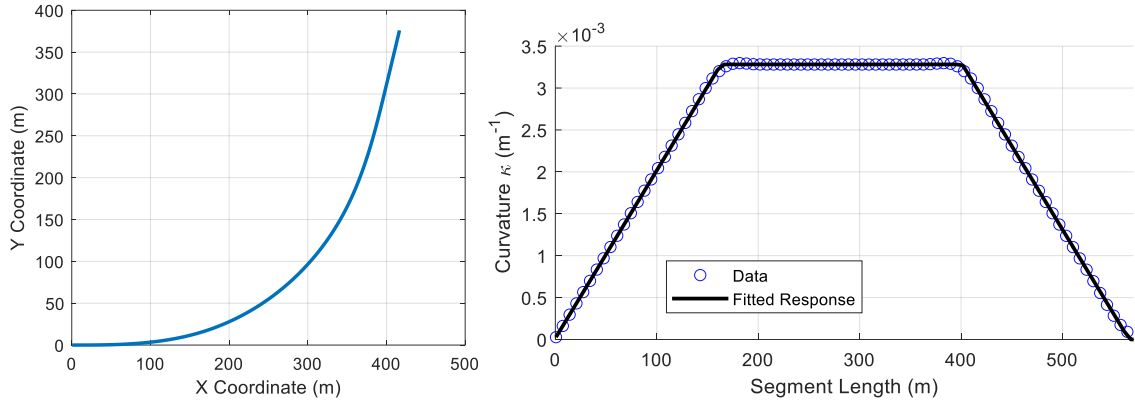


Figure 6.5 AASHTO Road (left) and Fitted Curvature Profile (right).

From the Least Squares Fitting analysis, it was determined that initial conditions followed a structure like the one presented in Table 6.2. The primary advantage of this setup is its versatility for implementation with machine learning techniques in determining the best initial conditions.

Table 6.2 Optimized Values for Curvature Model in AASHTO Dataset

Value	Initial Conditions	Optimized
x_1	$s_{initial}$	-0.763
x_2	$mean(s)$	163.075
x_3	$1.10 * mean(s)$	401.353
x_4	s_{final}	565.595
x_5	$\max(\kappa)$	0.0033

With the optimized model κ_{opt} , the remainder of the routine uses the routine in Pr.2 to obtain an optimized velocity profile for navigation of the road. The resulting velocity profile is shown in Figure 6.6, in which the overall reference speed increases as the road friction increases. It is noted how the profile for friction levels below 0.5 are optimized to have enter the constant radius curve at a slower speed, and then accelerate at the exit to arrive again the optimal speed available. As the friction reaches values higher than 0.5, the

results indicate that the vehicle can navigate through the half-kilometer curve with a constant speed of 38 m/s while maintaining stability.

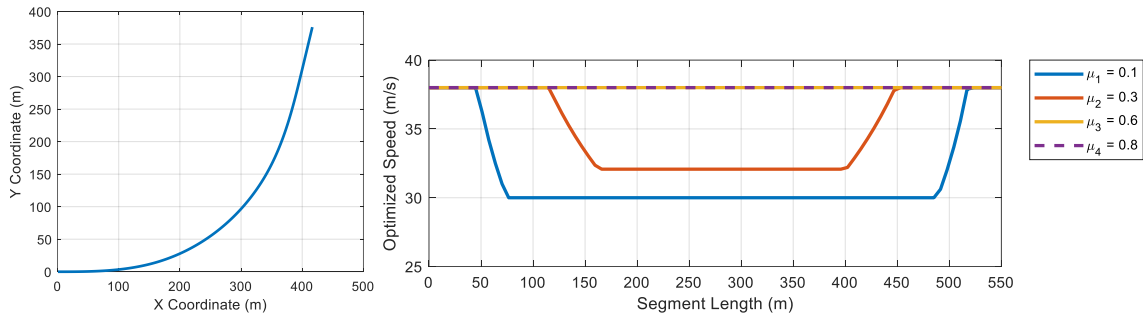


Figure 6.6 AASHTO Compliant Road (left) with Optimized Velocity Profile (right)

6.6.2 Analysis for Empirical Road Dataset

Next, authors extracted positional data for highway I-80 connecting the cities of Lincoln and Omaha in Nebraska (USA) for a practical “real world” evaluation of the recommended speed optimization method. The route was analyzed and observed to be within the AASHTO guidelines for curvatures and transitions. The segment is shown in Figure 6.7 (left) and its corresponding fitted curvature profile is shown in Figure 6.7 (right). Note that a locally weighted scatter plot smooth was used to reduce the noise in the sample [25].

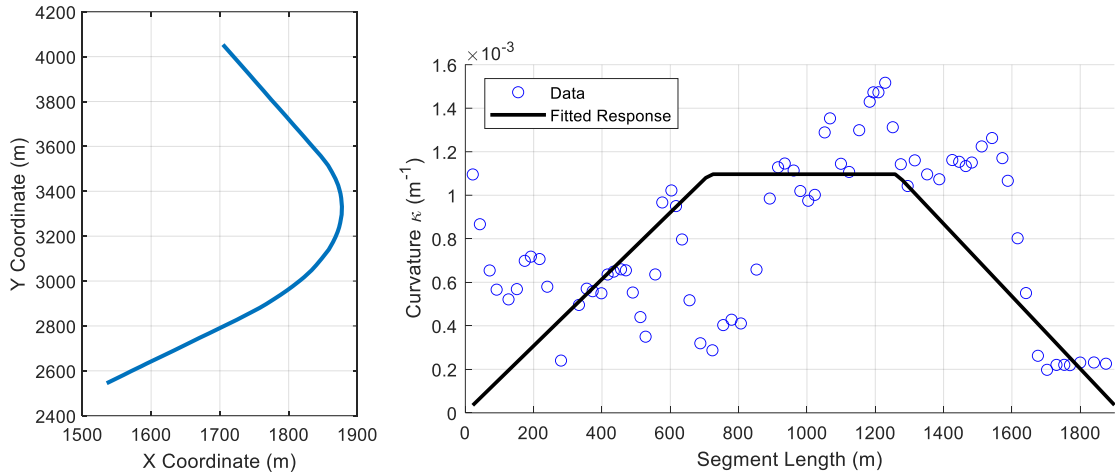


Figure 6.7 Empirical Road (left) and Fitted Curvature Profile (right).

Using the curvature profile, Least Squares Fitting yields the curvature model to be used in the two subsequent optimization routines. From the Least Squares Fitting analysis, the corresponding initial conditions are summarized in Table 6.3. It is noted how the values for x_2 and x_3 depend on coefficients (e.g., .75 and 1.90 for this section) that can be determined through machine learning. The selection of these initial conditions is crucial for the overall shape of the optimized fitted curvature model. However, since roads are designed from the same standards, the distribution of initial conditions is always proportional to the segment lengths, which is one main observation from this study. A generalized implementation of the concepts shown in this paper will include automated segmentation for analysis, and vehicle reactions using the speed governor approach discussed herein. It is anticipated that the automated extraction and processing of data can expedite conversion of road data into safe speed profiles compared to manual entry.

Table 6.3 Optimized Values for Curvature Model in Empirical Dataset

Value	Initial Conditions	Optimized
x_1	$s_{initial}$	-0.903
x_2	$.70 * mean(s)$	714.748
x_3	$1.25 * mean(s)$	1263.026
x_4	$.90 * s_{final}$	1921.747
x_5	$\max(\kappa)$	0.0011

Similar to section 6.6.1, the optimized model κ_{opt} was used in Pr.2 to obtain an optimized velocity profile for navigation of the road. The resulting velocity profile is shown in Figure 6.8, it is noted how the optimized velocity is considerably similar to the profile obtained by AASHTO standards. However, a key difference is at the friction level of about 0.3 at which the speed stays constant for the curve. Thus, the constructed road in this empirical example is considerably more stable at lower friction levels. This is attributed to the curve lasting for about 2 km or about 4 times longer than the critical AASHTO road example, which had a much larger maximum curvature [12].

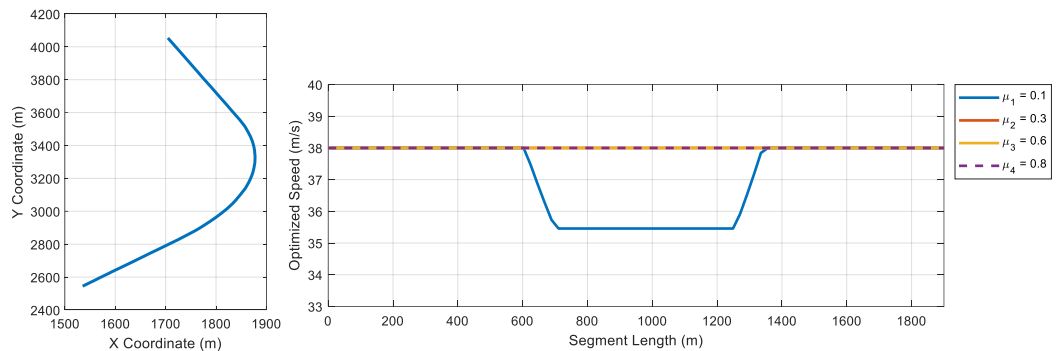


Figure 6.8 Empirical Road (left image) with Optimized Velocity Profile (right image)

6.7 Discussion on Alternative Applications

The proposed optimization routine augments the previous road map provided by the MVRC for aiding CAVs. However, the method shown in Figure 6.2 can be further implemented into other aspects of vehicle technology. Parting from the same step II to obtain κ_{opt} , and assuming that the vehicle can communicate back and forth with intelligent infrastructure, vehicle-specific references can be formed through equations (6.2) and (6.3). For this alternative routine Pr. 2, equation (6.3) will serve as an objective function to optimize vehicle-specific speed/angle combination under regional road conditions. Where vehicle velocity $v = y_1$ and steering wheel angle $\delta = y_2$ for every segment on $\kappa_{opt}(s)$ such that:

$$\min_y y_2 - (57.3L + \eta y_1^2) \kappa_{opt}(s) \quad \text{Pr.2}$$

subject to:

$$v_{min} < y_1 < v_{max} \quad \& \quad \delta_{min} < y_2 < \delta_{max} \quad \text{C.1}$$

$$\frac{y_1^2}{g} \kappa_{opt}(s) - \frac{\mu + 0.01e}{1 - 0.01\mu e} = 0 \quad \text{C.3}$$

Pr. 2 is a non-linear constrained optimization problem in which the vehicle parameters (L, η) and road parameters (μ, e) are regarded as constants for any generic road/vehicle. In this alternative routine, the particle dynamics' equation (6.2) is set as a constraint. Pr. 2 will find the optimized combination for both traveling velocity and wheel angle that uses the model $\kappa_{opt}(s)$ as part of their process. The following pseudo-code was created to illustrate this proposed optimization routine.

- Load Road Data
 - Calculate Discrete Curvature for Road Data $\kappa[s]$
 - Select a Curvature Model M.X
e.g., M.1
 - Solve Least Squares Optimization of M.X with Curvature Data $\hat{\kappa}[s]$
e.g., Pr. 1
 - Obtain an Optimized Curvature $\kappa_{Opt}(s)$
 - Define Vehicle/Road Parameters as appropriate
e.g., friction, gravity, understeer gradient, vehicle length
- for Step = Initial Step: Total Steps in $\kappa_{Opt}(s)$
- Objective Function for Pr. 2
e.g., Equation 3
 - Define Constraints
e.g., C.1 and C.2 Constraints
 - Apply Non-Linear Solver to find Optimal driving parameters
 $[v_{Opt}] = \text{Non-linear-Optimization-Solver(Eq.2,C.1,C.2)}$
- end

Figure 6.9 Vehicle-Specific Road Reference Numerical Optimization Routine Pseudo-Code.

For this optimization routine, road parameters are kept the same as Table 6.1. However, vehicle-dependent parameters are added as shown in Table 6.4. To summarize the process, both AASHTO and Google Earth models are shown in Figure 6.10 below, maintaining the corresponding initial conditions as per Table 6.2 and Table 6.3. In this model, lower allowable speeds are observed for the AASHTO speed profile at low friction levels, but overall speed behavior is the same. In this model, it is noted how the transitions from straight to constant radius requires a longer segment length available. Similarly, the empirical model has lower allowable speeds at lower friction levels, with a slightly longer transition needed compared to the Regional Road Reference.

Table 6.4 Vehicle-Specific Constants for Optimization Model [26]

Parameter	Quantity	Unit
η	1.95	degrees
L	2.5	meters

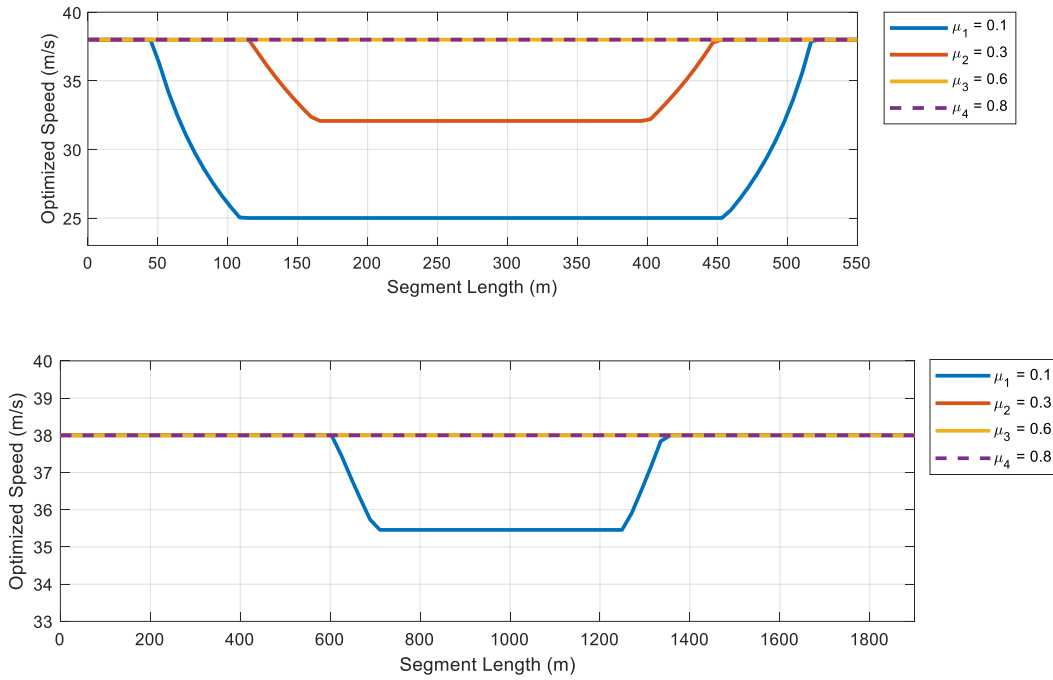


Figure 6.10 Vehicle-Specific Reference Velocity: AASHTO standards (top image) and Empirical (bottom image).

The developmental work shown in this paper is intended to provide a meaningful correlation between speed controllers and MVRC map data. Given the safety ramifications associated with speed controllers, it is likewise critical that proper data quality and traceback are included in the design and realization of any system which will interact with variable speed limit control and manipulation, from both the vehicle (user) and the adjustment (e.g., DOT) perspectives.

While several definitions for the term “data quality” have been proposed in the literature [27], in this discussion the most fitting definition is “data that are fit for use by data consumers” [28]. Hence, in the presented research study, the quality of data being

supplied to a vehicle should be sufficient to aid better traceback when errors occur or to clarify any confusion that could arise.

In order to achieve these objectives high quality data would need to be produced and provided by different data points along which the vehicle travels. One potential solution is to enhance the data quality through integration of forensic readiness principles into the design and development of data points along the vehicle path. While forensic readiness is traditionally used by businesses and organizations to ensure that maximize the potential use of digital evidence in corporate and legal scenarios [29], the same principles could be extended to the proposed research. For example, one of the principles of forensic readiness is to “define the business scenarios that require digital evidence” [29]. Hence, for vehicle-road interactions, road designers would need to consider the various scenarios that a vehicle will need (i.e., speed changes) in the event errors or corrections are needed. Likewise, another principle is that organizations “identify available evidence sources and different types of potential evidence” [29]. This study could be used to further enhance data quality that the vehicle receives, through proactive identification of data produced. It is also worth noting that high quality data generated by the integration of forensic readiness principles could also help enhance accident investigations (e.g., through stored velocity profiles), provide evidence of regulatory compliance, or simply be used by vehicle manufacturers to help improve the overall performance of the vehicle itself.

6.8 Conclusions

In this paper, an augmentation of the MVRC was presented, in which a methodology to obtain optimized velocity profiles was presented and analyzed. The methodology involved fitting curvature profiles that are constituent with AASHTO standards and then optimizing the reference velocity based on the aforementioned curvature profile. For this profile, the initial conditions of the function shape pose a major factor on the profiles obtained. Further research is being developed on the best estimation of initial conditions for the curvature model. Moreover, the selection of road segments in which the curvature profile can be estimated is also being researched with machine learning techniques.

Results showed a consistent velocity reference profile for both the mathematically designed road, and the extracted empirical profile. An optional routine was offered to accommodate for vehicle-specific parameters, the key difference was that velocity profiles were slower and required longer lengths for optimal navigation. Furthermore, the amount of friction available decreased considerably for the vehicle-specific model compared to that of the regional model. Results showed total road length was found to be a crucial factor on how the velocity profile is modeled.

Implementation of this method could result in an upgrade for autonomous vehicle technology in which weather disruptions and poor road markings could stop being a problem for future vehicle generations. In conclusion, the presented optimization routines offer the initial development on reference profiles for guidance in highway roads.

6.9 References

- [1] S. H. Naghavi and H. Pourreza, "Real-Time Object Detection and Classification for Autonomous Driving," 2018 8th International Conference on Computer and Knowledge Engineering (ICCKE), Mashhad, 2018, pp. 274-279, doi: 10.1109/ICCKE.2018.8566491.
- [2] Wu, J., Xu, H., & Zhao, J. (Spring 2020). Automatic Lane Identification Using the Roadside LiDAR Sensors. *IEEE Intelligent Transportation Systems Magazine*, 12(1), 25-34. doi:10.1109/MITTS.2018.2876559
- [3] Chen, C. T., & Chen, Y. S. (2009). Real-time approaching vehicle detection in blind-spot area. *IEEE*. doi:10.1109/ITSC.2009.5309876
- [4] Han., I. C., Luan, B. C., & Hsieh, F. C. (2014). Development of Autonomous Emergency Braking Control System Based on Road Friction. *IEEE International Conference on Automation Science and Engineering* (pp. 933-937). New York: IEEE.
- [5] Chang, J. (2017). An Overview of USDOT Connected Vehicle Roadside Unit Research Activities. U.S DOT. Washington D.C.: Federal Highway Administration Intelligent Transportation Systems (ITS) Joint Program Office. Publication Number: FHWA-JPO-17-433.
- [6] Arena, F., & Pau, G. (2019). An Overview of Vehicular Communications. *future internet*. doi:10.3390/fi11020027

- [7] USDOT. (2020, June 30). *USDOT Intelligent Transportation Systems Office - Connected Vehicle Pilot Deployment Program*. Retrieved from <https://www.its.dot.gov/pilots/index.htm>
- [8] WYDOT. (2020, May 16). *WYDOT Connected Vehicle Pilot Program*. Retrieved from <https://wydotcvp.wyoroad.info/>
- [9] Tampa (THEA) Pilot - Connected Vehicle Pilot Deployment Program [Online] Available: https://www.its.dot.gov/pilots/pilots_thea.htm , Accessed on: May 16, 2020
- [10] Jacome R. O., Stolle, C., Faller, R. K., Grispos, G., “A Dynamically-Concise Roadmap Framework for Guiding Connected and Automated Vehicles” IFIP/IEEE IM 2021 - 4th International Workshop on Intelligent Transportation and Autonomous Vehicles Technologies. Bordeaux, France, 2021, Manuscript Accepted for Publication
- [11] O'Reilly, O. M. (2010). Engineering Dynamics: A Primer. Springer Science & Business Media.
- [12] AASHTO. (2011). *A Policy on Geometric Design of Highways and Streets (The AASHTO)* (Sixth Edition ed.). Washington D.C.: American Association of State Highway and Transportation Officials.
- [13] Gillespie, T. D. (1992). *Fundamentals of Vehicle Dynamics*. SAE International.

- [14] Jacome, R., Stolle, C., & Sweigard, M. (2020). Road Curvature Decomposition for Autonomous Guidance. *SAE Technical Paper 2020-01-1024*. doi:10.4271/2020-01-1024
- [15] C. Wang, W. Miao and J. Zhao, "Vision-Based Curvature Model for Artificial Intelligence in Vehicles," *2012 International Conference on Control Engineering and Communication Technology*, Shenyang, China, 2012, pp. 245-248, doi: 10.1109/ICCECT.2012.194.
- [16] A. A. Assidiq, O. O. Khalifa, M. R. Islam and S. Khan, "Real time lane detection for autonomous vehicles," *2008 International Conference on Computer and Communication Engineering*, Kuala Lumpur, Malaysia, 2008, pp. 82-88, doi: 10.1109/ICCCE.2008.4580573.
- [17] Rangel Costa, G. H., & Baldo, F. (2013). A method to automatically identify road centerlines from georeferenced smartphone data. *GEOINFO 2013*.
- [18] Zhang, Y., Liu, J., Qian, X., Qiu, A., & Zhang, F. (2017). An Automatic Road Network Construction Method Using Massive GPS Trajectory Data. *International Journal of Geo-Information*. doi:10.3390/ijgi6120400.
- [19] Kelly, A., & Nagy, B. (2003). Reactive Nonholonomic Trajectory Generation via Parametric Optimal Control. *International Journal of Robotics Research*, 22(7-8), 583-601. doi:10.1177/02783649030227008
- [20] Minh, V. T. (2013). In T. Březina (Ed.), *Trajectory Generation for Autonomous Vehicles*. Springer International Publishing. doi:10.1007/978-3-319-02294-9_78

- [21] Nocedal, J., & Wright, S. J. (2006). Numerical Optimization. Springer.
- [22] Cho, Y. G. (2009). Vehicle steering returnability with maximum steering wheel angle at low speeds. *International Journal of Automotive Technology*, 10, 431-439.
- [23] Forkenbrock, G. J., & Elsasser, D. (2005). *An Assessment of Human Driver Steering Capability*. East Liberty, OH: National Highway Traffic Safety Administration Vehicle Research and Test Center.
- [24] Jacome, R. (2020). Road Data Optimization Reference for CAVs. *Mendeley Data*, 1. doi:10.17632/hbdy3cyckm.1
- [25] W. S. Cleveland, and C. Loader, "Smoothing by Local Regression: Principles and Methods," In Statistical Theory and Computational Aspects of Smoothing. 1996.
- [26] Dixit, N. R. (2009). *Evaluation of Vehicle Understeer Gradient Definitions*. Ohio.
- [27] G. Grispos, *On the enhancement of data quality in security incident response investigations*, Glasgow: University of Glasgow, 2016.
- [28] R. Y. Wang and D. M. Strong, ""Beyond accuracy: What data quality means to data consumers," *Journal of Management Information Systems*, pp. 5-33, 1996.
- [29] R. Rowlingson, "A ten step process for forensic readiness," *International Journal of Digital Evidence*, vol. 2, no. 3, pp. 1-28, 2004.

CHAPTER 7. ROAD ELEVATION REFERENCE FOR CONNECTED AND AUTOMATED VEHICLES FROM SERRET-FRENET FRAMES

Ricardo O. Jacome¹, Cody S. Stolle¹

University of Nebraska-Lincoln, WHIT 136, Lincoln, NE 68588, USA

¹ Corresponding author. *E-mail addresses:* rjacome@unl.huskers.unl.edu (R.O. Jacome), cstolle2@unl.edu
(C. S. Stolle)

Abstract

Highway roads typically conform to the elevation of the landscape near the roadway. However, elevation data, including vertical grade, sag or crest curves, and lateral elevation such as superelevation are not included in databases, and may only be indirectly identified from high-density point cloud data. To improve current approaches, a sensor-independent reference useful for identifying road elevation and recording data was developed to augment data collection for the Midwest Virtual Road Corridor (MVRC). The method utilizes vehicle dynamics concepts parting from the traditional Serret-Frenet formulation and generalizes to the case of modeling roads in three-dimensional space. This augmentation relies on measuring road grade from geodetic software and comparing it to empirical vehicle orientations. An experiment was performed to obtain vehicle on-board data and compare it with road grade reference. Results are analyzed and studied in the context of augmentation for the MVRC method.

Keywords: Autonomous Vehicles, Intelligent Transportation Systems, Serret-Frenet Dynamics, AASHTO, Street Design

7.1 Introduction

Vehicle autonomy often encounters difficulties in both road and weather conditions where sensor-vision quality is low, and identification difficult. For this reason, the MVRC was created as a backup system, in which the vehicle can access a description of dynamic road-attributes, commonly used in trajectory generation literature, to serve as a navigation reference independent of environment-recognition sensors [1]. In practice, vehicles obtain this dynamic-reference through wireless communications used in Connected and Automated Vehicles (CAVs) [2]. Multiple efforts have been deployed in the efficiency and large-scale implementation of wireless infrastructure communications and will not be explored in this paper. Readers are referred to the following references for a detailed treatise on the subject and its current implementation efforts [3][4][5].

Previously in the MVRC, road attributes were limited to two-dimensions, such that the aim of this paper is to augment the methodology into a three-dimensional reference scheme using empirical rotation angles. This extension will permit for elevation considerations in street design to be included [6]. To create this augmented reference, it is assumed that the vehicle's Euler Angles at an instantaneous point are approximately equal to the road's slope and superelevation. Thus, the measurements can be obtained through methods such as surveying, satellite imaging, LiDAR scanning, and vehicle recordings.

Current research has shown effective levels of superelevation measurements from kinematic data recordings and imaging processing data [7][8]. These methods have suffered from steady state errors produced by external sources including vehicle sprung mass attitude (yaw, pitch, and roll), aerodynamic drag, tire traction and compliance, and

road roughness. In literature, the contribution of these external factors is addressed by on-board state estimations techniques. Some techniques include Recursive Least Squares (RLS) with multiple forgetting factors, Dynamic Grade Observer (DGO), and Parallel Mass and Grade (PMG) estimations [9][10][11][12].

The present paper will explore a low-resolution geodetic elevation profiles, empirical recordings from a vehicle at a non-zero road grade, and data analysis in which the error difference is used as a main parameter on determining the quality of data for reference use. In summary, the proposed methodology uses empirical data to improve state estimation and augment the MVRC reference system to three-dimensions.

The remainder of this paper will be Section 7.2 on the proposed augmentation for the MVRC. Section 7.3 will focus on the experimental setup and Section 7.4 will encompass post-processing with data analysis. Finally, conclusions and recommendations are provided.

7.2 Proposed Three-Dimensional Augmentation of MVRC

In general, the MVRC method consists of two-dimensional motion with particle Serret-Frenet dynamics where acceleration is defined [13]:

$$a = \dot{v} T + \kappa v^2 N \quad (7.1)$$

Where:

a = Total acceleration of vehicle (m/s^2)

v = Tangential velocity of vehicle (m/s)

κ = Curvature at an instantaneous point (m^{-1})

N = Normal unit vector

T = Tangential unit vector

In addition, where the road tangent angle θ of a curve with curvature $\kappa(s)$ is defined as the deviation of the Serret-Frenet frame from a vehicle reference:

$$\theta = f[\kappa(s)] \quad (7.2)$$

By construction, the acceleration vector cannot contain a component in the binormal direction. This construction is valid, however, only in a planar curve assumption [13][14]. To extend this formulation into a three-dimensional motion, this paper proposes an orientation reference for the two-dimensional Serret-Frenet triad, such that the triad is updated with a new orientation vector that depends on empirical data. To illustrate this methodology, a variant geometry curved road, shown in Figure 7.1, is used. The road is composed of multiple superelevated segments with both downhill and uphill vertical slopes. For this case, the super elevation e per section is noted with different colors in Figure 7.1.

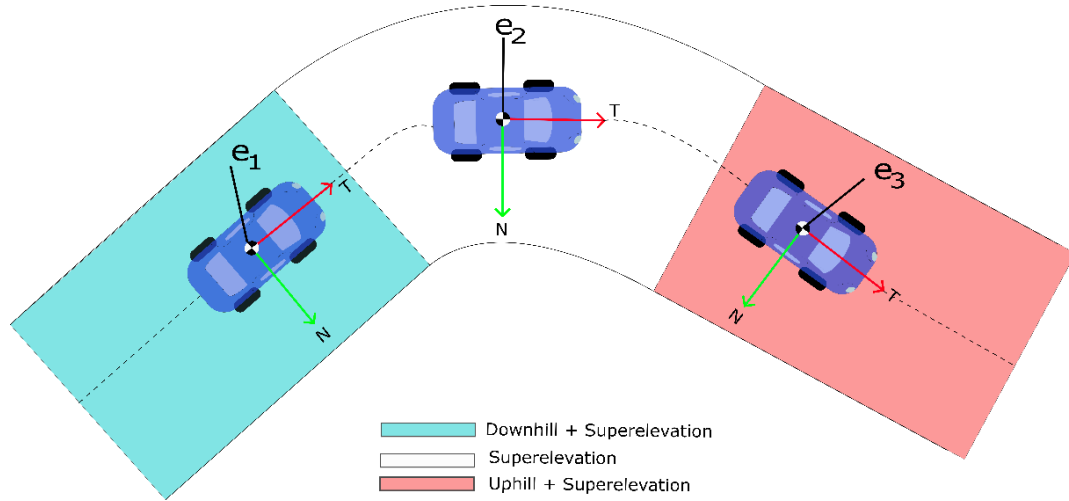


Figure 7.1 Variant Geometry Curved Road Example

The change in elevation affects the two-dimensional Serret-Frenet triad by applying rotational transformations defined by the orientations yaw (β_1), pitch (β_2), and roll (β_3) angles:

$$R = R_B(\beta_1)R_N(\beta_2)R_T(\beta_3)$$

$$R(\beta_k) = \begin{bmatrix} \cos(\beta_1) & -\sin(\beta_1) & 0 \\ \sin(\beta_1) & \cos(\beta_1) & 0 \\ 0 & 0 & 1 \end{bmatrix} \begin{bmatrix} \cos(\beta_2) & 0 & \sin(\beta_2) \\ 0 & 1 & 0 \\ -\sin(\beta_2) & 0 & \cos(\beta_2) \end{bmatrix} \begin{bmatrix} 1 & 0 & 0 \\ 0 & \cos(\beta_3) & -\sin(\beta_3) \\ 0 & \sin(\beta_3) & \cos(\beta_3) \end{bmatrix}$$

When applied to the Serret-Frenet Triad, the result is:

$$\begin{bmatrix} T' \\ N' \\ B' \end{bmatrix} = R(\beta_k) \begin{bmatrix} T \\ N \\ B \end{bmatrix}$$

Where a prime denotes a rotated frame. To upgrade the previous MVRC road data to a three-dimensional reference, a vehicle data recording is needed such that a vehicle can navigate a road segment while measuring its Euler Angles. The angles are used to find an appropriate transformation matrix $R(\beta_k(s_i))$ at incremental road segments. The transformation matrix is post-processed such that an analytical smooth matrix corresponds to the appropriate 3D rotation per segment length s_i :

$$\begin{bmatrix} T(s_{i+1}) \\ N(s_{i+1}) \\ B(s_{i+1}) \end{bmatrix} = R(\beta_k(s_i)) \begin{bmatrix} T(s_i) \\ N(s_i) \\ B(s_i) \end{bmatrix} \quad (7.3)$$

Where:

$$\beta_1(s_{i+1}) = \text{Yaw Rotation at segment length } s_{i+1}$$

$$\beta_2(s_{i+1}) = \text{Pitch Rotation at segment length } s_{i+1}$$

$$\beta_3(s_{i+1}) = \text{Roll Rotation at segment length } s_{i+1}$$

Assuming typical suspension characteristics and quasi-static driver behavior and alignment, vehicles will experience similar Euler Angle changes for a given road segment

such that measuring, post-processing, and storing the Euler Angles of a vehicle will provide a reliable reference for CAVs on curves.

In two dimensions, only parameters to have a pre-determined reference centerline trajectory independent of visual sensors were provided. From previous studies, the reference trajectory is formulated with the road tangent angle denoted in (7.2) [15]. In the current proposed method, a three-dimensional reference system for autonomous vehicles can be contained as a combination of curvature, heading angle, and a rotation matrix per segment length. An augmented data matrix for CAVs to store would follow:

$$ID = [P_{1i}, P_{2i}, s_i, \kappa_i, \theta_i, \beta_i]$$

Where:

ID = Road segment identification

P_{1i} = Latitudinal Coordinate

P_{2i} = Longitudinal Coordinate

s_i = Segment length (m)

κ_i = Curvature at segment length (m^{-1})

θ_i = Road tangent angle (degrees)

β_i = Transformation Angles (degrees)

7.2.1 Empirical State Estimation Considerations

Augmenting the current MVRC reference requires vehicle-dependent and vehicle-independent road grade profiles. Vehicle-independent road grades were obtained from elevation traces, as it has been shown that high accuracy elevation data is available for

various transportation applications [16]. A Piecewise-Linear Least Squares (PLLS) fit with a smoothed quadratic fit was used to approximate the road grade profiles.

Vehicle-dependent road grades were obtained by recording vehicle yaw/pitch/roll rate angles during a section curve. In this paper, an Extended Kalman Filter was used on sensor recordings. In brief, Kalman Filters approximate the best estimation of a measurement by considering the statistical characteristics of the sensor observations and surrounding noise. For a more detailed explanation, the reader is referred to additional resources on the topic [17][18][19][20].

Vehicle data was post-processed to obtain an analytical formulation of the road grade per segment length. Numerical quadratures were used to obtain vehicle's angular displacements. Numerical drift was subtracted from the integrated angular displacements, and the resulting roll/pitch/yaw measurements were identified and discretized. Spline interpolation and Linear Least Squares (LLS) method were performed to generate the road grade mathematical profiles to reduce the amount of data needed to represent the path.

In the LLS case, a $m \times 6$ Vandermonde matrix $A_{i,j}$ was used to formulate a cubic fit [21]. A quintic fit was selected for robustness and differentiability in the analytical reference, as it is expected for road grade to have smooth elevation changes. The LLS system is described below by the minimization of the residual norm $\|r\|_2$ given by:

$$r = A_{i,j}x_i - b_j = \begin{bmatrix} 1 & t_1 & t_1^2 & t_1^3 & t_1^4 & t_1^5 \\ 1 & t_2 & t_2^2 & t_2^3 & t_2^4 & t_2^5 \\ \vdots & \vdots & \vdots & \vdots & \vdots & \vdots \\ 1 & t_m & t_m^2 & t_m^3 & t_m^4 & t_m^5 \end{bmatrix} \begin{bmatrix} x_1 \\ x_2 \\ x_3 \\ x_4 \\ x_5 \\ x_6 \end{bmatrix} - \begin{bmatrix} b_1 \\ b_2 \\ \vdots \\ b_m \end{bmatrix} \quad (7.4)$$

Where:

x_i = Variables of quintic fit from given measurements with $i \in [1,6]$

t_j = Time measurements with $j \in [1, m]$

b_j = Road grade measurements with $j \in [1, m]$

Finally, data is compared between the extracted geodetic road, and the on-board vehicle data to evaluate the accuracy of the method.

7.3 Experimental Setup

This section evaluates the geodetic road grades and vehicle road grade readings. Since geodetic data only provided estimates for road “pitch” measurement, analysis will be limited to this measurement. Shortly, the test consisted of extracting geodetic data for a road with the Google Earth tool, and of obtaining on-board angular rate data from multiple vehicles for the same road.

7.3.1 Test Setup and Equipment

The road for grade testing comes from a variable-elevation road located at Salt Creek Roadway in Lincoln, Nebraska (USA). A satellite view of the extracted geodetic road is shown on Figure 7.2. Each vehicle was driven at an approximately constant velocity of 20 m/s and the data of interest is limited to about 400 m from the starting point, for a total length of approximately 1 km. This range was determined based on the stability of the vehicle to reach a constant velocity, the quality of the elevation data, and on the section of the road in which no major yaw change was present.



Figure 7.2 Road for Grade Testing

Three vehicles were used to record data in two trips each, with the following order: a 2019 Nissan Sentra, a 2014 Nissan Altima, and a 2013 Hyundai Sonata as shown in Figure 7.3. Their specifications such as weight and center of gravity (c.g.) location are found in Table 7.1.



Figure 7.3 Testing Vehicles: Nissan Sentra (left), Nissan Altima (middle), and Hyundai Elantra (right)

Table 7.1 Specifications of Testing Vehicles [22][23]

	Year	Tire Specification	Weight (kg)	Lateral (mm)	Longitudinal (mm)	Height (mm)
Nissan Sentra	2007	P205/55R16 89H	1711	-17.8	1192.8	556.8
Nissan Altima	2008	P215/60R16 94T	1968	-9	1301.9	544.1
Hyundai i Elantra	2007	P195/65R15 89T	1681	-19.6	1171.4	546.6

For data recording, a LSM6DSM-iNEMO inertial module, typically found in smartphones, with a recording rate of 417 Hz was used [24]. In this test, the recording device was attached by placing the smartphone with a Velcro mounting as close to the c.g. as possible as shown in Figure 7.4. Sample results of the angular rates for the first trial of the Sentra vehicle are shown in Figure 7.5 below.



Figure 7.4 Sensor Velcro Mounting on Vehicle

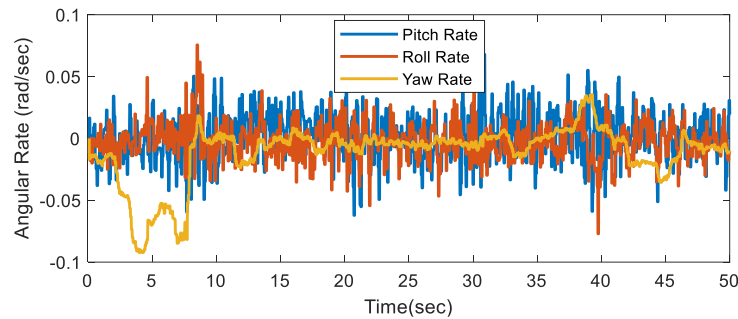


Figure 7.5 Sample Angular Rate Readings for Nissan Sentra Trial 1

7.4 Post-Processing Results and Analysis

This section will elaborate on the post-processing techniques on the data from section 7.3. The method will be showcased for the data from the Sentra’s first trial, but the same method was used for all datasets. Full results for the 6 tests are available for download and review at Mendeley Data [25]. The angular rates from the vehicle were numerically integrated as shown in Figure 7.6. The resulting yaw shows a turning motion from the first 10 seconds that was excluded from the further analysis. Pitch was selected for further analysis as shown in Figure 7.7. It is noted that a sensor-drift phenomenon is present as pitch accumulates with time [26][27]. To remove this effect, the average pitch rate was integrated and denoted as Drift-Integrated on Figure 7.7. This drift-integrated correction

was then subtracted from the recorded pitch resulting in the Drift-Subtracted data. The Drift-Subtracted pitch was plotted along with the extracted elevation profile on Figure 7.8 to exemplify the change of vehicle motion. Pitch's time data was spatially mapped based on vehicle trajectory for comparative purposes. In unidirectional curves, Euler angle's pitch is equal to the elevation slope. Thus, pitch changes can be correlated to the instantaneous (effective) slope of the roadway. However, the pitch measured is affected by factors such as: elevation difference between front and rear wheels, suspension difference between front-and-rear mounting locations of sprung mass, rake (resting) pitch of vehicle, usually for aerodynamic purposes.

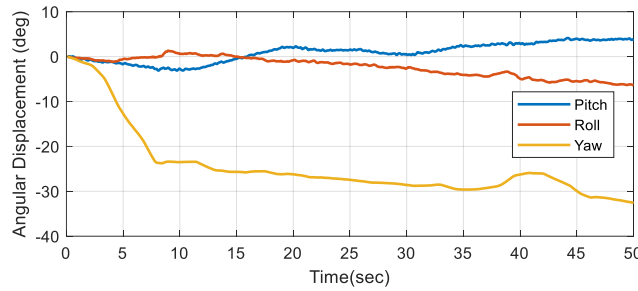


Figure 7.6 Numerically Integrated Angular Rates for Sentra-1

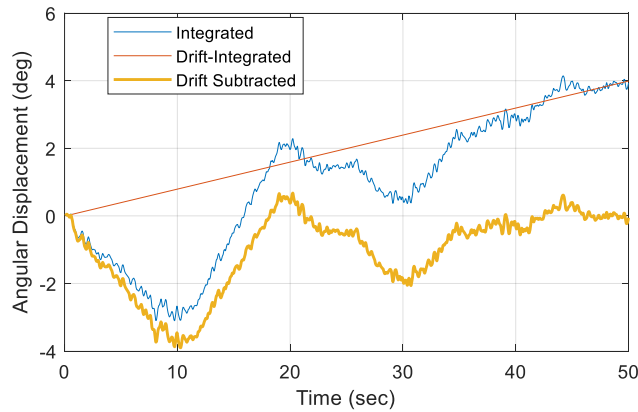


Figure 7.7 Numerical Drift Subtraction for Pitch in Sentra-1

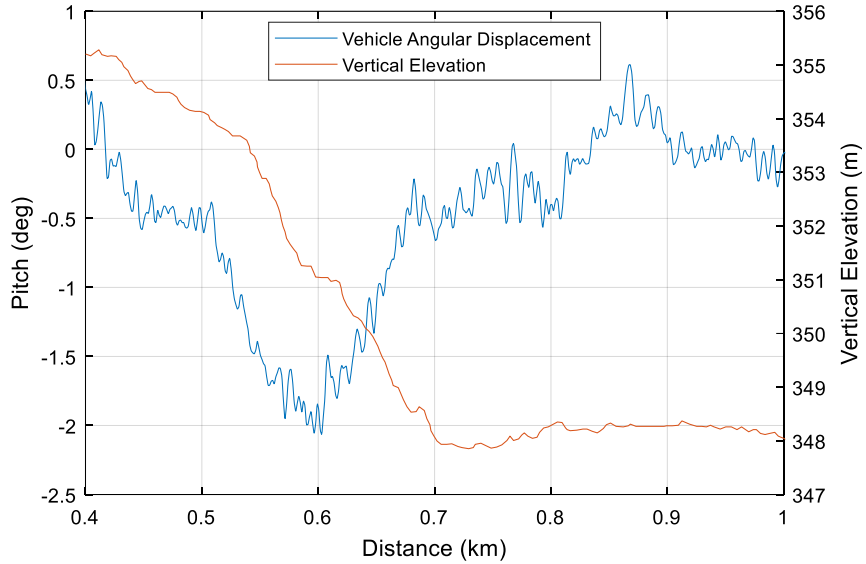


Figure 7.8 Sentra-1 Vehicle Pitch and Vertical Elevation Profile

Resulting vehicle angular displacement was fitted with both a quintic fit, and a spline interpolation for evaluation as shown in Figure 7.9 below. Quintic LLS was chosen since it is primarily used in trajectory generation on longitudinal control. However, for this elevation analysis, the quintic fit lacks substantial correlation with any of the other plots, and thus was excluded from further analysis.

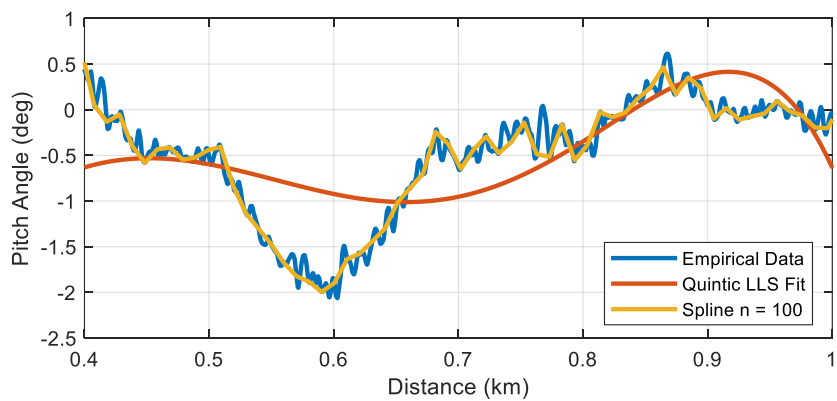


Figure 7.9 Empirical Vehicle Data Results for Sentra-1

Subsequently, road grade was calculated from vertical elevations. The estimated road grade from geodetic and a robust local regression using weighted LLS and a second-degree polynomial model is used to smooth the data as shown in Figure 7.10. Noise is visually reduced, but a correlation study was conducted to see how the smoothed geodetic road compared to the vehicle spline fitting the empirical data.

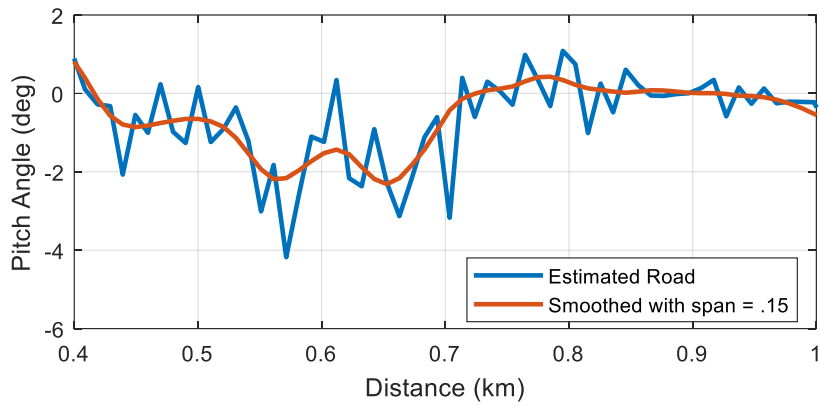


Figure 7.10 Estimated Road Grade from Geodetic Road Data Results

For all vehicle trials, the smoothed geodetic road profile and vehicle splined data were compared through an error analysis tabulated in Table 7.2, and both road grade profiles are graphed on Figure 7.11 for all six tests. Important remarks include a considerably low (< 0.1) Root-Mean Square Error (RSME) and normalized RSME for all trials consistently. Low RSME indicates a good level of fit in between of the empirical vehicle data and the extracted geodetic model. Some of the error is partially attributed to the low-resolution (~100 m) of the geodetic data, and to the intrinsic difference of pitch angle that a vehicle encounters when adjusting from an incline to a flat surface (e.g., vehicle wheelbase limits the shared pitch angle a vehicle experience with respect to the road). Furthermore, residual averages for all six trial, are consistently close to zero, indicating another signal of good fit for the data. A histogram for residual frequency is attached in the Appendix A.7 for further

indication on the normality of the residual data. Finally, coefficient of determination R^2 and adjusted R^2 were calculated and tabulated as well on Table 7.2. Results indicate that about 63% of the variance of the dependent variables is related to the independent variables. The choice of R^2 as a statistic metric was deemed as appropriate since the geodetic model is not constructed to make predictions about the road pitch, but as a substitute to obtain vehicle pitch data.

The residual plots are shown in the Appendix A.6 as well to determine if residuals are consistent with random error. As it was mentioned earlier, as the vehicle changed from an incline to a flat road surface, error was introduced in the data that is not attributed to stochastic factors. As such, all trials exhibit the same residual peak at around 650 m, which reflects the transition of the vehicle. Thus, considering this limitation on the model is essential for implementation. In general, for all trials, results indicate that any vehicle within considerable size metrics, can give a reasonable estimate of effective vehicle pitch from geodetic data.

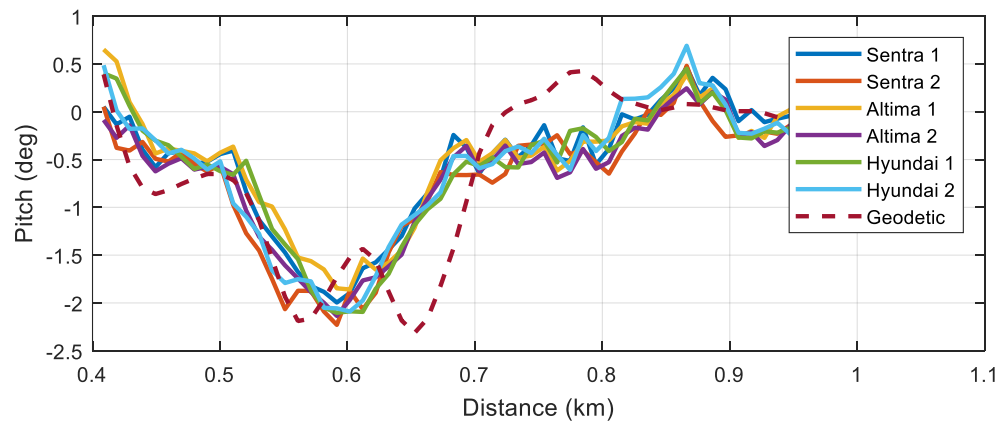


Figure 7.11 Vehicle Empirical Data and Extracted Geodetic Data for all Vehicle Trials

Table 7.2 Error Table for Pitch Results

Vehicle and Trial	Sentra-1	Sentra-2	Altima-1	Altima-2	Elantra-1	Elantra-2
Residual Mean	0.1096	-0.0459	0.1266	-0.0292	0.0355	0.0286
Residual Standard Deviation	0.4025	0.3614	0.3924	0.2968	0.2889	0.3573
RSME	0.0633	0.0640	0.0672	0.0605	0.0617	0.0627
Normalized RSME	0.0370	0.0423	0.0382	0.0496	0.0472	0.0413
R ² Value	0.6560	0.6310	0.6220	0.6350	0.6600	0.6500
Adjusted R ² Value	0.6500	0.6250	0.6150	0.6280	0.6540	0.6440

7.5 Conclusions and Recommendations

In this paper, a three-dimensional augmentation of the previous MVRC was proposed. This augmentation consisted of a mathematical development that used OBU measurements to estimate vehicle general orientation per segment road. The data was compared to a geodetic extracted profile and yielded a high degree of fit. Different fitting methods to interpret the geodetic data are still yet to be tested, along with the correlation exhibited with the vehicle data. Conclusions of this study show promising avenue of obtaining vehicle pitch angles without the necessity of empirical vehicle experimentation. Also, complementary vehicle recordings pose an alternative measurement for road grade when geodetic profiles are limited; often occurring in bridges or highway constructions with multi-grade levels. Subsisting with the MVRC, appropriate implementation of the data studied could improve considerably road references for CAVs.

7.6 References

- [1] Jacome R. O., Stolle, C., Faller, R. K., Grispos, G., “A Dynamically-Concise Roadmap Framework for Guiding Connected and Automated Vehicles” IFIP/IEEE IM 2021 - 4th International Workshop on Intelligent Transportation and

Autonomous Vehicles Technologies. Bordeaux, France, 2021, Manuscript Accepted for Publication

- [2] USDOT. (2020, June 30). USDOT Intelligent Transportation Systems Office - Connected Vehicle Pilot Deployment Program. Retrieved from <https://www.its.dot.gov/pilots/index.htm>
- [3] Chang, J. (2017). An Overview of USDOT Connected Vehicle Roadside Unit Research Activities. U.S DOT. Washington D.C.: Federal Highway Administration Intelligent Transportation Systems (ITS) Joint Program Office.
- [4] VDOT. (2018). Smarter Roads VDOT. Retrieved 2020, from <https://smarterroads.org/login>
- [5] WYDOT. (2020, May 16). WYDOT Connected Vehicle Pilot Program. Retrieved from <https://wydotcvp.wyoroad.info/>
- [6] AASHTO. (2011). A Policy on Geometric Design of Highways and Streets (The Green Book) (Sixth Edition ed.). Washington D.C.: American Association of State Highway and Transportation Officials.
- [7] Tsai, Y., & Ai, C. (2017). Automated Superelevation Measurement Method Using a Low-Cost Mobile Device: An Efficient, Cost-Effective Approach Toward Intelligent Horizontal Curve Safety Assessment. *Transportation Research Record: Journal of the Transportation Research Board*, 2621(1), 62-70. doi:10.3141/2621-08
- [8] Malartre, F., Feraud, T., Debain, C., & Chapuis, R. (2009). Digital Elevation Map Estimation by Vision-Lidar fusion. *IEEE International Conference on Robotics and Biomimetics (ROBIO)*. doi:10.1109/ROBIO.2009.5420701

- [9] McIntyre M. L., Ghotikar T. J., Vahidi A., Song X. and Dawson D. M., "A Two-Stage Lyapunov-Based Estimator for Estimation of Vehicle Mass and Road Grade," IEEE Transactions on Vehicular Technology, pp. 3177-3185, 2009, doi:10.1109/TVT.2009.2014385
- [10] Tseng H. E., Xu L. and Hrovat D., "Estimation of Land Vehicle Roll and Pitch Angles," Vehicle System Dynamics, vol. 45, no. 5, pp. 433-443, 2007.
- [11] Bae H. S., Ryu J. and Gerdes J. C., "Road Grade and Vehicle Parameter Estimation for Longitudinal Control Using GPS," in IEEE Conference on Intelligent Transportation Systems, 2001.
- [12] Kidambi, N., Harne, R. L., Fujii, Y., Pietron, G. M., & Wang, K. W. (2014). Methods in Vehicle Mass and Road Grade Estimation. SAE Int. J. Passeng. Cars - Mech. Syst., 7(3). doi:10.4271/2014-01-0111
- [13] Meriam, J. L., & Kraige, L. G. (2002). Engineering Mechanics, Dynamics. Wiley, John & Sons, Incorporated.
- [14] Kreyszig, E. (1991). Differential Geometry (1st ed.). Dover Publications.
- [15] Jacome, R., Stolle, C., & Sweigard, M. (2020). Road Curvature Decomposition for Autonomous Guidance. SAE Technical Paper 2020-01-1024. doi:10.4271/2020-01-1024
- [16] Wang, Y., Zou, Y., Henrickson, K., Tang, J., Wang, Y., & Park, B.-J. (2017, April). GE elevation data extraction and accuracy assessment for transportation applications. PLoS ONE, 12(4:e0175756). doi:10.1371/journal.pone.0175756

- [17] Rhudy, M. B., Salguero, R. A., & Holappa, K. (2017, February). A Kalman Filtering Tutorial For Undergraduate Students. International Journal of Computer Science & Engineering Survey (IJCSES), 8(1). doi:10.5121/ijcses.2017.8101
- [18] Abbeel, P., Coates, A., Montemerlo, M., Ng, A. Y., & Thrun, S. (2005, June 8-11). Discriminative Training of Kalman Filters. Robotics: Science and Systems I. doi:10.15607/RSS.2005.I.038
- [19] Shan, S., Hou, Z., & Wu, J. (2017). Linear Kalman Filter for Attitude Estimation from Angular Rate and a Single Vector Measurement. Hindawi Journal of Sensors, 9. doi:10.1155/2017/9560108
- [20] Simon, D. (2006). Optimal State Estimation: Kalman, H Infinity, and Nonlinear Approaches. Wiley-Interscience.
- [21] Heath, M. T. (2018). Scientific Computing: An Introductory Survey. SIAM.
- [22] Bixel, R., Heydinger, G., & Guenther, D. (2010). Measured Vehicle Center-of-Gravity Locations - Including NHTSA's Data Through 2008 NCAP. SAE Technical Paper 2010-01-0086. doi:10.4271/2010-01-0086
- [23] Heydinger, G., Bixel, R., Garrott, W., Pyne, M., Gavin, J., & Guenther, D. A. (1999). Measured Vehicle Inertial Parameters-NHTSA's Data Through November 1998. SAE Technical Paper 1999-01-1336, 26. doi:10.4271/1999-01-1336
- [24] iNEMO inertial module: always-on 3D accelerometer and 3D gyroscope
- [25] Jacome, R. (2021). Road Empirical Data for Elevation Estimations. Mendeley Data, V1. doi:10.17632/d586x5kbnd.1

- [26] Li, S., Gao, Y., Meng, G., Wang, G., & Guan, L. (2019, May). Accelerometer-Based Gyroscope Drift Compensation Approach in a Dual-Axial Stabilization Platform. *Electronics*, 8(5), 594. doi:10.3390/electronics8050594
- [27] Rockwood, M., Wallace, B., Goubran, R., Knoefel, F., & Marshall, S. (2015). Adaptive drift calibration of accelerometers with direct velocity measurements. IEEE. doi:10.1109/I2MTC.2015.7151272

CHAPTER 8. SUMMARY/CONCLUSIONS

8.1 Summary

A review of the state-of-the-art technologies in current CAVs and digital maps were explored. After identifying their shared characteristics and vulnerabilities, a new approach denoted as the MVRC was proposed. The proposed solution primarily solves the problem where CAVs cannot rely on light-based sensor data to navigate (e.g., harsh weather), but still uses wireless communications for map data transmissions. It is based on the combination of principles found in current design practices, differential geometry, and vehicle dynamics. This research investigation presented the foundation and development for the MVRC roadmap which uses dynamic vehicle data as a guidance reference for CAVs. The mathematical foundation for the roadmap system, along with augmentations for extra parameters, and three-dimensional considerations were explored.

8.2 Key Findings

The following is a list of key findings and contributions obtained throughout this investigation:

- Current vulnerabilities on the state-of-the-art systems were identified, and the MVRC was proposed based on them. Offering a roadmap of dynamic data for vehicles.
- Formulation of equations (3.33) - (3.35) proved the analytical form of acceleration when the plane curve assumption is not applied. Thus, generalizing the case of current acceleration formulations for 3D space curves.

- Methods for extracting road curvature from digital maps were discussed and a method based on pure geometry was proposed.
- Roads can be classified from their curvature profiles into either straight or curved for multi-scale classification.
- Mathematical curvature profiles can be created based on the type of street design for the road (i.e., classifying as spiral, simple, compound, reverse curves). Thus, diminishing the data used for storing, by implementing simpler mathematical models instead of high-density data.
- Based on the curvature profile, a maximum allowable safe speed can be calculated for the road. Thus, providing an adjustable (e.g., weather dependent) speed recommendation for CAVs. This data is used as part of the MVRC data map.
- Proposed solution solves a crucial problem by not having precise starting-stopping points for large-scale implementation. Noting that methods discussed in Chapter 1 suffer from a lack of large-scale uses because of their local limitations.
- Physical testing procedures can be applied to capture superelevation and road grade changes. Probe vehicle data showed good correlation on road grade determination for augmenting the MVRC data map.

8.3 Recommendations/Future Work

Future work involves testing and evaluation of the proposed roadmap reference for full-vehicle cases. Suggested testing will involve developing a testing track that is

composed of three main types of maneuvering: straight-line, simple curve, and spiral curve. The testing track is to be painted with road marking paint, and the GPS coordinates of the marking paint is to be pre-recorded with high level accuracy (< 2.50 cm) before testing. The paint is representative of a road centerline for a vehicle on the road. Using the GPS data points obtained, the curvature profile and dynamic attributes will be extracted, processed as per the methodology constructed in this dissertation, and stored for testing use.

Two different maneuvering techniques are recommended to be tested: a human driver, and the MVRC data guided. The MVRC approach must be used in conjunction with a vehicle on-board controller. The controller must use lateral and longitudinal control based on its steering and braking/throttle respectively. The vehicle system (man and unmanned) needs a data acquisition system for collection of GPS coordinates, steering wheel angle, acceleration, and velocity. To ensure high-accuracy and test the latency of wireless systems, a Real Time Kinematic (RTK) system is recommended. RTK can use wireless transmissions, such that the vehicle can receive and transmit data with a stationary rover holding the MVRC data.

Evaluation is performed after completing the tests for the two maneuvering techniques. Results between the manned and unmanned test are compared to (1) against each other and (2) against the high-accuracy road centerline coordinates collected pre-test. Comparison of steering wheel angle, GPS coordinates, and acceleration will be determinant factors on the accuracy of the MVRC method for future implementation. Furthermore, multiple discretization levels can be used on the MVRC method to see the controller

performance under low and high levels of discretization. Since the data is used at considerably different speed levels (e.g., 25 m/s – 38 m/s), multiple discretization levels (e.g., 1 point per 100 m) need to be explored as well to determine a robustness level on the system.

A final remark for implementation of the MVRC data, is to apply other classification methods for road types based on curvature data. This investigation showed some examples and uses for the curvature model, but an avenue that was not explored includes: Machine learning techniques and Neural Networks for classifying high-density number of roads. Supervised learning methods can be appropriate for classifying roads, given that there is data available along with proper name attributes.

8.4 Conclusions

The proposed research effort conducted at UNL, offers a backup system that is foundational to solve a paradigm in autonomous vehicle research, how to navigate on roads without light-based sensors. Project partnership for long-term implementation may potentially reduce CAV crashes where sensor reliability is low (e.g., winter weather). Potential partnerships include: Ontario Good Roads Association, Virginia DOT, and the Municipal Alliance for Connected and Automated Vehicles in Ontario.

Appendix

A.1 Formulation Chapter 3: Acceleration in Canonical Form

Recalling the canonical representation of a curve from Chapter 3:

$$x(s) = \left(s - \frac{\kappa^2 s^3}{6} \right) \mathbf{T} + \left(\frac{s^2}{2} \kappa + \frac{d\kappa}{ds} \frac{s^3}{6} \right) \mathbf{N} + \left(\frac{\kappa \tau s^3}{6} \right) \mathbf{B} + o(s^3)$$

$$x_1(s) = s - \frac{\kappa^2}{6} s^3 + o(s^3)$$

$$x_2(s) = \frac{\kappa}{2} s^2 + \frac{d\kappa}{ds} \frac{1}{6} s^3 + o(s^3)$$

$$x_3(s) = \frac{\kappa \tau}{6} s^3 + o(s^3)$$

Assuming first order terms, the following representation is found:

$$\phi = s\mathbf{T} + \left(\frac{\kappa}{2} s^2 \right) \mathbf{N} + \left(\frac{\kappa \tau}{6} s^3 \right) \mathbf{B}$$

It is now desired to find:

$$\frac{d^2\phi}{dt^2} = \frac{d^2}{dt^2} (x_1(s) + x_2(s) + x_3(s)) = \frac{d^2}{dt^2} (s\mathbf{T}) + \frac{d^2}{dt^2} \left(\frac{\kappa}{2} s^2 \mathbf{N} \right) + \frac{d^2}{dt^2} \left(\frac{\kappa \tau}{6} s^3 \mathbf{B} \right)$$

At this point forward, bolding will be omitted to ease writing, and denoting that T, N, and B will be unit vectors. To ease the derivatives, the terms will be done separately:

First Term

$$\frac{d^2}{dt^2} (sT) = \frac{d}{dt} \left(\frac{ds}{dt} T + s \frac{dT}{dt} \right)$$

$$\frac{d^2}{dt^2}(sT) = \frac{d}{dt} \left(\frac{ds}{dt} T + s \frac{dT}{dt} \right) = \left(\frac{d^2s}{dt^2} T + \frac{ds}{dt} \frac{dT}{dt} + \frac{ds}{dt} \frac{dT}{dt} + s \frac{d^2T}{dt^2} \right)$$

$$\frac{d^2}{dt^2}(sT) = \left(\ddot{s} T + 2\dot{s} \frac{dT}{dt} + s \frac{d^2T}{dt^2} \right) = \left(\ddot{s} T + 2\dot{s} \frac{dT}{ds} \frac{ds}{dt} + s \frac{d^2T}{ds^2} \frac{d^2s}{dt^2} \right)$$

$$\left(\ddot{s} T + 2\dot{s}^2 \frac{dT}{ds} + s\ddot{s} \frac{d^2T}{ds^2} \right) = \left(\ddot{s} T + 2\dot{s}^2 \kappa N + s\ddot{s} \frac{d}{ds}(\kappa N) \right)$$

$$= (\ddot{s} T + 2\dot{s}^2 \kappa N + s\ddot{s}\kappa(-\kappa T + \tau B)) =$$

First Term: $\frac{d^2}{dt^2}(sT) = ((1 - s\ddot{s}\kappa^2)\ddot{s}T + 2\dot{s}^2 \kappa N + \tau B)$

Second Term

$$\begin{aligned} \frac{d^2}{dt^2} \left(\frac{\kappa}{2} s^2 N \right) &= \frac{d}{dt} \left(\frac{\dot{\kappa}}{2} s^2 N + \kappa s \dot{s} N + \frac{\kappa}{2} s^2 \frac{dN}{dt} \right) \\ &= \frac{d}{dt} \left(\frac{\dot{\kappa}}{2} s^2 N + \kappa s \dot{s} N + \frac{\kappa}{2} s^2 (-\kappa T + \tau B) \right) \\ &= \frac{d}{dt} \left(\frac{\dot{\kappa}}{2} s^2 N + \kappa s \dot{s} N - \frac{\kappa^2}{2} s^2 T + \frac{\kappa}{2} s^2 \tau B \right) \end{aligned}$$

This will require taking the four terms separately

$$\frac{d^2}{dt^2} \left(\frac{\kappa}{2} s^2 N \right) = [1] + [2] + [3] + [4]$$

$$[1] \quad \frac{d}{dt} \left(\frac{\dot{\kappa}}{2} s^2 N \right) = \left(\frac{\ddot{\kappa}}{2} s^2 N + \dot{\kappa} s \dot{s} N + \frac{\dot{\kappa}}{2} s^2 \frac{dN}{dt} \right) = \left(\frac{\ddot{\kappa}}{2} s^2 N + \dot{\kappa} s \dot{s} N + \frac{\dot{\kappa}}{2} s^2 \frac{dN}{ds} \frac{ds}{dt} \right) \rightarrow$$

$$\left(\frac{\ddot{\kappa}}{2} s^2 N + \dot{\kappa} s \dot{s} N + \frac{\dot{\kappa}}{2} s^2 \dot{s} (-\kappa T + \tau B) \right) = \left(\frac{\ddot{\kappa}}{2} s^2 N + \dot{\kappa} s \dot{s} N - \frac{\dot{\kappa}}{2} s^2 \dot{s} \kappa T + \frac{\dot{\kappa}}{2} s^2 \dot{s} \tau B \right)$$

$$[1] \quad \frac{d}{dt} \left(\frac{\kappa}{2} s^2 N \right) = \left(-\frac{\dot{\kappa}}{2} s^2 \dot{s} \kappa T + \left(\frac{\dot{\kappa}}{2} s + \dot{\kappa} s \right) s N + \frac{\dot{\kappa}}{2} s^2 \dot{s} \tau B \right)$$

$$[2] \quad \frac{d}{dt}(\kappa s \dot{s} N) = \left(\dot{\kappa} s \dot{s} N + \kappa \dot{s}^2 N + \kappa s \ddot{s} N + \kappa s \dot{s} \frac{dN}{dt} \right)$$

$$= \left(\dot{\kappa} s \dot{s} N + \kappa \dot{s}^2 N + \kappa s \ddot{s} N + \kappa s \dot{s} \frac{dN}{ds} \frac{ds}{dt} \right) \rightarrow$$

$$(\dot{\kappa} s \dot{s} N + \kappa \dot{s}^2 N + \kappa s \ddot{s} N + \kappa s \dot{s}^2 (-\kappa T + \tau B)) \rightarrow$$

$$[2] \quad \frac{d}{dt}(\kappa s \dot{s} N) = (-s \dot{s}^2 \kappa^2 T + (\dot{\kappa} s \dot{s} + \kappa \dot{s}^2 + \kappa s \ddot{s}) N + \kappa s \dot{s}^2 \tau B)$$

$$[3] \quad \frac{d}{dt} \left(-\frac{\kappa^2}{2} s^2 T \right) = - \left(\frac{\dot{\kappa}}{2} s^2 T + \kappa s \dot{s} T + \frac{\kappa^2}{2} s^2 \frac{dT}{dt} \right)$$

$$= - \left(\frac{\dot{\kappa}}{2} s^2 T + \kappa s \dot{s} T + \frac{\kappa^2}{2} s^2 \frac{dT}{ds} \frac{ds}{dt} \right)$$

$$- \left(\frac{\dot{\kappa}}{2} s^2 T + \kappa s \dot{s} T + \frac{\kappa^3}{2} s^2 \dot{s} N \right)$$

$$[3] \quad \frac{d}{dt} \left(-\frac{\kappa^2}{2} s^2 T \right) = - \left(\left(\frac{\dot{\kappa}}{2} s + \kappa \dot{s} \right) s T + \frac{\kappa^3}{2} s^2 \dot{s} N \right)$$

$$[4] \quad \frac{d}{dt} \left(\frac{\kappa}{2} s^2 \tau B \right) = \left(\frac{\dot{\kappa}}{2} s^2 \tau B + \kappa \dot{s} s \tau B + \frac{\kappa}{2} s^2 \dot{\tau} B + \frac{\kappa}{2} s^2 \tau \frac{dB}{dt} \right)$$

$$= \left(\frac{\dot{\kappa}}{2} s^2 \tau B + \kappa \dot{s} s \tau B + \frac{\kappa}{2} s^2 \dot{\tau} B + \frac{\kappa}{2} s^2 \tau \frac{dB}{ds} \frac{ds}{dt} \right)$$

$$= \left(\left(\frac{\dot{\kappa}}{2} s^2 \tau + \kappa \dot{s} s \tau + \frac{\kappa}{2} s^2 \dot{\tau} \right) B + \frac{\kappa}{2} s^2 \tau \dot{s} (-\tau N) \right)$$

$$[4] \quad \frac{d}{dt} \left(\frac{\kappa}{2} s^2 \tau B \right) = \left(\left(\frac{\dot{\kappa}}{2} s^2 \tau + \kappa \dot{s} s \tau + \frac{\kappa}{2} s^2 \dot{\tau} \right) B - \frac{\kappa}{2} s^2 \tau^2 \dot{s} N \right)$$

Combining all four terms:

$$\frac{d^2}{dt^2} \left(\frac{\kappa}{2} s^2 N \right) = [1] + [2] + [3] + [4]$$

$$\begin{aligned}
\text{Second Term: } & \left(-\frac{\ddot{\kappa}}{2}s^2\dot{s}\kappa T + \left(\frac{\ddot{\kappa}}{2}s + \dot{\kappa}\dot{s} \right) sN + \frac{\ddot{\kappa}}{2}s^2\dot{s}\tau B \right) \\
& + (-s\dot{s}^2\kappa^2T + (\dot{\kappa}s\dot{s} + \kappa\dot{s}^2 + \kappa s\ddot{s})N + \kappa s\dot{s}^2\tau B) \\
& - \left(\left(\frac{\dot{\kappa}}{2}s + \kappa\dot{s} \right) sT + \frac{\kappa^3}{2}s^2\dot{s}N \right) \\
& + \left(\left(\frac{\dot{\kappa}}{2}s^2\tau + \kappa\dot{s}\tau + \frac{\kappa}{2}s^2\dot{t} \right) B - \frac{\kappa}{2}s^2\tau^2\dot{s}N \right)
\end{aligned}$$

Simplifying:

$$\begin{aligned}
\text{Second Term: } & \frac{d^2}{dt^2} \left(\frac{\kappa}{2}s^2N \right) \\
= & \left(\left((\ddot{\kappa}\dot{s}\kappa + \dot{\kappa}) \left(-\frac{1}{2}s^2 \right) + (\dot{s}^2\kappa^2 + \kappa\dot{s})(-s) \right) T \right. \\
& + \left. \left((\ddot{\kappa} - \kappa^3\dot{s} - \kappa\tau^2\dot{s}) \frac{1}{2}s^2 + 2s\dot{\kappa}\dot{s} + \kappa\dot{s}^2 + \kappa s\ddot{s} \right) N \right. \\
& \left. + \left(\left(\frac{\ddot{\kappa}}{2}s\dot{s} + \kappa\dot{s}^2 + \frac{\dot{\kappa}}{2}s + \kappa\dot{s} \right) s\tau + \frac{\kappa}{2}s^2\dot{t} \right) B \right)
\end{aligned}$$

Third Term

$$\begin{aligned}
\frac{d^2}{dt^2} \left(\frac{\kappa\tau}{6}s^3B \right) & = \frac{d}{dt} \left(\frac{\dot{\kappa}\tau}{6}s^3B + \frac{\kappa\dot{\tau}}{6}s^3B + \frac{\kappa\tau}{6}3s^2\dot{s}B + \frac{\kappa\tau}{6}s^3 \frac{dB}{dt} \right) \\
& = \frac{d}{dt} \left(\frac{\dot{\kappa}\tau}{6}s^3B + \frac{\kappa\dot{\tau}}{6}s^3B + \frac{\kappa\tau}{2}s^2\dot{s}B + \frac{\kappa\tau}{6}s^3 \frac{dB}{ds} \frac{ds}{dt} \right) \\
& = \frac{d}{dt} \left(\frac{\dot{\kappa}\tau}{6}s^3B + \frac{\kappa\dot{\tau}}{6}s^3B + \frac{\kappa\tau}{2}s^2\dot{s}B + \frac{\kappa\tau}{6}s^3\dot{s}(-\tau N) \right)
\end{aligned}$$

This will require taking the four terms separately

$$\frac{d^2}{dt^2} \left(\frac{\kappa}{2}s^2N \right) = \{1\} + \{2\} + \{3\} + \{4\}$$

First term

$$\{1\} \quad \frac{d}{dt} \left(\frac{\dot{\kappa}\tau}{6} s^3 B \right) = \left(\frac{\ddot{\kappa}\tau}{6} s^3 B + \frac{\dot{\kappa}\dot{\tau}}{6} s^3 B + \frac{\dot{\kappa}\tau}{6} 3s^2 \dot{s}B + \frac{\dot{\kappa}\tau}{6} s^3 \frac{dB}{dt} \right)$$

$$\left(\frac{\dot{\kappa}\tau}{6} s^3 B + \frac{\dot{\kappa}\dot{\tau}}{6} s^3 B + \frac{\dot{\kappa}\tau}{2} s^2 \dot{s}B + \frac{\dot{\kappa}\tau}{6} s^3 \frac{dB}{ds} \frac{ds}{dt} \right)$$

$$= \left(\frac{\dot{\kappa}\tau}{6} s^3 B + \frac{\dot{\kappa}\dot{\tau}}{6} s^3 B + \frac{\dot{\kappa}\tau}{2} s^2 \dot{s}B + \frac{\dot{\kappa}\tau}{6} s^3 (-\tau N) \dot{s} \right)$$

$$\{1\} \quad \frac{d}{dt} \left(\frac{\dot{\kappa}\tau}{6} s^3 B \right) = \left(\frac{\ddot{\kappa}\tau}{6} s^3 B + \frac{\dot{\kappa}\dot{\tau}}{6} s^3 B + \frac{\dot{\kappa}\tau}{2} s^2 \dot{s}B + \frac{\dot{\kappa}\tau}{6} s^3 (-\tau N) \dot{s} \right)$$

$$\{2\} \quad \frac{d}{dt} \left(\frac{\dot{\kappa}\dot{\tau}}{6} s^3 B \right) = \left(\frac{\dot{\kappa}\dot{\tau}}{6} s^3 B + \frac{\kappa\ddot{\tau}}{6} s^3 B + \frac{\kappa\dot{\tau}}{6} 3s^2 \dot{s}B + \frac{\kappa\dot{\tau}}{6} s^3 \frac{dB}{dt} \right)$$

$$\left(\frac{\dot{\kappa}\dot{\tau}}{6} s^3 B + \frac{\kappa\ddot{\tau}}{6} s^3 B + \frac{\kappa\dot{\tau}}{2} s^2 \dot{s}B + \frac{\kappa\dot{\tau}}{6} s^3 \frac{dB}{ds} \frac{ds}{dt} \right)$$

$$= \left(\frac{\dot{\kappa}\dot{\tau}}{6} s^3 B + \frac{\kappa\ddot{\tau}}{6} s^3 B + \frac{\kappa\dot{\tau}}{2} s^2 \dot{s}B + \frac{\kappa\dot{\tau}}{6} s^3 (-\tau N) \dot{s} \right)$$

$$\{2\} \quad \frac{d}{dt} \left(\frac{\kappa\dot{\tau}}{6} s^3 B \right) = \left(\frac{\dot{\kappa}\dot{\tau}}{6} s^3 B + \frac{\kappa\ddot{\tau}}{6} s^3 B + \frac{\kappa\dot{\tau}}{2} s^2 \dot{s}B + \frac{\kappa\dot{\tau}}{6} s^3 (-\tau N) \dot{s} \right)$$

$$\{3\} \quad \frac{d}{dt} \left(\frac{\kappa\tau}{2} s^2 \dot{s}B \right) = \left(\frac{\dot{\kappa}\tau}{2} s^2 \dot{s}B + \frac{\kappa\dot{\tau}}{2} s^2 \dot{s}B + \frac{\kappa\tau}{2} 2s\dot{s}^2 B + \frac{\kappa\tau}{2} s^2 \ddot{s}B + \frac{\kappa\tau}{2} s^2 \dot{s} \frac{dB}{dt} \right)$$

$$\left(\frac{\dot{\kappa}\tau}{2} s^2 \dot{s}B + \frac{\kappa\dot{\tau}}{2} s^2 \dot{s}B + \kappa\tau s\dot{s}^2 B + \frac{\kappa\tau}{2} s^2 \ddot{s}B + \frac{\kappa\tau}{2} s^2 \dot{s} \frac{dB}{ds} \frac{ds}{dt} \right)$$

$$= \left(\frac{\dot{\kappa}\tau}{2} s^2 \dot{s}B + \frac{\kappa\dot{\tau}}{2} s^2 \dot{s}B + \kappa\tau s\dot{s}^2 B + \frac{\kappa\tau}{2} s^2 \ddot{s}B + \frac{\kappa\tau}{2} s^2 \dot{s}^2 (-\tau N) \right)$$

$$\{3\} \quad \frac{d}{dt} \left(\frac{\kappa\tau}{2} s^2 \dot{s}B \right) = \left(\frac{\dot{\kappa}\tau}{2} s^2 \dot{s}B + \frac{\kappa\dot{\tau}}{2} s^2 \dot{s}B + \kappa\tau s\dot{s}^2 B + \frac{\kappa\tau}{2} s^2 \ddot{s}B + \frac{\kappa\tau}{2} s^2 \dot{s}^2 (-\tau N) \right)$$

$$\begin{aligned}
\{4\} \quad & \frac{d}{dt} \left(\frac{\kappa\tau}{6} s^3 \dot{s} (-\tau N) \right) \\
&= - \left(\frac{\dot{\kappa}\tau^2}{6} s^3 \dot{s} N + \frac{\kappa 2\tau \dot{t}}{6} s^3 \dot{s} N + \frac{\kappa\tau^2}{6} 3s^2 \dot{s}^2 N + \frac{\kappa\tau^2}{6} s^3 \ddot{s} N + \frac{\kappa\tau^2}{6} s^3 \dot{s} \frac{dN}{dt} \right) \\
&= - \left(\frac{\dot{\kappa}\tau^2}{6} s^3 \dot{s} N + \frac{\kappa\tau \dot{t}}{3} s^3 \dot{s} N + \frac{\kappa\tau^2}{2} s^2 \dot{s}^2 N + \frac{\kappa\tau^2}{6} s^3 \ddot{s} N + \frac{\kappa\tau^2}{6} s^3 \dot{s} \frac{dN}{ds} \frac{ds}{dt} \right) \\
\{4\} \quad & \frac{d}{dt} \left(\frac{\kappa\tau}{6} s^3 \dot{s} (-\tau N) \right) \\
&= - \left(\frac{\dot{\kappa}\tau^2}{6} s^3 \dot{s} N + \frac{\kappa\tau \dot{t}}{3} s^3 \dot{s} N + \frac{\kappa\tau^2}{2} s^2 \dot{s}^2 N + \frac{\kappa\tau^2}{6} s^3 \ddot{s} N \right. \\
&\quad \left. + \frac{\kappa\tau^2}{6} s^3 \dot{s}^2 (-\tau N) \right)
\end{aligned}$$

Combining Terms

$$\frac{d^2}{dt^2} \left(\frac{\kappa}{2} s^2 N \right) = \{1\} + \{2\} + \{3\} + \{4\}$$

$$\begin{aligned}
Third Term: \quad & \frac{d}{dt} \left(\frac{\dot{\kappa}\tau}{6} s^3 B + \frac{\kappa\dot{t}}{6} s^3 B + \frac{\kappa\tau}{2} s^2 \dot{s} B + \frac{\kappa\tau}{6} s^3 \dot{s} (-\tau N) \right) = \\
& \left(\frac{\ddot{\kappa}\tau}{6} s^3 B + \frac{\kappa\ddot{t}}{6} s^3 B + \frac{\dot{\kappa}\tau}{2} s^2 \dot{s} B + \frac{\dot{\kappa}\tau}{6} s^3 (-\tau N) \dot{s} \right) \\
&+ \left(\frac{\dot{\kappa}\dot{t}}{6} s^3 B + \frac{\kappa\ddot{t}}{6} s^3 B + \frac{\kappa\dot{t}}{2} s^2 \dot{s} B + \frac{\kappa\dot{t}}{6} s^3 (-\tau N) \dot{s} \right) \\
&+ \left(\frac{\dot{\kappa}\tau}{2} s^2 \dot{s} B + \frac{\kappa\dot{t}}{2} s^2 \dot{s} B + \kappa\tau s \dot{s}^2 B + \frac{\kappa\tau}{2} s^2 \ddot{s} B + \frac{\kappa\tau}{2} s^2 \dot{s}^2 (-\tau N) \right) \\
&- \left(\frac{\dot{\kappa}\tau^2}{6} s^3 \dot{s} N + \frac{\kappa\tau \dot{t}}{3} s^3 \dot{s} N + \frac{\kappa\tau^2}{2} s^2 \dot{s}^2 N + \frac{\kappa\tau^2}{6} s^3 \ddot{s} N + \frac{\kappa\tau^2}{6} s^3 \dot{s}^2 (-\tau N) \right)
\end{aligned}$$

Simplifying:

$$\begin{aligned}
& \left(\frac{\dot{\kappa}\tau}{6}s^3 + \frac{\dot{\kappa}\dot{\tau}}{6}s^3 + \frac{\dot{\kappa}\tau}{2}s^2\dot{s} \right) B - \frac{\dot{\kappa}\tau^2}{6}s^3\dot{s}N + \left(\frac{\dot{\kappa}\dot{\tau}}{6}s^3 + \frac{\kappa\ddot{\tau}}{6}s^3 + \frac{\kappa\dot{\tau}}{2}s^2\dot{s} \right) B - \frac{\kappa\dot{\tau}}{6}s^3\dot{s}\tau N \\
& + \left(\frac{\dot{\kappa}\tau}{2}s^2\dot{s} + \frac{\kappa\dot{\tau}}{2}s^2\dot{s} + \kappa\tau s\dot{s}^2 + \frac{\kappa\tau}{2}s^2\ddot{s} \right) B - \frac{\kappa\tau^2}{2}s^2\dot{s}^2N \\
& - \left(\frac{\dot{\kappa}\tau^2}{6}s^3\dot{s} + \frac{\kappa\tau\dot{\tau}}{3}s^3\dot{s} + \frac{\kappa\tau^2}{2}s^2\dot{s}^2 + \frac{\kappa\tau^2}{6}s^3\ddot{s} - \frac{\kappa\tau^2}{6}s^3\dot{s}^2 \right) N
\end{aligned}$$

Grouping:

$$\begin{aligned}
& \left(\frac{\dot{\kappa}\tau}{6}s^3 + \frac{\dot{\kappa}\dot{\tau}}{6}s^3 + \frac{\dot{\kappa}\tau}{2}s^2\dot{s} \right) B + \left(\frac{\dot{\kappa}\dot{\tau}}{6}s^3 + \frac{\kappa\ddot{\tau}}{6}s^3 + \frac{\kappa\dot{\tau}}{2}s^2\dot{s} \right) B \\
& + \left(\frac{\dot{\kappa}\tau}{2}s^2\dot{s} + \frac{\kappa\dot{\tau}}{2}s^2\dot{s} + \kappa\tau s\dot{s}^2 + \frac{\kappa\tau}{2}s^2\ddot{s} \right) B - \frac{\dot{\kappa}\tau^2}{6}s^3\dot{s}N - \frac{\kappa\tau^2}{2}s^2\dot{s}^2N \\
& - \frac{\kappa\dot{\tau}}{6}s^3\dot{s}\tau N - \left(\frac{\dot{\kappa}\tau^2}{6}s^3\dot{s} + \frac{\kappa\tau\dot{\tau}}{3}s^3\dot{s} + \frac{\kappa\tau^2}{2}s^2\dot{s}^2 + \frac{\kappa\tau^2}{6}s^3\ddot{s} - \frac{\kappa\tau^2}{6}s^3\dot{s}^2 \right) N
\end{aligned}$$

Third Term:

$$\begin{aligned}
& \left(\left(\frac{\dot{\kappa}\tau}{6}s^3 + \frac{\dot{\kappa}\dot{\tau}}{6}s^3 + \frac{\dot{\kappa}\tau}{2}s^2\dot{s} + \frac{\dot{\kappa}\dot{\tau}}{6}s^3 + \frac{\kappa\ddot{\tau}}{6}s^3 + \frac{\kappa\dot{\tau}}{2}s^2\dot{s} + \frac{\dot{\kappa}\tau}{2}s^2\dot{s} + \frac{\kappa\dot{\tau}}{2}s^2\dot{s} + \kappa\tau s\dot{s}^2 \right. \right. \\
& \left. \left. + \frac{\kappa\tau}{2}s^2\ddot{s} \right) B \right. \\
& - \left(\frac{\dot{\kappa}\tau^2}{6}s^3\dot{s} + \frac{\kappa\tau\dot{\tau}}{3}s^3\dot{s} + \frac{\kappa\tau^2}{2}s^2\dot{s}^2 + \frac{\kappa\tau^2}{6}s^3\ddot{s} - \frac{\kappa\tau^2}{6}s^3\dot{s}^2 + \frac{\dot{\kappa}\tau^2}{6}s^3\dot{s} \right. \\
& \left. \left. + \frac{\kappa\tau^2}{2}s^2\dot{s}^2 + \frac{\kappa\dot{\tau}}{6}s^3\dot{s}\tau \right) N \right) \rightarrow
\end{aligned}$$

$$\begin{aligned}
& \left(\left(\left(\frac{\ddot{\kappa}\tau}{6} + \frac{\dot{\kappa}\dot{\tau}}{6} + \frac{\dot{\kappa}\dot{\tau}}{6} + \frac{\kappa\ddot{\tau}}{6} \right) s^3 + \left(\frac{\dot{\kappa}\tau}{2} \dot{s} + \frac{\kappa\dot{\tau}}{2} \dot{s} + \frac{\dot{\kappa}\tau}{2} \dot{s} + \frac{\kappa\dot{\tau}}{2} \dot{s} + \frac{\kappa\tau}{2} \ddot{s} \right) s^2 + \kappa\tau s \dot{s}^2 \right) B \right. \\
& - \left(\left(\frac{\dot{\kappa}\tau^2}{6} \dot{s} + \frac{\kappa\tau\dot{\tau}}{3} \dot{s} + \frac{\kappa\tau^2}{6} \ddot{s} - \frac{\kappa\tau^2}{6} \dot{s}^2 + \frac{\dot{\kappa}\tau^2}{6} \dot{s} + \frac{\kappa\dot{\tau}}{6} \dot{s}\tau \right) s^3 \right. \\
& \left. \left. + \left(\frac{\kappa\tau^2}{2} \dot{s}^2 + \frac{\kappa\tau^2}{2} \dot{s}^2 \right) s^2 \right) N \right)
\end{aligned}$$

Simplifying further

$$\begin{aligned}
& \text{Third Term: } \frac{d^2}{dt^2} \left(\frac{\kappa\tau}{6} s^3 B \right) = \\
& \left(\left(\frac{1}{6} (\ddot{\kappa}\tau + 2\dot{\kappa}\dot{\tau} + \kappa\ddot{\tau}) s^3 + \left((\dot{\kappa}\tau + \kappa\dot{\tau}) \dot{s} + \frac{\kappa\tau}{2} \ddot{s} \right) s^2 + \kappa\tau s \dot{s}^2 \right) B \right. \\
& - \left. \left(\frac{1}{6} (\dot{\kappa}\tau^2 \dot{s} + 2\kappa\tau\dot{\tau}\dot{s} + \kappa\tau^2 \ddot{s} - \kappa\tau^2 \dot{s}^2 + \dot{\kappa}\tau^2 \dot{s} + \kappa\dot{\tau}\dot{s}\tau) s^3 + \kappa\tau^2 \dot{s}^2 s^2 \right) N \right)
\end{aligned}$$

Therefore, the final acceleration result is:

$$a = \frac{d^2}{dt^2} (sT) + \frac{d^2}{dt^2} \left(\frac{\kappa}{2} s^2 N \right) + \frac{d^2}{dt^2} \left(\frac{\kappa\tau}{6} s^3 B \right) =$$

$$\begin{aligned}
a = & ((1 - s \ddot{s} \kappa^2) \ddot{s} T + 2 \dot{s}^2 \kappa N + \tau B) \\
& + \left(\left((\ddot{\kappa} \dot{s} \kappa + \dot{\kappa}) \left(-\frac{1}{2} s^2 \right) + (\dot{s}^2 \kappa^2 + \kappa \dot{s})(-s) \right) T \right. \\
& + \left((\ddot{\kappa} - \kappa^3 \dot{s} - \kappa \tau^2 \dot{s}) \frac{1}{2} s^2 + 2s \dot{\kappa} \dot{s} + \kappa \dot{s}^2 + \kappa s \ddot{s} \right) N \\
& + \left(\left(\frac{\dot{\kappa}}{2} s \dot{s} + \kappa \dot{s}^2 + \frac{\dot{\kappa}}{2} s + \kappa \dot{s} \right) s \tau + \frac{\kappa}{2} s^2 \dot{t} \right) B \Bigg) \\
& + \left(\left(\frac{1}{6} (\ddot{\kappa} \tau + 2 \dot{\kappa} \dot{t} + \kappa \ddot{t}) s^3 + \left((\dot{\kappa} \tau + \kappa \dot{t}) \dot{s} + \frac{\kappa \tau}{2} \ddot{s} \right) s^2 + \kappa \tau s \dot{s}^2 \right) B \right. \\
& - \left. \left(\frac{1}{6} (\dot{\kappa} \tau^2 \dot{s} + 2 \kappa \tau \dot{t} \dot{s} + \kappa \tau^2 \ddot{s} - \kappa \tau^2 \dot{s}^2 + \dot{\kappa} \tau^2 \dot{s} + \kappa \dot{t} \dot{s} \tau) s^3 + \kappa \tau^2 \dot{s}^2 s^2 \right) N \right)
\end{aligned}$$

A.2 Potential Energy Derivation with Respect to Serret-Frenet Triad

Let ϕ be a trajectory such that $\phi(T, N, B)$. To make this representation as invariant, it needs to satisfy the principle of stationary action, such that the path satisfies the Euler Lagrange Equation. It will be assumed that only conservative forces act along with a gravitational field point on the negative vertical direction. In general:

$$\frac{d}{dt} \frac{\partial L}{\partial \dot{q}^p} - \frac{\partial L}{\partial q^p} = 0$$

$$L = \frac{1}{2} m(\dot{\phi})^2 - V^p(\phi)$$

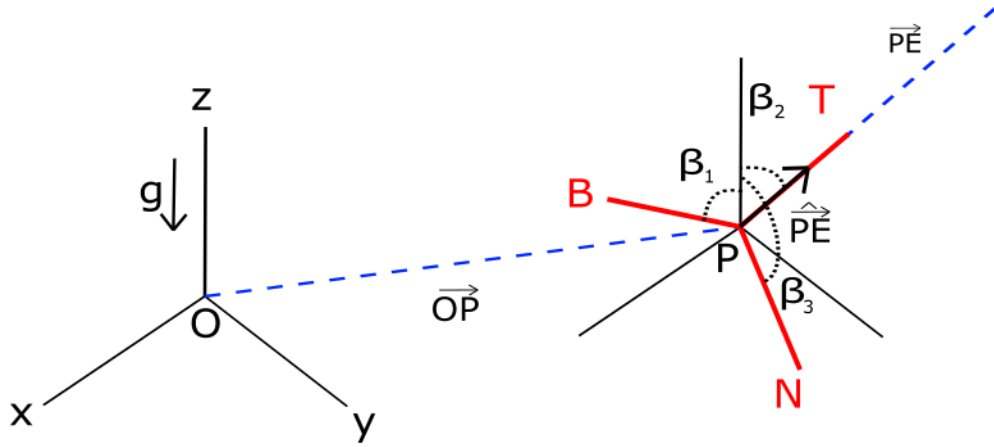
$$\frac{d}{dt} \frac{\partial L}{\partial \dot{\phi}} - \frac{\partial L}{\partial \phi} = 0$$

$$\frac{d}{dt} \frac{\partial}{\partial \dot{\phi}} \left(\frac{1}{2} m(\dot{\phi})^2 - V^p(\phi) \right) - \frac{\partial}{\partial \phi} \left(\frac{1}{2} m(\dot{\phi})^2 - V^p(\phi) \right) = 0$$

$$m \frac{d}{dt} (\dot{\phi}) = - \frac{\partial V^p(\phi)}{\partial \phi}$$

$$m \frac{d^2 \phi}{dt^2} = - \frac{\partial V^p(\phi)}{\partial \phi}$$

Where the acceleration of the trajectory $\ddot{\phi}$ has been defined in the previous section. To find the potential energy, assume a particle with respect to an arbitrary point in space (Point O as shown in Figure) and assign a Serret-Frenet triad. Denote the deviation of the Serret-Frenet unit vectors to the vertical z vector with β_i shown in Figure.



Define the gravitational potential: $V^p(\phi) = -mg\epsilon(\phi)$

Where: $\epsilon(\phi) = \cos(\beta_i) e_i \cdot \phi^p$

$$|\epsilon(\phi)| = \left| s \cos(\beta_1) + \cos(\beta_2) \left(\frac{\kappa}{2} s^2 \right) + \cos(\beta_3) \left(\frac{\kappa\tau}{6} s^3 \right) \right|$$

$$|\epsilon(\phi)| = \sqrt{s^2 \cos^2(\beta_1) + \cos^2(\beta_2) \left(\frac{\kappa}{2} s^2 \right)^2 + \cos^2(\beta_3) \left(\frac{\kappa\tau}{6} s^3 \right)^2}$$

To find the derivative:

$$\begin{aligned} \frac{\partial V^p(\phi)}{\partial \phi^p} &= \frac{\partial}{\partial \phi^p} (mg \cos(\beta_i) e_i \cdot \phi^p) \\ &= mg \cos \beta_i e_i = mg (\cos \beta_1 T + \cos \beta_2 N + \cos \beta_3 B) \end{aligned}$$

Now the complete equation looks like:

$$m \frac{d^2}{dt^2} (sN) + m \frac{d^2}{dt^2} \left(\frac{\kappa}{2} s^2 N \right) + m \frac{d^2}{dt^2} \left(\frac{\kappa\tau}{6} s^3 B \right) = -\frac{\partial V^p(\phi)}{\partial \phi^p}$$

$$m \frac{d^2}{dt^2} (sN) + m \frac{d^2}{dt^2} \left(\frac{\kappa}{2} s^2 N \right) + m \frac{d^2}{dt^2} \left(\frac{\kappa\tau}{6} s^3 B \right) = mg(\cos \beta_1 T + \cos \beta_2 N + \cos \beta_3 B)$$

Combining with the acceleration found in section A.1

$$\begin{aligned}
& m \frac{d^2}{dt^2} (sT) + m \frac{d^2}{dt^2} \left(\frac{\kappa}{2} s^2 N \right) + m \frac{d^2}{dt^2} \left(\frac{\kappa\tau}{6} s^3 B \right) = \\
& m((1 - s\ddot{s}\kappa^2)\ddot{s}T + 2\dot{s}^2\kappa N + \tau B) \\
& + m \left(\left((\ddot{\kappa}\dot{s}\kappa + \ddot{\kappa}) \left(-\frac{1}{2}s^2 \right) + (\dot{s}^2\kappa^2 + \kappa\dot{s})(-s) \right) T \right. \\
& \left. + \left((\ddot{\kappa} - \kappa^3\dot{s} - \kappa\tau^2\dot{s}) \frac{1}{2}s^2 + 2s\ddot{\kappa}\dot{s} + \kappa\dot{s}^2 + \kappa s\ddot{s} \right) N \right. \\
& \left. + \left(\left(\frac{\ddot{\kappa}}{2}s\dot{s} + \kappa\dot{s}^2 + \frac{\ddot{\kappa}}{2}s + \kappa\dot{s} \right) s\tau + \frac{\kappa}{2}s^2\dot{\tau} \right) B \right) \\
& + m \left(\left(\frac{1}{6}(\ddot{\kappa}\tau + 2\ddot{\kappa}\dot{\tau} + \kappa\ddot{\tau})s^3 + \left((\ddot{\kappa}\tau + \kappa\dot{\tau})\dot{s} + \frac{\kappa\tau}{2}\ddot{s} \right) s^2 + \kappa\tau s\dot{s}^2 \right) B \right. \\
& \left. - \left(\frac{1}{6}(\ddot{\kappa}\tau^2\dot{s} + 2\kappa\tau\dot{\tau}\dot{s} + \kappa\tau^2\ddot{s} - \kappa\tau^2\dot{s}^2 + \ddot{\kappa}\tau^2\dot{s} + \kappa\dot{\tau}\dot{s}\tau)s^3 + \kappa\tau^2\dot{s}^2s^2 \right) N \right) \\
& = -\frac{\partial V^p(\phi)}{\partial \phi^p} = mg(\cos \beta_1 T + \cos \beta_2 N + \cos \beta_3 B)
\end{aligned}$$

Separating into components:

$$T: m \left((1 - s\ddot{s}\kappa^2)\ddot{s} + \left((\ddot{\kappa}\dot{s}\kappa + \ddot{\kappa}) \left(-\frac{1}{2}s^2 \right) + (\dot{s}^2\kappa^2 + \kappa\dot{s})(-s) \right) \right) = mg \cos \beta_1$$

$$(1 - s\ddot{s}\kappa^2)\ddot{s} - \left((\dot{\kappa}\dot{s}\kappa + \dot{\kappa}) \left(\frac{1}{2}s^2 \right) + (\dot{s}^2\kappa^2 + \kappa\dot{s})s \right) = g \cos \beta_1$$

$$\begin{aligned}
N: m & \left(2\dot{s}^2\kappa + \left((\dot{\kappa} - \kappa^3\dot{s} - \kappa\tau^2\dot{s}) \frac{1}{2}s^2 + 2s\dot{\kappa}\dot{s} + \kappa\dot{s}^2 + \kappa s\ddot{s} \right) \right. \\
& \left. - \left(\frac{1}{6}(\dot{\kappa}\tau^2\dot{s} + 2\kappa\tau\dot{t}\dot{s} + \kappa\tau^2\ddot{s} - \kappa\tau^2\dot{s}^2 + \dot{\kappa}\tau^2\dot{s} + \kappa\dot{t}\dot{s}\tau)s^3 + \kappa\tau^2\dot{s}^2s^2 \right) \right) \\
& = mg \cos \beta_2 \\
2\dot{s}^2\kappa & + (\dot{\kappa} - \kappa^3\dot{s} - \kappa\tau^2\dot{s}) \frac{1}{2}s^2 + 2s\dot{\kappa}\dot{s} + \kappa\dot{s}^2 + \kappa s\ddot{s} \\
& - \frac{1}{6}(\dot{\kappa}\tau^2\dot{s} + 2\kappa\tau\dot{t}\dot{s} + \kappa\tau^2\ddot{s} - \kappa\tau^2\dot{s}^2 + \dot{\kappa}\tau^2\dot{s} + \kappa\dot{t}\dot{s}\tau)s^3 + \kappa\tau^2\dot{s}^2s^2 \\
& = g \cos \beta_2 \\
B: m & \left(\tau + \left(\left(\frac{\dot{\kappa}}{2}s\dot{s} + \kappa\dot{s}^2 + \frac{\dot{\kappa}}{2}s + \kappa\dot{s} \right) s\tau + \frac{\kappa}{2}s^2\dot{t} \right) \right. \\
& \left. + \left(\frac{1}{6}(\dot{\kappa}\tau + 2\dot{\kappa}\dot{t} + \kappa\ddot{t})s^3 + \left((\dot{\kappa}\tau + \kappa\dot{t})\dot{s} + \frac{\kappa\tau}{2}\ddot{s} \right) s^2 + \kappa\tau s\dot{s}^2 \right) \right) \\
& = mg \cos \beta_3 \\
\tau + \left(\frac{\dot{\kappa}}{2}s\dot{s} & + \kappa\dot{s}^2 + \frac{\dot{\kappa}}{2}s + \kappa\dot{s} \right) s\tau + \frac{\kappa}{2}s^2\dot{t} + \frac{1}{6}(\dot{\kappa}\tau + 2\dot{\kappa}\dot{t} + \kappa\ddot{t})s^3 \\
& + \left((\dot{\kappa}\tau + \kappa\dot{t})\dot{s} + \frac{\kappa\tau}{2}\ddot{s} \right) s^2 + \kappa\tau s\dot{s}^2 = g \cos \beta_3
\end{aligned}$$

A.3 Source Code Chapter 4: MDC Geometric Formulation Implementation

```

clear; close all; clc %Which is opposite for the
%Google Earth Data Curvature Kappa
load('GPS1Xft.mat');
load('GPS1Yft.mat');
x2 = GPSX; y2 = GPSY;
x2 = x2'*3048; y2 = y2'*3048;
%GPS DATA
% load('CVF9LatX.mat');
load('CVF9LongY.mat');
% x2 = LatX'; y2 = LongY';
%Ideal AASHTO
% load('MichXm.mat');
load('MichYm.mat');
% x2 = xm'; y2 = ym';
x2 = unique(x2, 'stable');
y2 = unique(y2, 'stable');
x2 = x2(1:numel(y2)); X =
[x2', y2'];
[L2, R2, K2] = curvature(X);
figure(1); plot(L2, R2); grid on;
title('Curvature radius \rho vs.
Cumulative curve length')
%The Radius of Curvature is High
at the Ends and Small at the
middle
xlabel('Length of Road');
ylabel('Radius \rho');
figure(2);
h = plot(x2, y2); grid on; axis
equal; set(h, 'marker', '.');
xlabel('X Coordinate');
ylabel('Y Coordinate');
title('Road with Curvature
Vectors');
hold on
quiver(x2', y2', K2(:, 1), K2(:, 2));
hold off
% figure(3); hold on;
%
plot(x2, sqrt(K2(:, 2).^2+K2(:, 1).^2));
% xlabel('X-Coordinate');
ylabel('Curvature \kappa'); grid
on;
% title('Curvature \kappa vs X
Coordinate');
% figure(4); hold on;

```

```

%
plot(x,y,'b.',x,yy1,'r-');

plot(y2,sqrt(K2(:,2).^2+K2(:,1).^2));
%
% xlabel('Y-Coordinate');
% ylabel('Curvature \kappa'); grid on;
%
% title('Curvature \kappa vs Y Coordinate')

KK =
sqrt(K2(:,2).^2+K2(:,1).^2);
figure(5); scatter(L2,KK); grid on
xlabel('Length of Road');
ylabel('Curvature \kappa');
title('Curvature \kappa vs. Cumulative curve length');

%
% Smoothing Technique on Curvature-----
figure(1050)
x = L2; y = KK;
yy1 = smooth(x,y,0.15,'loess');
%Span of 15%
yy2 = smooth(x,y,0.15,'rloess');

%
plot(x,y,'b.',x,yy1,'r-');
ylim([0,.3]); grid on
legend('Original data','Smoothed data using ''loess''',...
'Location','best');

xlabel('Segment S (m)');
ylabel('Curvature K');

%subplot(2,1,2)
figure(1051)
plot(x,y,'b.',x,yy2,'r-'); grid on;
ylim([0,.3])
xlabel('Segment S (m)');
ylabel('Curvature K');
legend('Original data','Smoothed Data',...
'Location','best');

%
[Th,n] = DiscInteg(K2,L2);

figure(20)
plot(L2(1:n),Th*180/pi); grid on
xlabel('Segment S');
ylabel('Heading Angle \theta degrees');
title('Numerically Integrated Heading \theta');

%
%-----
```

```
%Note: This angle is in
reference to the completely
horizontal line
% that was defined from the road
design perpesctive
grid on;
% Smoothing Technique on
Angles-----
figure(1000)
x = L2; y = O2;
yy1 = smooth(x,y,0.15,'loess');
%Span of 15%
yy2 = smooth(x,y,0.15,'rloess');

figure(21)
O = atand(K2(:,2)./K2(:,1));
plot(L2,O)
xlabel('S'); ylabel('Angle from
Inverse Tan')
title('Angle from Inverse Tan')
%subplot(2,1,1)
plot(x,y,'b.',x,yy1,'r-')
legend('Original data','Smoothed
data using ''loess''',...
'Location','SE')

figure(22)
[O1,O2] = direction(K2);
figure(21); plot(L2,O1)
xlabel('Segment S (m)');
ylabel('Angle from Inverse
Tangent')
title('Angle of Curvature
Direction'); grid on;
figure(22); plot(L2,O2)
xlabel('Segment S (m)');
ylabel('Angle of Velocity
Vector')
title('Angle of Velocity
Direction');

figure(1001)
plot(x,y,'b.',x,yy2,'r-'); grid
on
xlabel('Segment S (m)');
ylabel('Angle of Velocity
Vector')
legend('Original data','Smoothed
Data',...
'Location','SE')
```

```

% -----
e1 = cosd(O2); e2 = sind(O2);

figure(23)
subplot(1,2,1)
h1 = plot(x2,y2); grid on; axis
equal; set(h1,'marker','.');
hold on; quiver(x2',y2',e1,e2);
hold off
%title('Road with Velocity
Vectors')
xlabel('X Coordinate (m)');
ylabel('Y Coordinate (m)');

% ---- smoothed data quiver
subplot(1,2,2)
e1 = cosd(yy2); e2 = sind(yy2);
%figure(1002)
h1 = plot(x2,y2); grid on; axis
equal; set(h1,'marker','.');
hold on; quiver(x2',y2',e1,e2);
hold off
xlabel('X Coordinate (m)');
ylabel('Y Coordinate (m)');

% -----
figure(30)
subplot(2,2,1)
plot(L2,R2); grid on;
title('\rho vs. S')
xlabel S; ylabel ('\rho')
subplot(2,2,2)
plot(x2,y2); grid on; hold on
xlabel X; ylabel Y
title('Road with Curvature
Vectors')
quiver(x2',y2',K2(:,1),K2(:,2));
hold off
subplot(2,2,3)
plot(L2,(sqrt(K2(:,2).^2+K2(:,1)
.^2)));
grid on;
title('\kappa vs. S')
xlabel S; ylabel ('\kappa')
subplot(2,2,4)
plot(L2(1:n),Th*180/pi); grid on
title('Integrated Heading
\theta')
xlabel S; ylabel ('\theta')

```

A.4 Formulation Chapter 6: Geometric Trapezoid

The formulation of the mathematical curvature model was based on the shape of a trapezoid. This trapezoid consists of three different functions: An increasing linear slope, a constant slope, and a decreasing linear slope. To achieve a continuous and differentiable function containing the aforementioned parts, unit step functions were utilized. A minimum of 5 different values were determined to generate a general trapezoid to be fit with data. The choice of the shape values for the trapezoid are shown in Figure A.1, in which x_1 through x_4 are values defined by the segment length and x_5 is defined by the curvature.

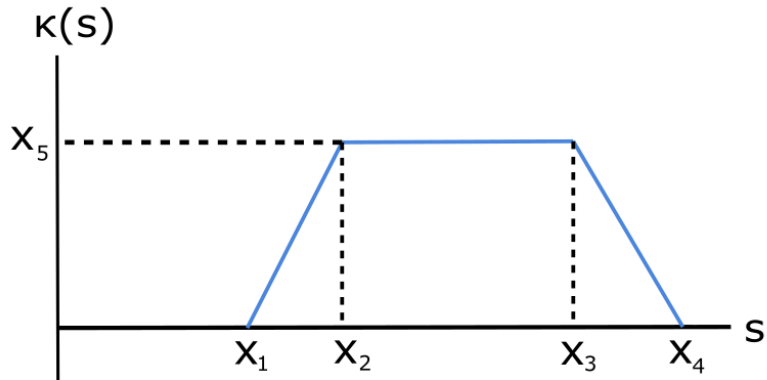


Figure A.1. Sample Curvature Model

To create this model, step functions were needed to encompass the continuity of the three desired functions. Thus, the range of the available step functions for a trapezoid are such that

$$\kappa = A[\varphi(s - x_1) - \varphi(s - x_2)] + B[\varphi(s - x_2) - \varphi(s - x_3)] + C[\varphi(s - x_3) - \varphi(s - x_4)]$$

Where:

$$\varphi(s - a) = \text{Unit Step Function with a shift of } a \in \mathbb{R}$$

It was needed to geometrically obtain the coefficients of A , B and C such that all three together will constitute a continuous function. To find B , it was sufficient with the requirement of the segment being constant, such that $B = x_5$. With B determined, A and C needed to be two linear functions connected through the value x_5 .

To obtain A , a linear increasing function is assumed. The formula for obtaining a linear function in terms of the allowed values is

$$A = \left(\frac{x_5}{x_2 - x_1} \right) s - d$$

Where d is a constant defining the vertical intercept of the function below the horizontal axis. To describe the vertical intercept in terms of the allowed values, the angle θ in between the first linear function and the vertical created by x_2 had to be found. The angle θ , and the required values to find it are shown in Figure A.2.

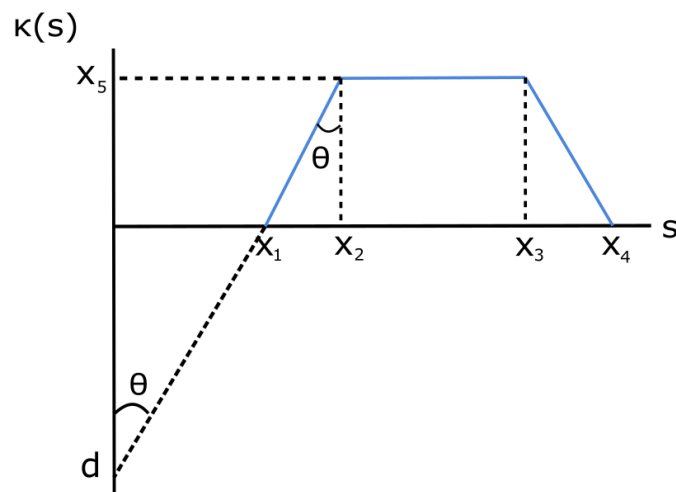


Figure A.2. Formulation for Curvature Model (1)

By geometric relations, the angle is found to be

$$\theta = \tan^{-1} \left(\frac{x_2 - x_1}{x_5} \right) = \tan^{-1} \left(\frac{x_1}{d} \right)$$

Which can be used to find the following

$$d = \frac{x_1 x_5}{x_2 - x_1}$$

By plugging the definition of the vertical intercept in the definition of A , the following is found

$$A = \left(\frac{x_5}{x_2 - x_1} \right) s - \frac{x_1 x_5}{x_2 - x_1} = \left(\frac{x_5}{x_2 - x_1} \right) (s - x_1)$$

To obtain B , a similar approach is used, in which C is modeled by a decreasing linear slope so that:

$$C = \left(\frac{x_5}{x_4 - x_3} \right) (-s) + e$$

Where e is a constant defining the vertical intercept of the function. To describe the vertical intercept in terms of the allowed values, the angle β in between the second linear function and the vertical created by x_3 had to be found. The angle β , and the required values to find it are shown in Figure A.3.

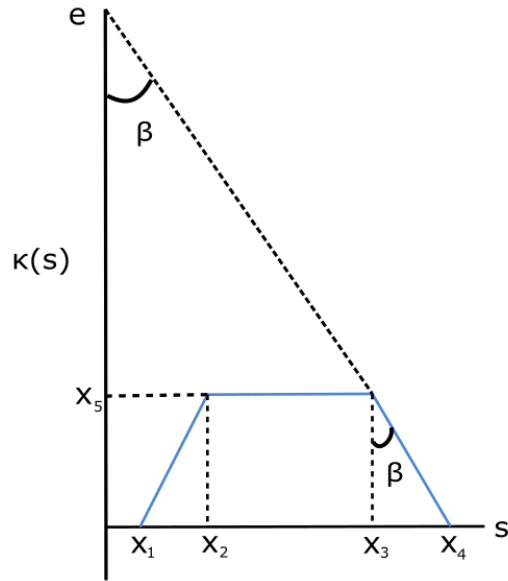


Figure A.3. Formulation for Curvature Model (2)

By geometric relations, the angle is found to be

$$\beta = \tan^{-1} \left(\frac{x_4 - x_3}{x_5} \right) = \tan^{-1} \left(\frac{x_3}{e - x_5} \right)$$

Which can be used to find the vertical intercept

$$e = \frac{x_3 x_5}{x_4 - x_3} + x_5$$

By plugging the definition of the vertical intercept in the definition of C , the following is found

$$C = \left(\frac{x_5}{x_4 - x_3} \right) (-s) + \frac{x_3 x_5}{x_4 - x_3} + x_5 = \left(\frac{x_5}{x_4 - x_3} \right) (-s + x_3) + x_5$$

By plugging the values obtained for A , B , and C , the following differentiable, continuous equation is found.

$$\kappa = \left(\frac{x_5}{x_2 - x_1} \right) (s - x_1) [\varphi(s - x_1) - \varphi(s - x_2)] + x_5 [\varphi(s - x_2) - \varphi(s - x_3)] +$$

$$\left(\left(\frac{x_5}{x_4 - x_3} \right) (-s + x_3) + x_5 \right) [\varphi(s - x_3) - \varphi(s - x_4)]$$

A.5 Source Code Chapter 6: Optimization Implementation

Curve Fitting Least Square with Noise

```

clc; clear all; close all           x0 = [0.9 2.9 4.89 7.85 11.50];

% Analysis on the performance of

M.1 under different Gaussian      fun1 = @(x,s) ((x(5)./(x(2)-
Noise Levels                      x(1))).*(s -
                                         x(1))).*(heaviside(s-x(1)) -
                                         heaviside(s-x(2))) + ...
                                         x(5).*heaviside(s-x(2))- ...
                                         heaviside(s-x(3))) + ...
                                         ((x(5)./(x(4)-x(3))).*(-
                                         s+x(3))+ x(5)).*(heaviside(s-
                                         x(3)) - heaviside(s-x(4)));

% Behavior is good because even
though there should be           % Note: the function only
compensates and does not         behaves properly when the data
generate a drop                  starts at 0 for y-axis

% Note: the function only
behaves properly when the data
starts at 0 for y-axis

s = 1:.01:25;
%y = [0 2 4.8 5.2 5 5.6];
n = numel(s)-1;
y1 = 2.*s(1:n/2) - 1;
y2 = 23*ones(1,n/2);
for k = 1:9
    y1o = awgn(y1,k,'measured');
    y2o = awgn(y2,k,'measured');
    y = [y1o y2o];
    x = lsqcurvefit(fun1,x0,s(1:end-1),y)
    times = linspace(s(1),s(end-1));
    figure
    hold on; plot(s(1:end-1),y,'bo')
    plot(times,fun1(x,times),'k-
    ','linewidth',2)
    xlim([times(1), times(end)+5])
    legend('Data','Fitted
Response','location','best');
    title('Data and Fitted Curve');
    grid on
end

```

```
end
```

Regional Routine

<pre>%%%-----</pre> <p>% 2-16-2021</p> <p>% For this SemiDynamic Routine to work</p> <p>% (1) Select your Data i.e. GPS, Google Earth, AASHTO, etc.</p> <p>% (2) Select a range that occupies one "curve segment" i.e.</p> <p>% when does curvature change considerably.</p> <p>% (3) Select appropiate Initial Conditions i.e. proportional to % segment length.</p> <p>% External files used: curvature.m direction.m</p> <p>% curvature.m can be extracted from</p> <p>% Are Mjaavatten (2021).</p> <p>%</p> <p>https://www.mathworks.com/matlabcentral/fileexchange/69452-</p>	<pre>curvature-of-a-1d-curve-in-a-2d- or-3d-space</pre> <p>%MATLAB Central File Exchange.</p> <pre>%%%-----</pre> <p>%clear; close all; clc</p> <pre>%%%-----</pre> <p>%(1)</p> <p>%Google Earth Data</p> <pre>%load('GPS1Xft.mat'); load('GPS1Yft.mat');</pre> <p>%x2 = GPSX; y2 = GPSY;</p> <pre>%x2 = x2'*3048; y2 = y2'*3048;</pre> <p>% Normalization (if needed)-----</p> <pre>%x2 = x2-min(x2); %y2 = y2-min(y2); %x2 = x2(120:180); %y2 = y2(120:180);</pre> <p>% -----</p> <p>%GPS DATA</p> <pre>% load('CVF9LatX.mat'); load('CVF9LongY.mat');</pre> <p>% x2 = LatX'; y2 = LongY';</p>
---------------------------------------------------------------------------------------------------------------------------------------------------------------------------------------------------------------------------------------------------------------------------------------------------------------------------------------------------------------------------------------------------------------------------------------------------------------------------------------------------------------------------------------------------------------------------------------------------------------------------------------------------------------------------------------------------------------------------------------------	--------------------------------------------------------------------------------------------------------------------------------------------------------------------------------------------------------------------------------------------------------------------------------------------------------------------------------------------------------------------------------------------------------------------------------------------------------------------------------------------------------------------------------------------------------------------------------------------------------------------------

```
%Ideal AASHTO

load('IdealXm.mat');
load('IdealYm.mat');
x2 = xm'; y2 = ym';
%%%%-----%
-----%
x2 = unique(x2,'stable'); y2 =
unique(y2,'stable');
x2 = x2(1:numel(y2));
x = [x2',y2'];
[L,R,K] = curvature(X);
K(1,:) = []; K(end,:) = [];
L(1,:) = []; L(end,:) = [];
xlabel('Length of Road (m)');
ylabel('Radius \rho (m)')
figure(1);
x2(1) = []; x2(end) = [];
y2(1) = []; y2(end) = [];
h = plot(x2,y2); grid on; axis
equal; set(h,'marker','.');
xlabel('X Coordinate (m)');
ylabel('Y Coordinate (m)');
title('Road with Curvature
Vectors')
hold on
quiver(x2',y2',K(:,1),K(:,2));
hold off
% -----
y = sqrt(K(:,1).^2 + K(:,2).^2);
s = L;
%-----
[O1,O2] = direction(K);
e1 = cosd(O2); e2 = sind(O2);
figure(200); hold on; h1 =
plot(x2,y2); grid on; axis
equal;
set(h1,'marker','.', 'Linewidth',
3);
quiver(x2',y2',e1,e2); hold off
%title('Road with Velocity
Vectors')
xlabel('X Coordinate (m)');
ylabel('Y Coordinate (m)');
figure; plot(s,y)
%%%-----%
-----%
%(2)
%%% Road Section-----
ni = 1;
ne = numel(x2);
% ni = 110;
% ne = 180;
%%%-----%
-----%
```

```

figure; %Ideal AASHTO IC.

plot(x2(ni:ne),y2(ni:ne),'linewi
dth',2); grid on;
xlabel('X Coordinate (m)');
ylabel('Y Coordinate (m)');
title(' ')
figure; plot(s(ni:ne),y(ni:ne));
grid on;xlabel('Segment Length
(m)');
ylabel('Curvature \kappa
(m^{-1})')
title(' ')
ySmoo =
smooth(s(ni:ne),y(ni:ne),0.15,'l
oess');
sSmoo = s(ni:ne);
figure; plot(sSmoo,ySmoo); grid
on;
xlabel('Segment Length (m)');
ylabel('Curvature \kappa (m^{-1})')
%-----%
%-----%
% Curvature Model M.1
M1 = @(x,s) ((x(5)./(x(2)-
x(1))).*(s -
x(1))).*(heaviside(s-x(1)) -
heaviside(s-x(2))) + ...
x(5).* (heaviside(s-x(2))-
heaviside(s-x(3))) + ...
((x(5)./(x(4)-x(3))).*(-
s+x(3))+ x(5)).*(heaviside(s-
x(3)) - heaviside(s-x(4)));
% Pr.1

%From this point forward, I am
doing the Optimization Semi-
Dynamic Routine
% Initial Conditions, NEVER
repeat them.

```

```

fprintf('Pr. 1, Least Squares %Parameters

Min. Has finalized');

options =
optimset('Display','off');

x =
lsqcurvefit(M1,x0,sSmoo,ySmoo, []
, [],options)

snew =
linspace(sSmoo(1),sSmoo(end),100
); % <--- This defines the
% size of the "K_vector".
figure; hold on;
plot(sSmoo,ySmoo,'bo');
plot(snew,M1(x,snew), 'k-
', 'linewidth',2);
xlim([snew(1), snew(end)+5]);
legend('Data','Fitted
Response','location','best');
title('Data and Fitted Curve');
grid on
xlabel('Segment Length (m)');
ylabel('Curvature \kappa (m^{-1})')

% -----
global K_temp e g mu
% Road Only
%e = 12; mu = 0.4;
e = 6; mu = 0.3;
% Both
g = 9.81; K_vector = M1(x,snew);

% -----
%Iterative Optimization Routine
for Pr.2 given Optimized M.1
for i = 1:length(K_vector)
K_temp = K_vector(i);

% Objective Function Pr.2
fun = @(x) x(1)^2*K_temp/g - (mu
+ 0.01*e)/(1-0.01*mu*e);

%C.1 (Bounds)
lb = 30;
%ub = [30,35];
ub = 38; % 60 < x2 < 80; mph
% There are no linear
constraints, so set those
arguments to |[]|.

A = []; b = []; % Linear In-
equality Constraints
Aeq = []; beq = []; % Linear
Equality Constraints
%Initial Conditions
x0 = 1/4;

```

```
%Constraints as an anonymous
function
Op(i,:) =
fmincon(fun,x0,A,b,Aeq,beq,lb,ub
);
end
fprintf('Pr. 2 Has finalized
\n');
figure;
plot(snew,Op(:,1), 'linewidth',2)
ylim([29 32])
xlabel('Segment Length (m)');
ylabel('Optimized Velocity
(m/s)')
title('Segment Length vs
Velocity Optimized'); grid on
```

Vehicle-Specific Routine Optimization

```
% 2-16-2021 % Are Mjaavatten (2021).
% For this Dynamic Routine to
work
% (1) Select your Data i.e. GPS,
Google Earth, AASHTO, etc.
% (2) Select a range that
occupies one "curve segment"
i.e.
% when does curvature change
considerably.
% (3) Select appropriate Initial
Conditions i.e. proportional to
% segment length.
% External files used:
curvature.m direction.m
% curvature.m can be extracted
from
```

%
<https://www.mathworks.com/matlabcentral/fileexchange/69452-curvature-of-a-1d-curve-in-a-2d-or-3d-space>

%
MATLAB Central File Exchange.

%

```
%clear; close all; clc
%Google Earth Data
%load('GPS1Xft.mat');
load('GPS1Yft.mat');
%x2 = GPSX; y2 = GPSY;
%x2 = x2'*3048; y2 = y2'*3048;
%GPS DATA
% load('CVF9LatX.mat');
load('CVF9LongY.mat');
```

```
% x2 = LatX'; y2 = LongY';
s = L;
%-----
load('IdealXm.mat');
load('IdealYm.mat');

x2 = xm'; y2 = ym';
x2 = unique(x2,'stable'); y2 =
unique(y2,'stable');
x2 = x2(1:numel(y2));
X = [x2',y2'];

[L,R,K] = curvature(X);
K(1,:) = []; K(end,:) = [];
L(1,:) = []; L(end,:) = [];
xlabel('Length of Road (m)');
ylabel('Radius \rho (m)')
figure(1);
x2(1) = []; x2(end) = [];
y2(1) = []; y2(end) = [];
h = plot(x2,y2); grid on; axis
equal; set(h,'marker','.');
xlabel('X Coordinate (m)');
ylabel('Y Coordinate (m)')
title('Road with Curvature
Vectors')
hold on
quiver(x2',y2',K(:,1),K(:,2));
hold off
% -----
y = sqrt(K(:,1).^2 + K(:,2).^2);
s = L;
%-----
[O1,O2] = direction(K);
e1 = cosd(O2); e2 = sind(O2);
figure(200); hold on; h1 =
plot(x2,y2); grid on; axis
equal;
set(h1,'marker','.', 'Linewidth',
3);
quiver(x2',y2',e1,e2); hold off
%title('Road with Velocity
Vectors')
xlabel('X Coordinate (m)');
ylabel('Y Coordinate (m)');
figure; plot(s,y); grid on;
xlabel('Segment Length (m)');
ylabel('Curvature \kappa (m^{-1})')
ni = 1;
ne = numel(x2);
%ni = 120;
%ne = 180;
figure;
plot(x2(ni:ne),y2(ni:ne)); grid
on;
xlabel('X Coordinate (m)');
ylabel('Y Coordinate (m)');
figure; plot(s(ni:ne),y(ni:ne));
```

```

grid on; xlabel('Segment Length
(m)'); ylabel('Curvature \kappa
(m^{-1})')

ySmoo =
smooth(s(ni:ne),y(ni:ne),0.15,'l
oess');

sSmoo = s(ni:ne);

figure; plot(sSmoo,ySmoo); grid
on;
xlabel('Segment Length (m)');
ylabel('Curvature \kappa (m^{-1})')
%-----%
%(3)

% Initial Conditions, NEVER
repeat them.

%Ideal AASHTO IC.

% Recommended values

%x0 = [ 100 200 300 400
max(ySmoo)];

x0 = [sSmoo(1) .90*mean(sSmoo)
1.10*mean(sSmoo) sSmoo(end)
max(ySmoo)];

%Google Earth IC.

%x0 = [sSmoo(1) .75*mean(sSmoo)
1.25*mean(sSmoo) sSmoo(end)
max(ySmoo)];

```

```

% Recommended values for non-
normalized data

% x0 = [3200 3500 4000 4200
max(ySmoo)];

%-----%
% Curvature Model M.1

M1 = @(x,s) ((x(5)./(x(2)-
x(1))).*(s -
x(1))).*(heaviside(s-x(1)) -
heaviside(s-x(2))) + ...
x(5).* (heaviside(s-x(2))-
heaviside(s-x(3))) + ...
((x(5)./(x(4)-x(3))).*(-
s+x(3))+ x(5)).*(heaviside(s-
x(3)) - heaviside(s-x(4)));

% Pr.1

fprintf('Pr. 1, Least Squares
Min. Has finalized');

options =
optimset('Display','off');

x =
lsqcurvefit(M1,x0,sSmoo,ySmoo,[]
,[],options)

snew =
linspace(sSmoo(1),sSmoo(end),100
); % <-- This defines the
% size of the "K_vector".

figure; hold on;

```

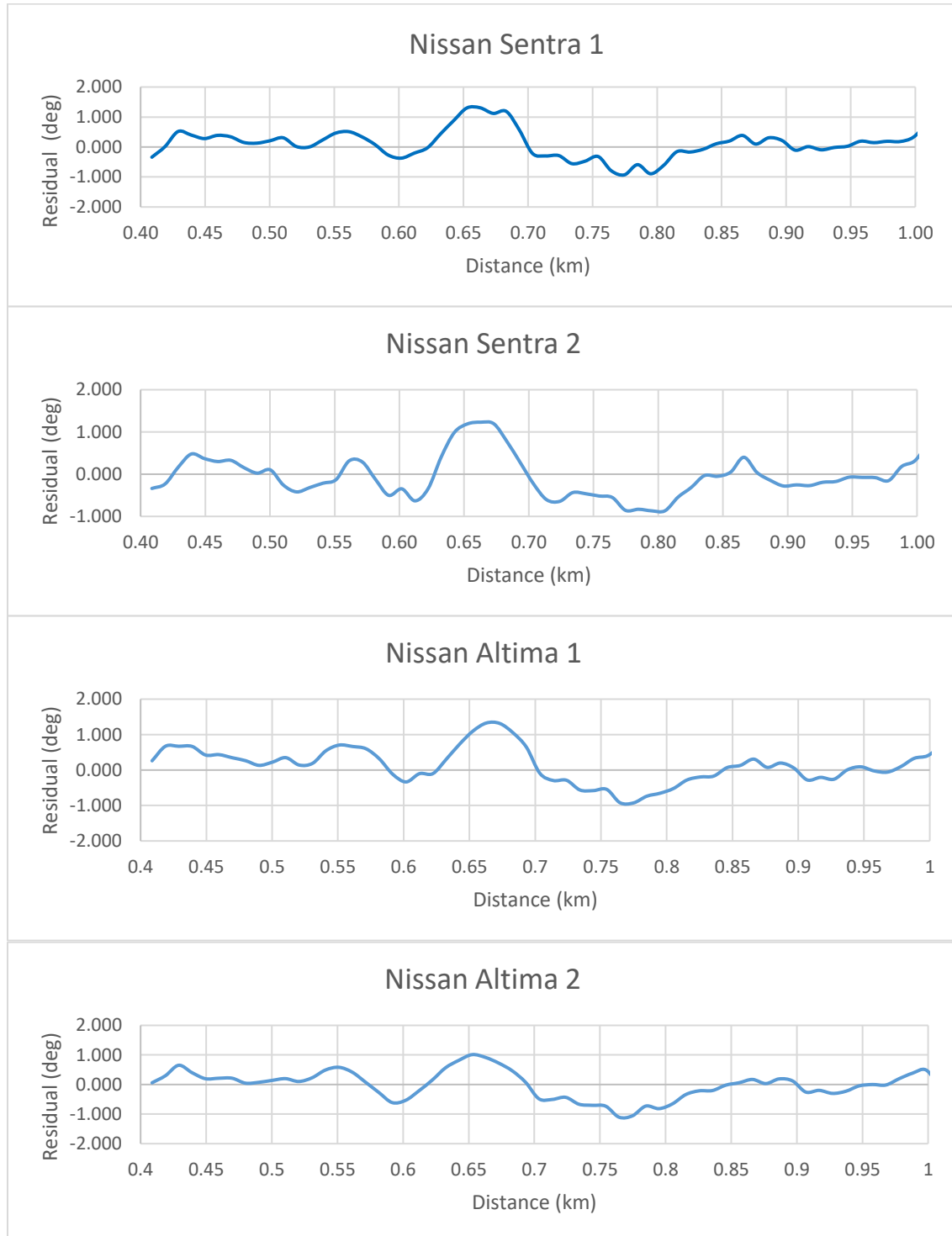
```

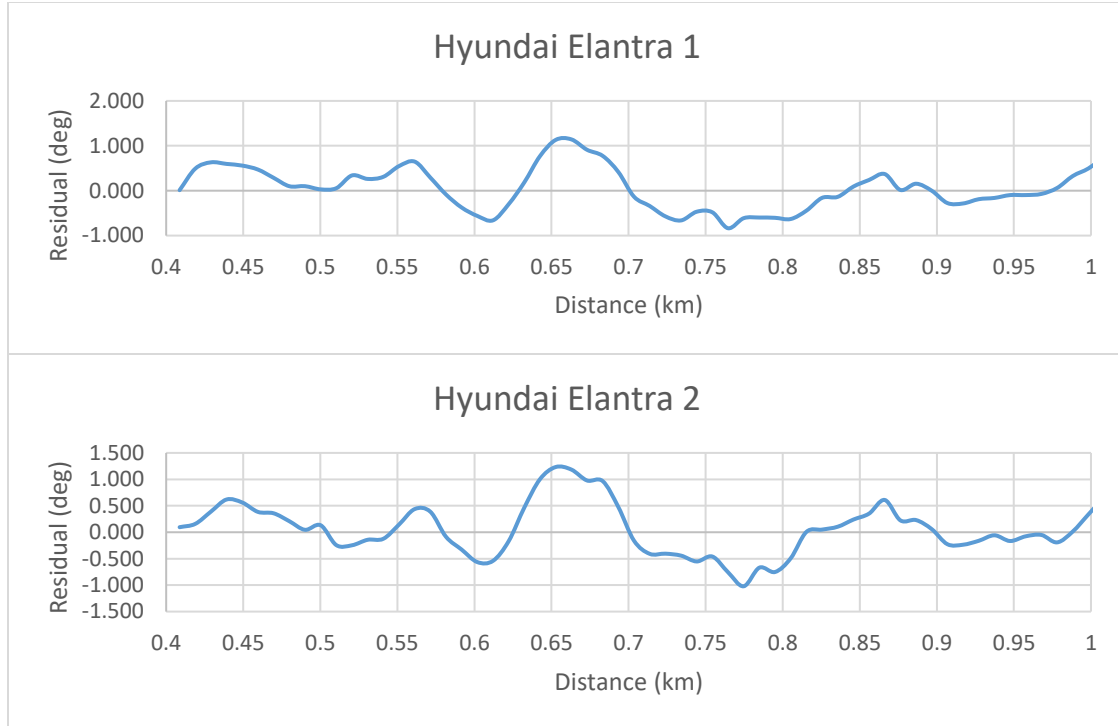
plot(sSmoo,ySmoo,'bo');
plot(snew,M1(x,snew),'k-
','linewidth',2);
xlim([snew(1), snew(end)+5]);
xlabel('Segment Length (m)');
ylabel('Curvature \kappa (m^{{-1}})')
legend('Data','Fitted
Response','location','best');
title('Data and Fitted Curve');
grid on
% -----
%Parameters
global K_temp e g mu U
% Vehicle Only
L = 2.5; U = 1.95;
%U = 3;
% Road Only
%e = 12; mu = 0.4;
e = 6; mu = 0.3;
% Both
g = 9.81; K_vector = M1(x,snew);
% -----
%Iterative Optimization Routine
for Pr.2 given Optimized M.1
for i = 1:length(K_vector)
K_temp = K_vector(i);
% Objective Function Pr.2
fun = @(x) x(1) - (53.7*L +
U*x(2)^2/g)*K_temp;
%C.1 (Bounds)
lb = [-3,25]; % -3 < x1 < 3;
%ub = [30,35];
ub = [3,36]; % 60 < x2 < 80;
mph
% There are no linear
constraints, so set those
arguments to [].
A = []; b = []; % Linear In-
equality Constraints
Aeq = []; beq = []; % Linear
Equality Constraints
%Initial Conditions
x0 = [1/4,1/2];
%Constraints as an anonymous
function
nonlcon = @EqConstraint;
options =
optimoptions('fmincon','Display'
,'off');
Op(i,:) =
fmincon(fun,x0,A,b,Aeq,beq,lb,ub
,nonlcon,options);
end
fprintf('Pr. 2 Has finalized
\n');

```

```
figure; plot(snew,Op(:,2))  
%title('Segment Length vs  
Velocity Optimized');  
grid on  
xlabel('Segment Length (m)');  
ylabel('Optimized Velocity  
(m/s)')  
% Nonlinear Constaints (Not  
bounds)  
function [c,ceq] =  
EqConstraint(x)  
  
global K_temp e g mu  
%Pr.2  
% Nonlinear Inequality  
Constraints  
c = x(2)^2*K_temp/g - (mu +  
0.01*e)/(1-0.01*mu*e);  
% Nonlinear Equality Constraints  
ceq = [];  
end
```

A.6 Residual Plots for all Vehicle Trials for Chapter 7





A.7 Histograms for all Vehicle Trials for Chapter 7

